Lewis-Acid and Fluoride-Ion Donor Properties of SF_4 and Solid-State NMR Spectroscopy of Me_3SnF

PRAVEEN CHAUDHARY

M.E., Delhi University, 2003

A Thesis

Submitted to the School of Graduate Studies

of the University of Lethbridge

in Partial Fulfillment of the Requirements

for the Degree

MASTER OF SCIENCE

Department of Chemistry and Biochemistry

University of Lethbridge

LETHBRIDGE, ALBERTA, CANADA

Abstract

Trimethyltin fluoride (Me_3SnF) is a useful fluorinating agent in organometallic chemistry. Its solid-state structure has been investigated by X-ray crystallography showing a polymeric fluorine-bridged structure. Disorder, however, has precluded the accurate refinement of all structural parameters. In order to obtain accurate structural information, trimethyltin fluoride was investigated using high-resolution ^{13}C, ^{19}F, and ^{119}Sn solid-state NMR spectroscopy using a four-channel HFXY capability. The $^{119}Sn\{^1H\}$ solid-state NMR spectrum agrees with pentacoordination about Sn in this compound. The high-resolution $^{119}Sn\{^{19}F, ^1H\}$, $^{13}C\{^1H,^{19}F\}$ and $^{19}F\{^1H\}$ NMR spectra offer unambiguous determination of $^1J(^{119}Sn\text{-}^{19}F)$ and $^1J(^{119}Sn\text{-}^{13}C)$ coupling constants. Furthermore, the analysis of the $^{119}Sn\{^{19}F, ^1H\}$, $^{119}Sn\{^1H\}$, and $^{19}F\{^1H\}$ MAS spectra as a function of spinning speed allowed for the determination of the ^{119}Sn CSA and *J* anisotropy, as well as the $^{119}Sn\text{-}^{19}F$ dipolar couplings. These were determined via SIMPSON simulations of the ^{13}C, ^{19}F, and ^{119}Sn NMR spectra. Finally the $^{119}Sn\{^{19}F, ^1H\}$ revealed fine structure as the result of $^{119}Sn\text{-}^{117}Sn$ two bond *J*-coupling, seen here for the first time.

Sulfur tetrafluoride can act as a Lewis acid. Claims had been presented for the formation of an adduct between SF_4 and pyridine, but no conclusive characterization had been performed. In the present study, adducts of SF_4 with pyridine, lutidine, 4-picoline and triethylamine were prepared and characterized by low-temperature Raman spectroscopy. Sulfur tetrafluoride also acts as a fluoride-ion donor towards strong Lewis acids, such as AsF_5 and SbF_5, forming SF_3^+ salts. Variable-temperature (VT) solid-state ^{19}F NMR spectroscopy showed that $SF_3^+SbF_6^-$ exists in three phases with phase transitions at ca. –45 and –85°C, while $SF_3^+AsF_6^-$ exists only as one phase between +20

and −150 °C. The phases of $SF_3^+AsF_6^-$ were also characterized by VT Raman spectroscopy.

Acknowledgement

I would like to thank my supervisors Prof. Michael Gerken and Prof. Paul Hazendonk to give me an opportunity to work in their laboratories. Their patience, guidance, experience, enthusiasm, support and confidence in me were invaluable throughout my years of study. With their constant help I was able to handle both specialized areas of research, i.e., fluorine chemistry and solid-state NMR spectroscopy.

I would like to thank my committee members Profs. René Boeré and Adriana Predoi-Cross for their interest and investment of time into helping me further my research.

I would like to thank Prof. Rene T. Boere for his patience, advice, invaluable suggestions and allowing me to audit the course on X-ray crystallography.

I would like to thank our NMR manager Tony Montina for his guidance and support in running the solid-state NMR experiments.

I would like thank Heinz Fischer for fixing the Raman low-temperature assembly unit from time to time.

I would like to thank our chemistry lab members Jamie Goettel, Roxanne Shank, Alex, Xin Yu, Kevin, David Franz, Matt, Mike and Breanne for their help and friendship through my research time. Again, I would like to thank Jamie Goettel for the assistance with the study of SF_4 adducts.

I would like to thank Alberta Ministry of Education and the Department of Chemistry and Biochemistry and the University of Lethbridge for their financial support.

Finally, I would like to thank my wife Yogita, my parents, my brother and my son for their constant support to finish my studies.

TABLE OF CONTENTS

LIST OF TABLES

LIST OF FIGURES

LIST OF ABBREVIATION

General

ax	axial
eq	equatorial
Kel-F	chlorotrifluoroethylene
NMR	Nuclear Magnetic Resonance
TEA	triethylamine
Me_3SnF	trimethyltin fluoride
br	broad

Nuclear Magnetic Resonance

δ	chemical shift
J	scalar coupling constant in Hertz
ppm	parts per million
TMS	tetramethylsilane
HFB	hexafluorobenzene
CP	cross polarization
DP	direct polarization
T1	spin lattice relaxation delay
T2	spin spin relaxation delay
T	tesla
MAS	magic angle spinning

X-ray Crystallography

a, b, c, α, β, γ	cell parameters
V	cell volume
λ	wavelength
Z	molecules per unit cell
mol. wt.	molecular weight
Wt. No.	isotopic molecular weight
μ	absorption coefficient
R1	conventional agreement index
wR2	weighted agreement index

Chapter-1

1. Introduction

1.1 Organotin Halides

Organotin halides are compounds which have at least one bond between tin and carbon as well as between tin and a halogen. The first organotin halide, diethyl tin dichloride, was synthesized by Frankland in 1849.[1] Tin is a member of group 14 in the periodic table with the $[Kr]4d^{10}5s^25p^2$ electron configuration. As a consequence, the most common oxidation state for tin is +4. Furthermore, organotin halides served as starting materials in the synthesis of organotin compounds having different functional groups like –OR, $-NR_2$, -OCOR etc. (Figure 1.1).[2] The most important application fields for tin compounds are catalysis, organic synthesis, biological activity, and polymers.

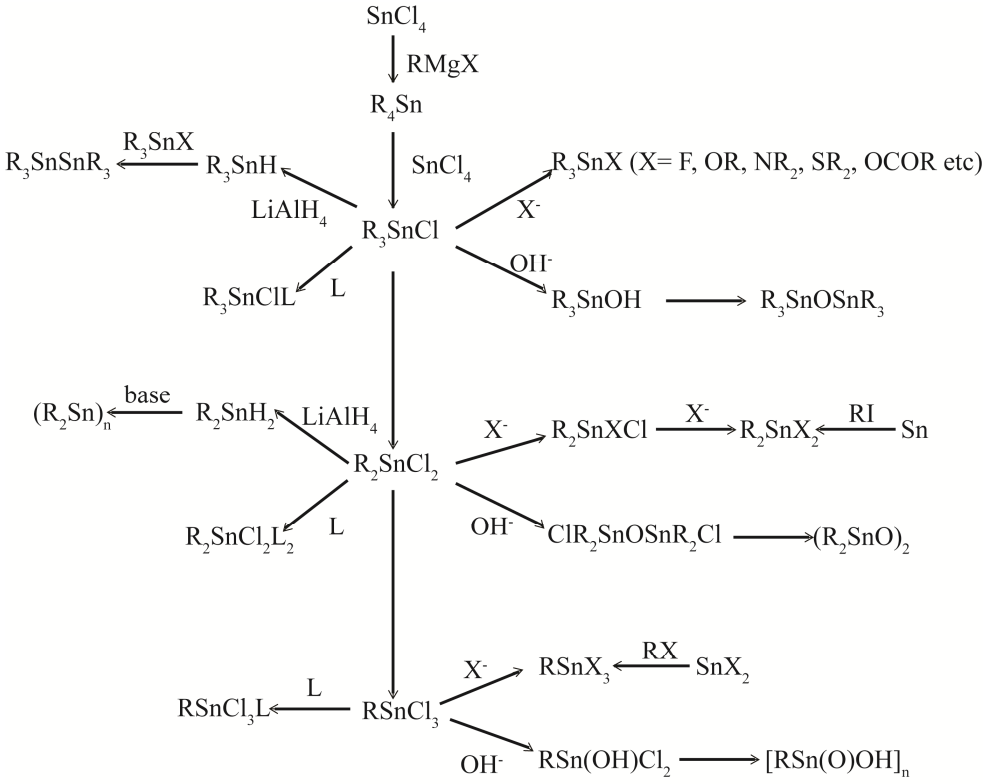

Figure 1.1 Reaction scheme for the synthesis of different organotin componds

There are five general ways to form a tin-carbon bond:

1. Reaction between an organomettallic compound and a tin halide:

   $SnX_4 + RM \rightarrow RSnX_3 + MX$

2. Reaction of tin with an alkyl halide (RX):

   $Sn + 3RX \rightarrow R_3SnX + X_2$

3. Reaction of tin hydride with an alkene:

   $H_2C{=}CH_2 + R_3SnH \rightarrow R_3SnCH_2CH_3$

4. Metathesis:

   M—R + M'—R' → M'—R + M—R'

5. Transmetallation reaction:

   Sn + M—R → Sn—R + M

Organotin halides have a wide range of structures with coordination numbers 4, 5 and 6 (Fig 1.2).

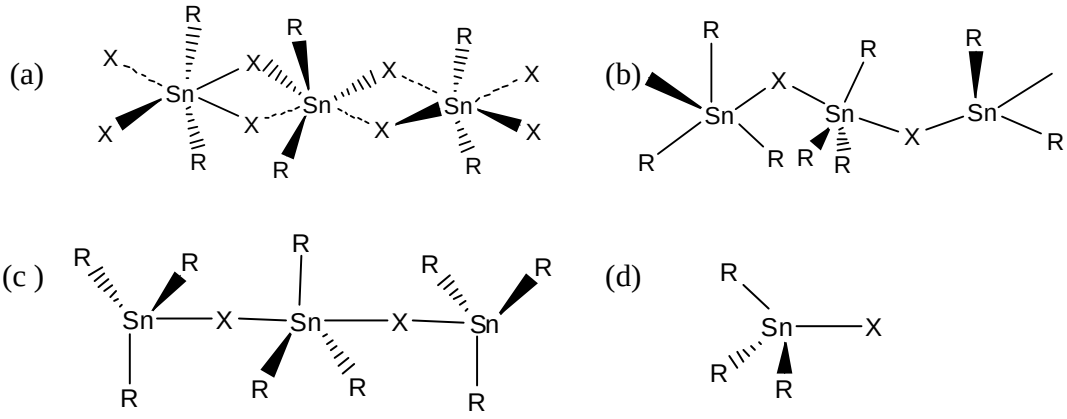

Figure 1.2 Possible structure arrangements of different organotin compounds

Triorganotin halides, except the fluorides, are usually soluble in organic solvents while organotin fluorides are usually less soluble in organic solvents.[2,3] Organotin

fluorides generally have high melting points depending on the size of the alkyl (R-) group. When R is small, the melting points normally decrease along the homologous series R_nSnX_{4-n} (where n=1,2,3).[2] It has been shown by X-ray crystallography that many organotin halides R_nSnX_{4-n} are self-associated in the solid state due to the interaction between positive metal and negative halide centers. For example, solid $[(CH_3)_3SnCl]$ exists as a zig-zag polymer while $[(C_6H_5)_3SnF]$ has a linear chain structure.

Trimethyltin fluoride (Me_3SnF) has a severely disordered structure. A model of the disordered structure suggests that the Me_3Sn units are planar and the non-linear Sn-F-Sn bridges are asymmetric with two inequivalent Sn-F distances. One Sn-F distance was determined as 2.1 Å and the other between 2.2 Å - 2.6 Å.[3] It is a very stable compound at ambient temperature having a melting point of 375°C, and has a polymeric chain structure.[2] Another model based on vibrational spectroscopy and X-ray crystallography suggested that one Sn—F distance is 2.15 Å and the other Sn·····F distane is 2.45 Å, while the F—Sn·····F angle is 141°.[4] The solid-state ^{119}Sn NMR spectrum at ambient temperature showed that the Sn is equally coupled to two fluorine atoms with a scalar coupling constant of 1300 Hz.[5]

Trimethyltin chloride $[(CH_3)_3SnCl]$ exists in the crystal as a zig-zag polymer (structure (b) in Figure 1.2) similar to $(CH_3)_3SnF$, however, $(CH_3)_3SnCl$ does not exhibit disorder in its crystal structure and the geometry about tin is very close to trigonal bipyramidal with Sn—Cl distances of 2.430(2) and 3.269(2) Å. The methyl groups about tin are arranged with a non-planar arrangement. The Cl—Sn—Cl angle is 176.85(6)° (nearly linear) and the Sn—Cl·····Sn angle is 150.30(9)°.[2, 57]

Triphenyltin fluoride [$(C_6H_5)_3SnF$] is a rod-shaped polymer (structure (c) in Figure 1.2).[2] The Sn–F distance in the symmetric fluorine bridge is 2.14 Å and the solid-state ^{119}Sn NMR spectrum shows that the Sn is equally coupled to two fluorine atoms with a scalar coupling constant of 1500 Hz at ambient temperature.[6]

The insolubility of organotin fluorides is useful in the removal of organotin residues from organic synthesis by the addition of potassium fluoride (KF), which forms an insoluble complex with organotin residues.

Solid-state NMR-spectroscopy of tin compounds is a way to determine the coordination number, chemical environment about tin, and NMR parameters like chemical shift anisotropy, and dipolar couplings, especially for polymeric tin compounds. There are three NMR-active isotopes of tin (^{115}Sn, ^{117}Sn, ^{119}Sn) having the spin quantum number I = 1/2. Tin-115 (^{115}Sn) NMR spectroscopy is not routine due to its very low natural abundance (0.35%). Although ^{117}Sn and ^{119}Sn isotopes have approximately the same natural abundance (7.61% and 8.58%, respectively) ^{119}Sn-NMR spectroscopy is more prevalent due to the higher receptivity of ^{119}Sn. Chemical shifts for ^{119}Sn NMR spectroscopy have a range of 4500 ppm (–2199 ppm for Cp_2Sn to +2325 ppm for $[(Me_3Si)_2CH]_2Sn$).[2]

1.2 Sulfur tetrafluoride chemistry: Overview and Literature

Sulfur forms several binary fluorides, among which SF_4 and SF_6 are commercially available; in addition, S_2F_2, SF_2, $FSSF_3$, and F_5SSF_5 have also been prepared.[7] In contrast to SF_6, which is chemically inert, SF_4 is very reactive and hydrolyzes readily upon

contact with trace amounts of water.[8] Sulfur tetrafluoride is used in organic chemistry to transform carbonyl (C=O) groups to CF_2 groups and hydroxyl (–OH) groups to fluoro (–F) groups.[9]

1.2.1 Sulfur tetrafluoride (SF_4)

Sulfur tetrafluoride is used as a selective fluorinating agent in the field of fluorine chemistry and is used in the synthesis of many inorganic and organo-fluorine compounds. The existence of SF_4 was first confirmed in 1950 by Silvery and Cady who synthesized it by decomposition of CF_3SF_5 in an electric discharge (Eq. 1.1).[10]

$$CF_3SF_5 \longrightarrow CF_4 + SF_4 \qquad (1.1)$$

On an industrial scale SF_4 is generated by the direct controlled fluorination of sulfur according to (Eq.1.2).[11]

$$S + 2F_2 \xrightarrow{-75°C} SF_4 \qquad (1.2)$$

The most convenient method to produce SF_4 on a laboratory scale starts from sulfur dichloride according to (Eq. 1.3).[12]

$$SCl_2 + Cl_2 + 4NaF \longrightarrow SF_4 + 4NaCl \qquad (1.3)$$

Usually SF_4 contains the impurity, SOF_2, as a hydrolysis product. Commercial SF_4 can be obtained up to a purity of 98%. It can be purified by passing it through Kel-F (homopolymer of chlorotrifluoroethylene) containing chromosorb as adsorbent or by passing it through activated charcoal.[13] Reversible salt formation using BF_3 as $[SF_3][BF_4]$[14,15] has also been utilized for its purification because the dissociation of $[SF_3][BF_4]$ results in pure SF_4. While working with SF_4, extreme caution is necessary due to the toxic nature of SF_4 and the facile production of HF on contact with moisture.[16]

Sulfur tetrafluoride has a melting point at –121 ± 0.5 °C and boiling point at –38°C.[16] On the basis of the VSEPR model[17] it was predicted that SF_4 has an AX_4E type structure with a molecular seesaw geometry (Scheme–I). It has two fluorine atoms and a lone pair in the equatorial plane while the other two fluorine atoms are in the axial position. It was found that the SF_4 molecule is fluxional on the NMR time scale at room temperature but at low temperature (–98°C) the exchange between the equatorial and axial environments is sufficiently slow to give two triplets in the low-temperature (–98°C) solution-state ^{19}F NMR spectrum.[18]

(Scheme-I)

Commercial SF_4 usually contains impurities of SF_6, HF and SOF_2 due to the hydrolysis of SF_4. In SF_4, the rapid exchange of axial and equatorial positions on sulfur can be furnished either by intermolecular[19,20] or intramolecular exchange processes.[21,22] Gibson, Ibbott and Janzen proposed an intermolecular exchange process[19,20] for the interconversion of axial and equatorial fluorines via an intermediate adduct with a donor molecule such as HF, which is usually present as an impurity. The intermolecular exchange between the axial and equatorial positions can be explained in terms of a rapid equilibrium between SF_4 and the $SF_4 \cdot D$ adduct, resulting in inversion at the sulfur atom (Fig 1.3).[20] The structure of the $SF_4 \cdot D$ adduct can adopt configurations with the donor (D)

being *cis* or *trans* to the lone pair. The structure with the donor (D) *trans* to the lone pair is the only one leading to isomerization.[20]

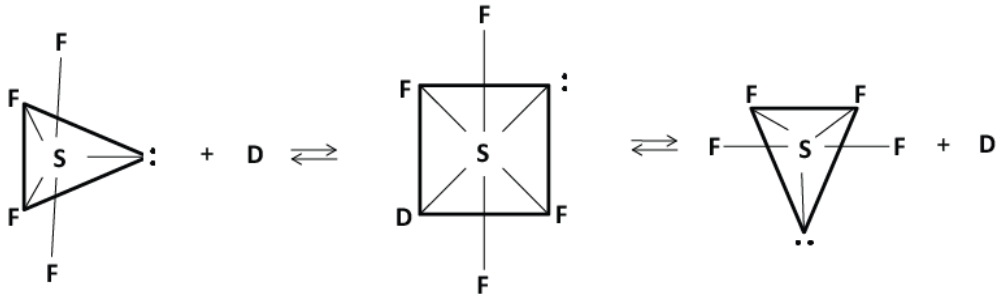

Where D = HF or F^-

Fig 1.3: Mechanism of the exchange between axial and equatorial fluorine atoms in SF_4

Klemperer and Muetterties found that the exchange rate is considerably smaller for rigorously purified SF_4, suggesting that an intramolecular mechanism such as Berry pseudorotation[23] is operative in pure SF_4.[21] Most publications assume a Berry pseudorotation mechanism for the exchange in pure SF_4. A barrier of 33.89 kJ/mol was calculated for the Berry pseudo rotation at the DFT level with B3LYP/6-31+G and B3LYP/6-311+G basis sets.[22,24]

1.2.2 Sulfur tetrafluoride chemistry

Sulfur tetrafluoride has been employed to convert carbon oxygen functional groups to CF_n groups.[16] It converts organic hydroxyl, carbonyl and carboxylic acid groups into mono-, di- and trifluoromethyl groups, respectively.[25]

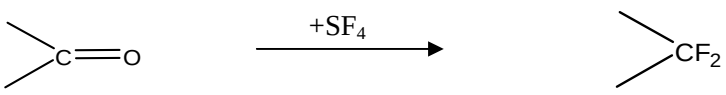

(1.4)

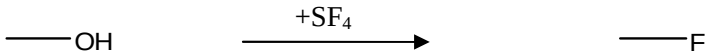

(1.5)

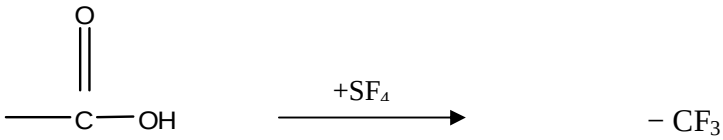

(1.6)

The products of the reaction of esters with SF_4 are usually trifluoromethyl compounds.

$$C_6H_5COOCH_3 + 2SF_4 \xrightarrow{+SF_4} C_6H_5CF_3 + CH_3F + 2SOF_2 \quad (1.7)$$

Sulfur tetrafluoride has also been employed as a reagent in inorganic chemistry. For example SF_4 can convert the P=O group to $–PF_2$ (Eq. 1.8), the –N=C=O group to $–N=SF_2$ (Eq. 1.9), and –CN group to $–CF_2N=SF_2$ (Eq. 1.10).[16]

$$(C_6H_5)_3P=O + SF_4 \longrightarrow (C_6H_5)_3PF_2 + SOF_2 \quad (1.8)$$

$$R\text{-}N=C=O + SF_4 \longrightarrow R\text{-}N=SF_2 \quad (1.9)$$

$$R\text{-}CN + SF_4 \longrightarrow RCF_2N=SF_2 \quad (1.10)$$

Sulfur tetrafluoride can act as a weak Lewis acid.[8] Its fluoride-ion-acceptor properties are well established yielding the SF_5^- anion.[26,27,28] Tunder and Siegel[27] were successful in synthesizing $[(CH_3)_4N][SF_5]$ (Eq.1.11), whereas Tullock, Coffman and Muetterties[29] synthesized $Cs[SF_5]$ (Eq.1.12). The $Cs[SF_5]$ salt was subsequently characterized by X-ray crystallography[30] and vibrational spectroscopy[31]. Only few papers were published on the reaction of SF_4 with the nitrogen containing Lewis bases (Eq. 1.13).[32, 33]

$$SF_4 + (CH_3)_4NF \longrightarrow (CH_3)_4NSF_5 \quad (1.11)$$

$$SF_4 + CsF \longrightarrow CsSF_5 \quad (1.12)$$

$$SF_4 + C_5H_5N \longrightarrow C_5H_5N\cdot SF_4 \quad (1.13)$$

Sulfur tetrafluoride can act as fluoride-ion donor towards strong Lewis acids, e.g., BF_3, PF_5, AsF_5, and SbF_5 to produce SF_3^+ salts, which have been characterized by vibrational spectroscopy.[15]

$$SF_4 + BF_3 \longrightarrow SF_3BF_4 \qquad (1.14)$$

$$SF_4 + MF_5 \longrightarrow SF_3MF_6 \quad \text{where (M = Sb, As)} \qquad (1.15)$$

While $[SF_3^+][BF_4^-]$ dissociates at room temperature under dynamic vacuum to SF_4 and BF_3, $[SF_3^+][AsF_6^-]$ and $[SF_3^+][SbF_6^-]$ are stable towards dissociation at room temperature. Crystal structures have been reported for $[SF_3^+][BF_4^-]$ and for $[SF_3^+]_2[GeF_6^{2-}]$.[16,34]

1.3 Solid-state NMR spectroscopy

Solid-state NMR spectroscopy is very useful in providing molecular structural information even up to the nanoscale level because with dipolar-coupling value the internuclear distance information can be estimated.[35] Solid-state NMR spectra are intrinsically anisotropic due to the inclusion of orientation-dependent interactions, which in solution-state are averaged out by rapid, random tumbling. Specific techniques were developed for solid-state NMR spectroscopy to achieve higher resolution, selectivity, and sensitivity. These include magic angle spinning (MAS), cross polarization (CP), improvements in probe electronics, and specialized decoupling[36] and recoupling sequences.[37,38]

Multiple-pulse sequences are commonly employed as decoupling sequences. Decoupling a nucleus like ^{19}F, which has a very large chemical shielding anisotropy (CSA), is particularly difficult. Multiple-pulse sequences can impose rotational

transformations, i.e., changing the phase and frequency of the applied radio-frequency pulse for better decoupling, on the spin operators to selectively remove and introduce spin-spin and spin-field interactions. Even at this point, highly resolved ^{1}H NMR spectra are still very difficult to acquire because of the small chemical shift range of ^{1}H.

1.4 Solid-state ^{19}F NMR spectroscopy

Covalent hydrogen atoms in the hydrocarbon compounds can be replaced with fluorine atoms without drastic changes of the structure. Fluorinated compounds have many useful applications in different fields, ranging from medical science to space technology. Such compounds can be readily studied by solid-state ^{19}F NMR spectroscopy. Fluorine-19 is 100% naturally abundant and has a resonance frequency close to that of ^{1}H, i.e., 469.99 MHz for ^{19}F and 499.99 MHz for ^{1}H at 11.7 T magnetic field strength available at the University of Lethbridge. Proton as well as ^{19}F are spin-½ nuclei. Therefore, ^{19}F is easily detected, similar to ^{1}H, but often has higher resolution due to its large range of chemical shifts. Historically, NMR technology was limited to HX– or FX– types of probe configurations as it was difficult to isolate two closely spaced frequencies at high power. Nowadays, NMR spectrometers are available on which ^{1}H and ^{19}F can be decoupled simultaneously by using HFX triple-channel or HFXY four-channel probes to get high-resolution NMR spectra.

Fluorine-19 exhibits a large chemical shift range of over 1000 ppm and is affected by large homonuclear dipolar coupling and large chemical shielding anisotropies, which can results in solid-state NMR spectral line widths in excess of 160 ppm for static samples at 4.7 T.[39] Homonuclear dipolar interactions gives rise to homogeneous

broadening and if the magic angle spinning is not able to reduce it appreciably, additional multiple pulse sequences, such as windowed sequences (e.g. wPMLG), are required to remove these interactions. Shielding anisotropies are inhomogeneous and can be refocused or averaged by MAS giving isotropic resonances with the sideband patterns which are typical of chemical-shielding-anisotropy (CSA) information.[39] Fluorine-19 solid-state NMR spectroscopy is very useful in obtaining information about the spatial arrangement of the atoms by determining the CSA, the distance between the atoms, as well as symmetry in the molecule through dipolar coupling and quadrupolar effects.[40]

Obtaining information about phase transitions is a new emerging application field in solid-state ^{19}F NMR spectroscopy. With the advent of variable-temperature solid-state NMR spectroscopy (–150℃ to +300℃), it is possible now to get this information.[41]

The study of CaF_2 in various systems with solid-state ^{19}F NMR spectroscopy represents important examples. Calcium fluoride (CaF_2) is generally used to decrease the melting point of steel making slags and is an essential component for the crystallization of cuspidine ($CaO{\cdot}2SiO_2{\cdot}CaF_2$). Different compositions with different molar ratios of $CaO{\cdot}SiO_2$ versus CaF_2 were correlated with the ^{19}F chemical shift of $CaO{\cdot}SiO_2{\cdot}CaF_2$ glasses. In addition, the ^{19}F–^{19}F dipole interactions were studied with the help of MAS and static solid-state NMR spectra.[42]

Calcium fluoride has been studied in detail because of its importance in the human dental enamel.[43] Udo *et al.*[44] correlated the experimental ^{19}F chemical shift values of alkali metal fluorides with the electronegativities of alkali metals.[44] They said that their experimental ^{19}F chemical shift values correlate quite well with the Pauling electronegativities of alkali metals and even better with the Allred-Rochow

electronegativities.[44] Solid-state ^{19}F NMR spectroscopy can also provide information about coordination numbers.[44]

One important field of the applications of the solid-state ^{19}F NMR spectroscopy is polymer science. Fluorine-19 NMR spectroscopy has been employed to characterize the different phases with the help of $T_{1\rho}$ measurements.[45] Ellis *et al.* used ^{19}F NMR spectroscopy in combination with mass spectrometry in analyzing the atmospheric fluoroacid precursors evolved from the thermolysis of fluoropolymers.[46]

Fluorine-19 solid-state NMR spectroscopy has also been used for the study of biomembranes, obtaining intramolecular distances, which led to the distinction between secondary structures of biomembranes.[47]

Fluorine-19 solid-state NMR spectroscopy has been shown to be a powerful technique in determining the amount of crystalline and amorphous phases present in a pharmaceutical solid.[48] The amorphous phase is of great interest in pharmaceutical materials since it has an impact on the solubility and better bioavailability of these materials. Most crystallinity-quantification work done to date in the pharmaceutical field has made use of ^{13}C solid-state NMR spectroscopy, as carbon is present in almost all drugs.[48] Carbon-13-based quantification methods have relied on either least-squares-type analyses or measurements of relaxation parameters that were used in combination with peak areas. Offerdahl *et al.*[49] measured relaxation times in cross polarization experiments and used this information in combination with the integrated peak area of selected resonances to estimate the amount of different polymorphs present in a sample. This method is attractive as it does not require standards if the ^{13}C NMR spectrum shows sufficient chemical resolution. The high gyromagnetic ratio and 100% natural abundance

of ^{19}F allow for high sensitivity that is required to quantify low amorphous content.[48] Using the ^{19}F nucleus can be advantageous over the more common ^{13}C nucleus in oral formulations as excipient components also contribute to the ^{13}C NMR spectrum. Similar type of work is also in progress for Nafion and polycrystalline amino acids.[48]

1.5 General Procedures in Solid-State NMR Spectroscopy

(The following discussion of NMR spectroscopy in chapters 1.5.1.1 to 1.5.1.3; 1.5.1.4; 1.5.1.5 to 1.5.1.8; 1.5.1.9; and 1.5.2 to1.5.7 is heavily based on the references 50 to 52; 50, 53, 54; 50 to 52, 55, 56; 50, 51, 57 to 59; and 50, 51, 60 to 63, respectively.)

1.5.1 1D-NMR spectroscopy

1.5.1.1 Spin and Magnetization

Fundamental particles are characterized by their finite sizes, a well defined mass, fixed charges (including zero) and a well defined intrinsic angular momentum (spin). The spin of a particle can be given by its spin quantum number *I*. Particles having a spin quantum number $I = ½$ are called fermions and quantum mechanics shows that they are not superimposable, i.e., they cannot occupy the same space at the same time. Fundamental particles, such as nucleons, have intrinsic angular momenta, initially thought to arise from motion, hence spin, which produces a magnetic moment. These combine to give rise to the magnetic moment (μ) of the nucleus. The ratio of the magnetic moment of the nucleus to its spin angular momentum is defined as the gyromagnetic ratio ($\boldsymbol{\gamma}$) of the nucleus.

The magnetic moment μ determines the potential energy E of the nuclear magnetic dipole in a static magnetic field ($\vec{B}$) of strength (or flux density) B_z, according to Eq. (1.5.1).

$$E = -\vec{\mu} \cdot \vec{B} \tag{1.5.1}$$

The nuclear spin angular momentum is given by the vector $\vec{\mathbf{I}}$, whose total magnitude can be defined by Eq. 1.5.2.

$$\overrightarrow{|\mathbf{I}|} = \hbar\sqrt{I(I+1)} \tag{1.5.2}$$

where I is the nuclear spin quantum number and $\hbar = \frac{h}{2\pi}$, with a Planck's constant, h. The magnetic moment $\vec{\mu}$ is related to the gyromagnetic ratio (γ) of a particular nucleus and can be given according to Eq. (1.5.3).

$$\gamma = \frac{\overrightarrow{|\mu|}}{\overrightarrow{|I|}} = \frac{\overrightarrow{|\mu|}}{\hbar\sqrt{I(I+1)}} \quad \text{or for simplicity it is often written as,} \quad \gamma = \frac{|\vec{\mu}|}{\hbar I} \tag{1.5.3}$$

Nuclear magnetic moments $\vec{\mu}$ may also be expressed in terms of the nuclear magneton as shown in Eq. (1.5.4).

$$\vec{\mu} = g_N \mu_N \vec{I} \tag{1.5.4}$$

where, $\mu_N = \frac{e\hbar}{2m_p} = 5.050 \times 10^{-27} JT^{-1}$ and g_N is the nuclear g-factor.

From Eq. (1.5.3) and Eq. (1.5.4), it can be written

$$\overrightarrow{|\mu|} = g_N \mu_N |\vec{\mathbf{I}}| = \gamma\hbar I \tag{1.5.5}$$

From Eq. (1.5.1) and (1.5.3), it can be seen

$$E = -\boldsymbol{\gamma} \cdot \hbar \cdot \vec{I} \cdot \vec{B} \tag{1.5.6}$$

The observable components of I along the quantization axis, i.e., the external magnetic field, are $m_\ell\hbar$ where m_ℓ is the magnetic quantum number and takes the values of $+I$, $+I$-1, $+I$-2……$-I$+1, $-I$ with $2I$+1 different values.

In quantum mechanics, the angular momentum $\vec{\mathbf{I}}$ (I_x, I_y, I_z) has uncertainty associated with it and, thus, its three components in the x, y and z directions, I_x, I_y and I_z

respectively, cannot be known simultaneously because these components do not commute with each other nor with the total angular momentum ($|\vec{\mathbf{I}}|$). However, the term $\mathbf{I^2}$ commutes with I_z and thus the orientation of the angular momentum can be represented by I_z. The total angular momentum (**I)** can be defined as in Eq. 1.5.7.

$$|\vec{\mathbf{I}}|^{\mathbf{2}} = \vec{I}_x^2 + \vec{I}_y^2 + \vec{I}_z^2 \qquad (1.5.7)$$

In the absence of an external magnetic field, the alignment of the magnetic moment of the charged particle is random, and these randomly oriented spins cancel out the individual magnetic moments, resulting in a net polarization of the ensemble of spins of zero. When an external magnetic field is applied to these spins, it gives rise to a net directional preference of spin alignment either in the direction of the applied magnetic field or in the opposite direction of the applied magnetic field (Fig 1.5.1). A net polarization (magnetization) is produced in the direction of the applied field because the net distribution of spin orientations, with magnetic moments aligned in the direction of the applied external magnetic field being slightly preferred over the magnetic moments opposing the externally applied magnetic field.

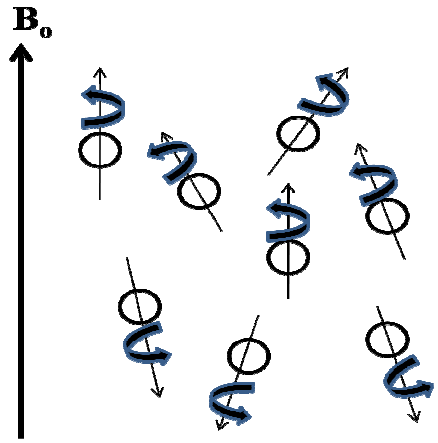

Figure 1.5.1: Alignment of spins in the presence of a static magnetic field

According to the Boltzmann distribution the number of spins in the lower energy state will always be larger than that of the higher energy state. The population difference will be governed by the Eq. 1.5.8.

$$\frac{N}{N_i} = e^{\frac{-\Delta E}{kT}} \tag{1.5.8}$$

where k is Boltzmann's constant. The difference of magnetic energy between a single proton polarized along the field and the one polarized against the field is $\hbar\gamma B_z$ = 3.3×10^{-25} J in a static magnetic field ($\vec{B}$) of 11.74 T. The available thermal energy at room temperature is kT = 4.1×10^{-21} J, which is larger by about four orders of magnitude. As a consequence in the case of nuclear spins we have only slightly biased spin polarization as shown in Figure 1.5.1. This net spin polarization is referred to as magnetization.

1.5.1.2 Zeeman Effect

Every rotating object in classical mechanics has an angular momentum, which can be described as a vector along the axis about which the object rotates. In the classical theory of angular momentum, it is continuous but in the case of quantum mechanical theory, it is quantized. The spin angular momentum of spin is a vector which can be oriented in any possible direction in space. The magnetic moment of a nucleus points either in the same direction as the spin (for nucleus $\gamma > 0$, e.g., ^{15}N, ^{17}O) or in the opposite direction (for nucleus $\gamma < 0$, e.g., ^{129}Xe). In the absence of a magnetic field, the magnetic moment can point in all possible directions, i.e., it is isotropic in nature. When an external magnetic field is applied, however, the nuclear spins start to precess around the field. The

magnetic moment of the spins move on a cone, keeping a constant angle between the spin magnetic moment and the field. This motion is called ‘precession’.

In an applied external magnetic field, the spin states split into 2*I*+1 levels, which is known as Zeeman splitting (Figure 1.5.2) and the effect is known as the ‘Zeeman effect’. The energy value for each of these levels can be determined from the interaction between the nucleus and the static magnetic field.

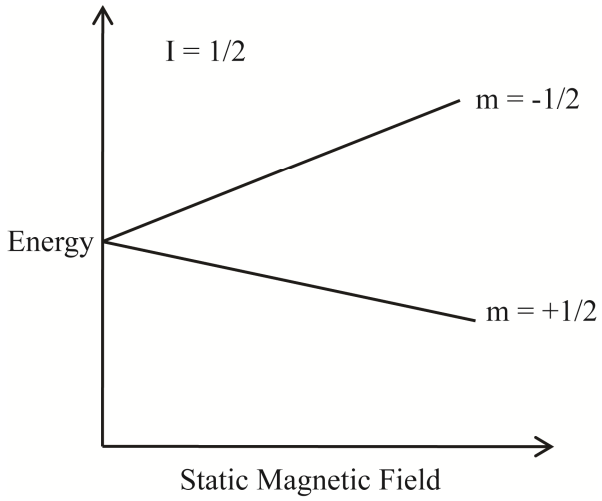

Figure 1.5.2: Zeeman splitting of the energy levels for spin-1/2 nucleus in the presence of externally applied magnetic field

1.5.1.3 Nuclear Spin Hamiltonian

The nuclear spin Hamiltonian describes the interaction of the nuclear spin with the following magnetic fields:

(i) External: The interaction of nuclear spin with the static magnetic field $\vec{B}$ and the radiofrequency $\vec{B}_{rf}$ from the electromagnetic radiation produced by the instrument.

(ii) Internal: The interaction of the spins present in the sample, for example, dipolar coupling, *J*-coupling, and quadrupolar coupling.

The total Hamiltonian can therefore be written as given in Eq. 1.5.9.

$$\hat{\mathbf{H}} = \hat{\mathbf{H}}^{\mathrm{CS}} + \hat{\mathbf{H}}^{\mathrm{rf}} + \hat{\mathbf{H}}^{J-\mathrm{coupling}} + \hat{\mathbf{H}}^{\mathrm{dipolar-coupling}} + \hat{\mathbf{H}}^{\mathrm{quadrupolar-couplings}} \quad (1.5.9)$$

In the case of spin-½ nuclei, we are mainly concerned with the effects of $\hat{\mathbf{H}}^{\mathrm{cs}}$, $\hat{\mathbf{H}}^{\mathrm{rf}}$ and $\hat{\mathbf{H}}^{J\text{-coupling}}$ in isotropic (solution-state) NMR spectroscopy, while in anisotropic (solid-state) NMR spectroscopy of spin-½ nuclei, all the effects except quadrupolar become effective as mentioned in Eq. 1.5.9.

1.5.1.4 Relaxation (T_1, T_2, $T_{1\rho}$)

Spin Lattice Relaxation (T_1) is a process by which the longitudinally polarized state of the spin ensemble returns to equilibrium (from the Y-axis to Z-axis), from some perturbed state, after the application of a pulse (Figure 1.5.3). This recovery process (Eq. 1.5.10) is facilitated by an energy exchange between the spins and their surroundings. The time scale of T_1 will be dependent on the factors which influence the fluctuating magnetic fields, such as temperature and viscosity, and may range from milliseconds to days. Figure 1.5.3 shows the recovery of longitudinal magnetization.

$$\mathrm{M_z} = \mathrm{M_o}(1 - \mathrm{e}^{\frac{-\mathrm{t}}{\mathrm{T_1}}}) \quad (1.5.10)$$

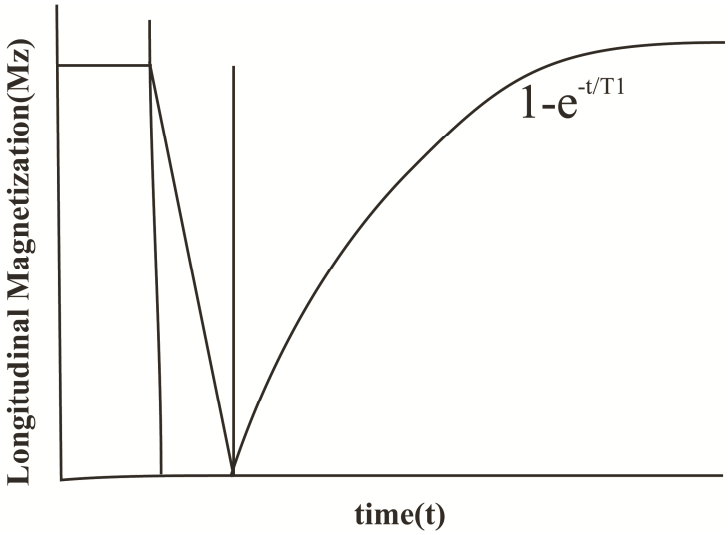

Figure 1.5.3 Recovery of the equilibrium magnetization according to the longitudinal relaxation rate T_1.

Spin-Spin Relaxation (T_2): The phase coherence between nuclear spin vectors present immediately after a pulse is lost over time. As a result the transverse component of the magnetization in the rotating frame decays to zero exponentially, characterized by a decay constant known as T_2. This process is referred to as transverse relaxation (T_2) given in Eq. 1.5.11 and illustrated in Figure 1.5.4. The relaxation time constant,T_2, determines the length of the FID signal detected in an instrument with an perfectly homogeneous field. Furthermore, the relaxation rate, which is the reciprocal of T_2, determines the full width at half height in the signal of NMR spectrum, thereby, imposing the upper limit on spectral resolution.

$$M_z = M_o e^{\frac{-t}{T_2}} \qquad (1.5.11)$$

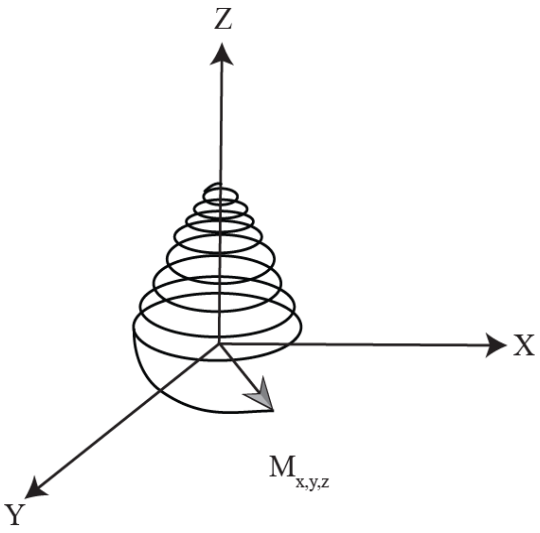

Figure 1.5.4 Decay of magnetization in the transverse (i.e. XY) plane

The graphical form of the loss of transverse magnetization is shown in Figure 1.5.5.

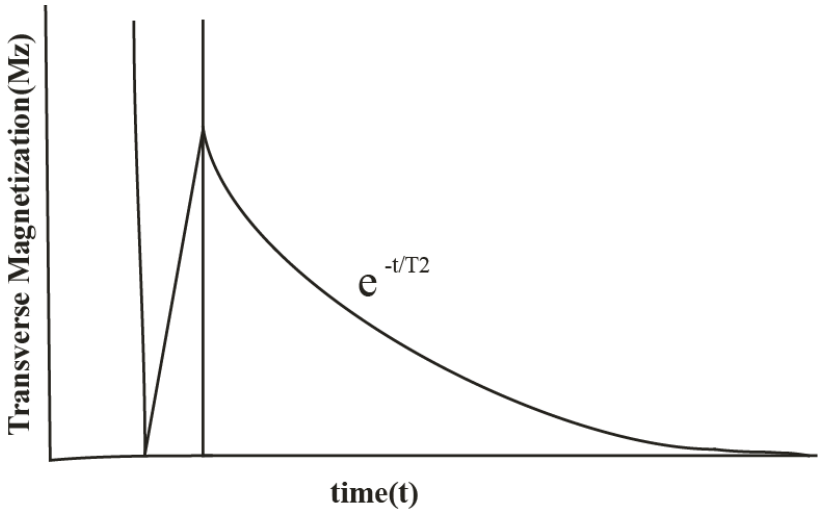

Figure 1.5.5 Decay of the transverse magnetization according to the transverse relaxation rate T_2.

Spin Lattice relaxation in the rotating frame ($T_{1\rho}$)

If a $(90°)_x$-pulse is applied on the z-magnetization vector in the rotating frame, the magnetization vector is moved to the –y axis. In this condition, if a pulse along +y axis is applied that is strong enough to keep the net magnetization along the same axis, i.e., along –y axis, the spins are locked (Fig 1.5.6). If the spin locking pulse is turned off on +y axis, the magnetization returns back to the thermal equilibrium condition in the rotating frame with the frequency of the applied spin locking Rf field, instead of the Larmor frequency. This experiment is called T_1 relaxation in the rotating frame ($T_{1\rho}$) experiment.

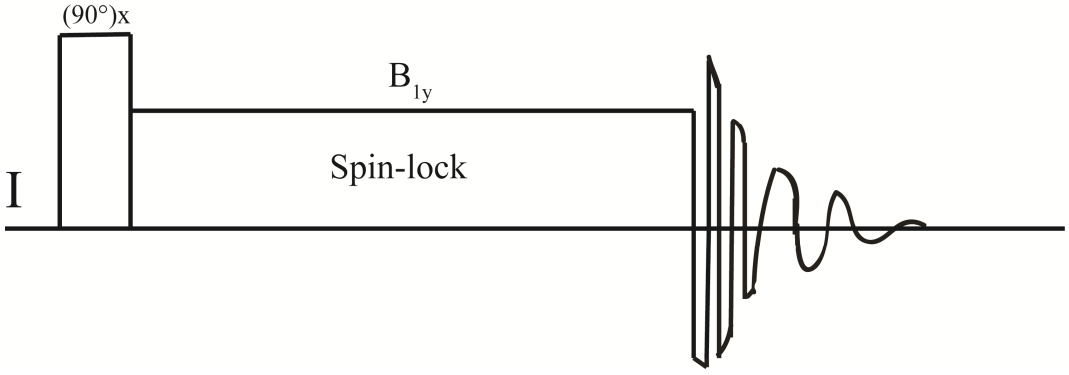

Figure 1.5.6 A basic pulse sequence for measuring $T_{1\rho}$

1.5.1.5 Chemical Exchange

Motion of various kinds can be observed in NMR spectra in both solution-state or solid-state. In solution-state dynamic processes can lead to modulations in chemical shifts and *J*-couplings resulting from conformational changes in the molecules, such as rotation and inversion processes. In the solid-state a simple reorientation of molecule with respect

to applied magnetic field will modulate the resonance frequencies in the spectra owing to the orientational dependence of the spectral parameters. This phenomenon is known as "chemical-exchange". The chemical-exchange phenomenon has three different regimes, *i.e.* fast, intermediate and slow regime. In the fast regime the exchange rate is larger than the change in the resonance frequency and only one peak is observed at an average frequency position. In the slow regime the exchange rate is slower than the change in frequency and separate signals are observed for each species. In the intervening regime, very broad signals are observed, where slight differences in rate dramatically influence the line shape. This regime is often referred to as the "cross-over point" as has been demonstrated in Figure 1.5.7.

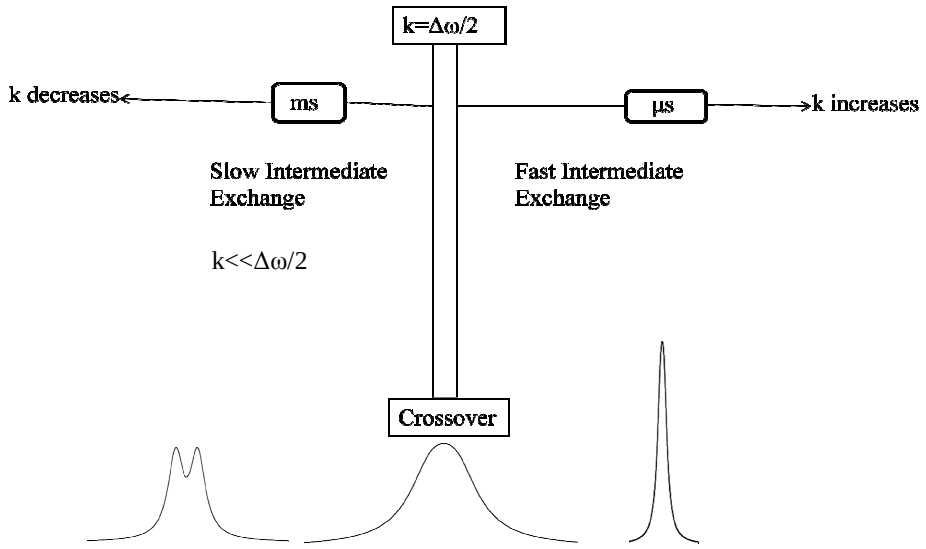

Figure 1.5.7 : Demonstration of the relation between exchange rate constant, k and the resonance frequency difference between two nuclei A and B.

Consider the Bloch equations for two distinct species A and B, the absence of chemical exchange describing the transverse component of their magnetization undergoing free precession as given by Eq. 15.12.

$$\frac{d}{dt}\widehat{M}_A^+ = [-\frac{1^A}{T_2} + i\omega_A]\widehat{M}_A^+ \,,\ \frac{d}{dt}\widehat{M}_B^+ = [-\frac{1^B}{T_2} + i\omega_B]\widehat{M}_B^+ \qquad (1.5.12)$$

where ω_A, ω_B are the resonance frequencies of A and B. $\frac{1^A}{T_2}$ and $\frac{1^B}{T_2}$ are their transverse relaxation rates. When chemical exchange occurs between A and B, as:

$$A \underset{k}{\overset{k}{\rightleftharpoons}} B$$

Eq. 1.5.12 can be rewritten as:

$$\frac{d}{dt}\widehat{M}_A^+ = \left[-\frac{1^A}{T_2} + i\omega_A - k\right] M_A^+ + kM_B^+$$

$$\frac{d}{dt}\widehat{M}_B^+ = \left[-\frac{1^B}{T_2} + i\omega_B - k\right] M_B^+ + kM_A^+ \qquad (1.5.13)$$

The solution to Eq. 1.5.13 illustrates that the line width (W) is governed by the relation:

$$w\,\alpha = \frac{1}{T_2} + k - d = \frac{1}{T_2} + k - \sqrt{k^2 - \frac{\Delta\omega^2}{4}} \qquad (1.5.14)$$

where $\Delta\omega = \omega_A - \omega_B$ and $\Delta\nu = 2\pi\Delta\omega$

When the exchange rate is smaller than $\Delta\nu = \pi\Delta\omega$, d is imaginary directly affecting the line position, and k contributes directly to the linewidth. Thus in the slow to intermediate exchange regime the line moves to the average frequency and broadens with increasing k. Once the exchange rate k is larger than the $\Delta\nu$, then d is real, subtracting from the direct contribution to the width from k, and the frequency remains unchanged.

In this case the line position is at the average frequency and narrows with increasing k. It is demonstrated in Figure 1.5.8.

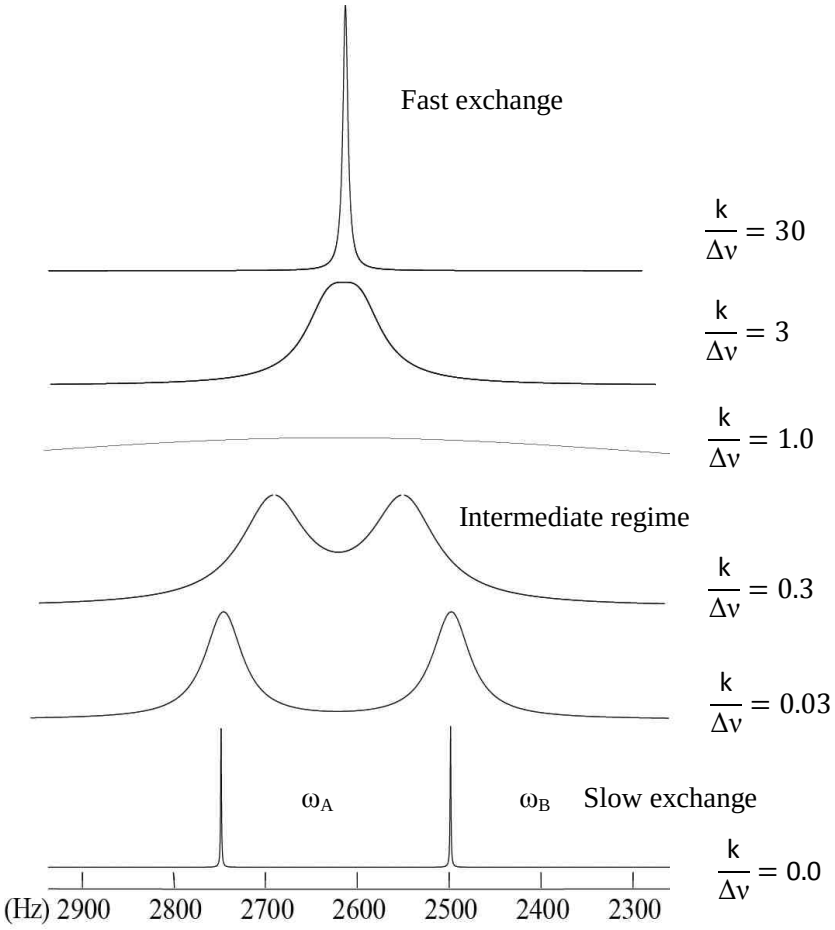

Figure 1.5.8: Demonstration of the Chemical Exchange process through simulation spectra on NMR time-scale

The rate constant 'k', can be determined by simulating the line shape for various rates. As series of rates measurements can be made over a range of temperatures. The activation parameters can be determined using the Eyring equation

$$k = \frac{k_b T}{h} e^{\frac{-\Delta G^{\dagger}}{RT}} \qquad (1.5.15)$$

Where k_b is the Boltzmann constant, h is Plank's constant, and $\Delta G^{\dagger}$ is change in the Gibbs energy from the equilibrium geometry to the transitions state, from which the entropy and enthalpy of activation can be derived.

1.5.1.6 Solid-state NMR interaction tensors

Solid-state NMR interactions can be defined as:

$$\hat{\mathbf{H}} = \vec{\mu}_i \cdot \vec{B} \tag{1.5.16}$$

for single spin interaction with externally applied magnetic field, or

$$\hat{\mathbf{H}} = r_{ij}^{-3}(\vec{\mu}_i \cdot \vec{\mu}_j) \tag{1.5.17}$$

for two spins undergoing some coupling interaction. The interactions in Eq. 1.5.12 and Eq. 1.5.13 can be given in a general way as in Eq. 1.5.18.

$$\hat{\mathbf{H}} = C \cdot \vec{\mathbf{I}}_i \cdot \hat{\hat{\mathbf{A}}} \cdot \vec{\mathbf{I}}_j \tag{1.5.18}$$

where $\hat{\mathbf{H}}$ is the Hamiltonian, C is a constant, $\vec{\mathbf{I}}$ is the spin vector and $\hat{\hat{\mathbf{A}}}$ is defined as a tensor (matrix).

All solid-state NMR interactions are anisotropic in nature and hence can be described as Cartesian tensors, which is a 3×3 matrix in the form shown in Eq.1.5.19.

$$\hat{\hat{\mathbf{A}}} = \begin{bmatrix} A_{xx} & A_{xy} & A_{xz} \\ A_{yx} & A_{yy} & A_{yz} \\ A_{zx} & A_{zy} & A_{zz} \end{bmatrix} \tag{1.5.19}$$

The tensor $\hat{\hat{\mathbf{A}}}$ given in Eq. 1.5.19 can be converted to the principal axis system (PAS) as given in Eq. 1.5.20 and has been shown in Fig 1.5.9.

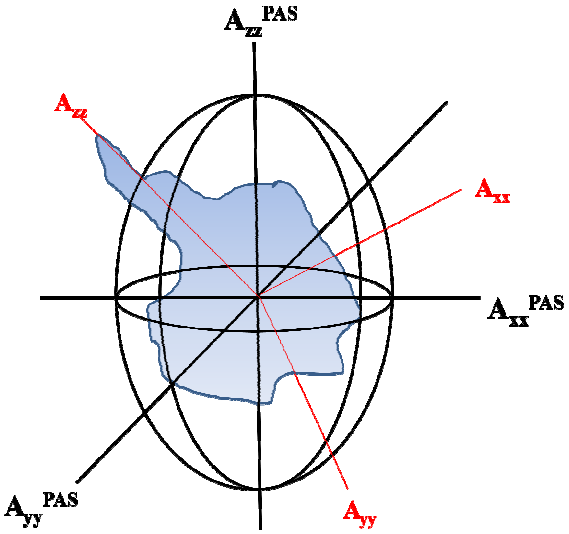

Figure 1.5.9 Transfer of a Cartesian tensor components to the principal axis tensor components

$$\hat{\hat{A}} = \begin{bmatrix} A_{xx}^{PAS} & 0 & 0 \\ 0 & A_{yy}^{PAS} & 0 \\ 0 & 0 & A_{zz}^{PAS} \end{bmatrix} \tag{1.5.20}$$

The tensor in its PAS form, Equation 1.5.20, can be further decomposed into three components represented shown in Eq. 1.5.21 and Eq. 1.5.22.

$$\hat{\hat{\mathbf{A}}} = \begin{bmatrix} A_{iso} & 0 & 0 \\ 0 & A_{iso} & 0 \\ 0 & 0 & A_{iso} \end{bmatrix} + \begin{bmatrix} A_{xx}^{PAS} - A_{iso} & 0 & 0 \\ 0 & A_{yy}^{PAS} - A_{iso} & 0 \\ 0 & 0 & A_{zz}^{PAS} - A_{iso} \end{bmatrix} \tag{1.5.21}$$

or

$$\hat{\hat{\mathbf{A}}} = A_{iso} \begin{bmatrix} 1 & 0 & 0 \\ 0 & 1 & 0 \\ 0 & 0 & 1 \end{bmatrix} + (A_{aniso}) \begin{bmatrix} -\frac{1}{2}(1-\eta) & 0 & 0 \\ 0 & -\frac{1}{2}(1+\eta) & 0 \\ 0 & 0 & 1 \end{bmatrix} \tag{1.5.22}$$

where,

$$A_{iso} = \frac{(A_{xx}^{PAS}+A_{yy}^{PAS}+A_{zz}^{PAS})}{3}, A_{aniso} = A_{zz}^{PAS} - A_{iso} \text{ and } \eta = \frac{A_{xx}^{PAS}-A_{yy}^{PAS}}{A_{zz}^{PAS}-A_{iso}} \quad (1.5.23)$$

In Eq. 1.5.23, A_{iso} is referred to as the isotropic component, A_{aniso} is the anisotropic component and η is defined as the asymmetry parameter of $\hat{\hat{\mathbf{A}}}$. A_{aniso} and η govern the orientational dependence of $\hat{\hat{\mathbf{A}}}$ and A_{iso} is the uniform average over all orientations.

1.5.1.7 Chemical Shift

The magnetic field, a nucleus experiences, is a combination of the applied field and those due to the electron motion surrounding them. The applied magnetic field induces current in electron densities of molecules, which in turn induces magnetic field that either decreases or increases net field the nucleus experiences. This induced magnetic field is directly proportional to the applied magnetic field, $\vec{B}_{induced} = \hat{\hat{\boldsymbol{\sigma}}}\vec{B}$, where $\hat{\hat{\boldsymbol{\sigma}}}$ is the shielding tensor. The effective magnetic field can therefore be expressed according to Eq. 1.5.24.

$$\vec{B}_{eff} = \vec{B} - \hat{\hat{\boldsymbol{\sigma}}}\vec{B} = \vec{B}\left(1 - \hat{\hat{\boldsymbol{\sigma}}}\right) \quad (1.5.24)$$

The chemical shift for a particular nucleus relative to a standard reference compound can be defined by using the following convention:

$$\delta_i = \frac{\omega_i - \omega_{ref}}{\omega_{ref}} \times 10^6 \text{ parts per million (ppm)} \quad (1.5.25)$$

$$\delta_i = \frac{\sigma_{ref} - \sigma_i}{\sigma_{ref}} \times 10^6 \text{ ppm} \quad (1.5.26)$$

where ω_i is the resonance frequency of the nucleus under externally applied magnetic field $\vec{B}$ and ω_{ref} is the resonance frequency of same nucleus in a standard compound. The relative chemical shift is defined with reference to a standard compound, which is defined to be at 0 ppm. For example, tetramethylsilane (TMS) is usually used as a standard for ^{1}H and ^{13}C NMR spectroscopy and its chemical shift value is taken as zero. The chemical shift scale is made more manageable by expressing the chemical shifts in parts per million (ppm) which is independent of the spectrometer frequency as shown in Eq. 1.5.25 and 1.5.26.

The induced magnetic field at the nucleus depends on structure of the electron density surrounding it, and the applied magnetic field strength and direction. Thus the degree of shielding depends on the molecular orientation with respect to the magnetic field, defined by the euler angles α, β, γ , and the magnitude of the applied field as given in Eq. 1.5.27.

$$\vec{B}_{induced} = \hat{\hat{\boldsymbol{\sigma}}}(\alpha, \beta, \gamma)\vec{B} \tag{1.5.27}$$

Hence, the average shielding can be given by the chemical shielding tensor ($\hat{\hat{\boldsymbol{\sigma}}}$**).**

The Hamiltonian for the chemical shift can be given according to Eq. 1.5.28.

$$\hat{\mathbf{H}}^{cs} = \gamma \cdot \vec{I} \cdot \hat{\hat{\boldsymbol{\sigma}}} \cdot \vec{B} \tag{1.5.28}$$

In solution-state experiments, an isotropic chemical shift is observed while in the solid-state a powder pattern is observed, because the nuclei may have different fixed orientations in 3-D space in the solid-state, and each orientation will give a different chemical shift based on its position. The isotropic chemical shift, the chemical shift

anisotropy (δ_{aniso}) and the asymmetry parameter (η) are defined in Eq. 1.5.30, 1.5.31 and 1.5.32 respectively.

$$\hat{\hat{\delta}}^{PAS} = \begin{bmatrix} \delta_{xx}^{PAS} & 0 & 0 \\ 0 & \delta_{yy}^{PAS} & 0 \\ 0 & 0 & \delta_{zz}^{PAS} \end{bmatrix} \quad (1.5.29)$$

$$\delta_{iso} = \frac{(\delta_{xx}^{PAS} + \delta_{yy}^{PAS} + \delta_{zz}^{PAS})}{3} \quad (1.5.30)$$

$$\delta_{aniso} = \delta_{iso} - \delta_{zz}^{PAS} \quad (1.5.31)$$

$$\eta = \frac{\delta_{yy}^{PAS} - \delta_{xx}^{PAS}}{\delta_{aniso}} \quad (1.5.32)$$

where $\delta_{zz}^{PAS}$is defined as the farthest component from the isotropic chemical shift, δ_{yy}^{PAS} is the closest component from the isotropic chemical shift δ_{iso} and the third part is δ_{xx}^{PAS}, defined in the principle axis system (PAS).

$$\delta_{zz}^{PAS} \geq \delta_{xx}^{PAS} \geq \delta_{yy}^{PAS} \quad (1.5.33)$$

The effect of the asymmetry parameter on the shape of the solid-state NMR spectrum is shown in Figure 1.5.10.

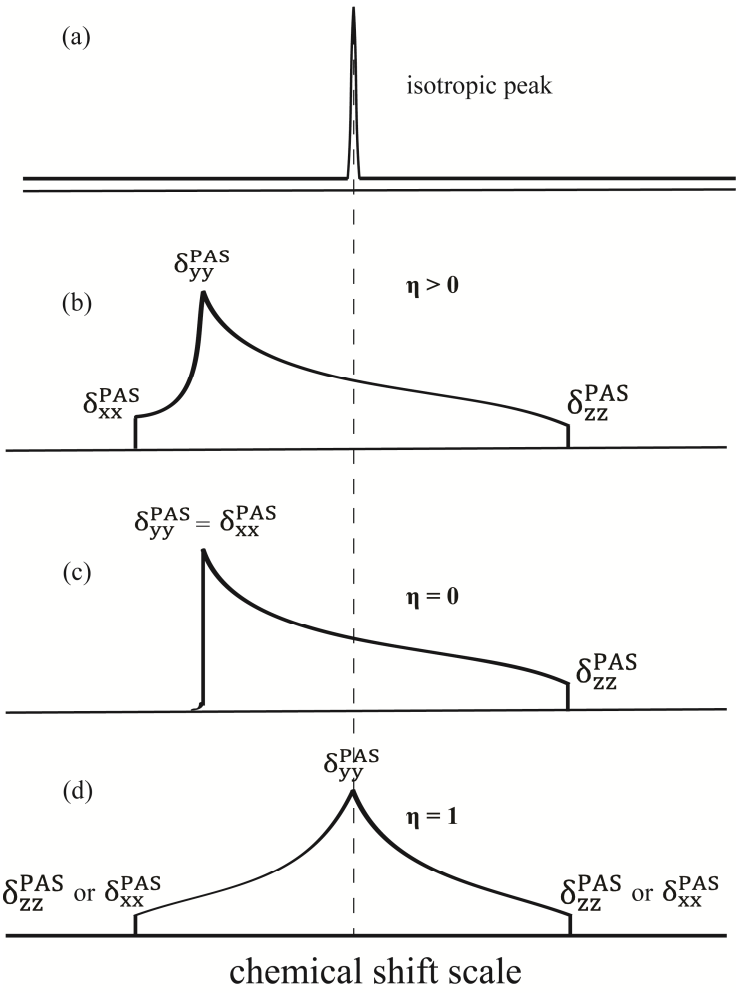

Figure 1.5.10: Powder pattern corresponding to different chemical shielding interactions. a) The spectrum resulting from fast isotropic motion; b) the powder pattern resulting in the case of the asymmetry parameter being greater than zero; c) the powder pattern resulting in the case of the asymmetry parameter being equal to zero (axial symmetry); d) the powder pattern resulting in the case of the asymmetry parameter equal to one.

1.5.1.8 Scalar Coupling (*J*-coupling)

Scalar-coupling, i.e., *J*-coupling, between two nuclei is facilitated by the surrounding electrons. This is in contrast to the dipolar interaction, which is a direct interaction between two nuclei through space. In solution, if a spin-½ nucleus couples with n neighboring spin-½ nuclei, its signal will be split into n+1 peaks with an intensity

pattern given by the binomial expression $(a+b)^n$, where n is the total number of neighboring nuclei. The spacing between the peaks is given by the *J*-coupling constant usually expressed in Hz as it is field independent.

In the solid state the Hamiltonian for *J*-coupling interaction can be expressed as Eq. 1.5.34.

$$\hat{\mathbf{H}} = 2\pi \cdot \hat{\mathbf{I}}_1 \cdot \hat{\hat{\mathbf{J}}} \cdot \hat{\mathbf{I}}_2 \tag{1.5.34}$$

where $\hat{\mathbf{I}}_1$ and $\hat{\mathbf{I}}_2$ are the two spin vectors and $\hat{\hat{\mathbf{J}}}$ is the scalar or *J*-coupling tensor. The *J*-coupling tensor is not traceless. As a result, in solution, *J*-coupling is observed.

J-coupling is an intramolecular phenomenon. Two spins have a measurable *J*-coupling only if they are linked together through a small number of chemical bonds. The *J*-coupling has either a positive or negative sign. The positive value of *J*-coupling indicates that spin-spin coupling is stabilized; decreasing the energy of the system and the negative value of *J*-coupling is destabilized, increasing the energy of the system. In the case of anisotropic liquids and solids, the anisotropic part of *J*-coupling is observed and is called J_{aniso} (ΔJ). In the principal axis system, *J*-coupling can be treated according to the theory defined in section 1.5.1.6 and can be given by Eq. 1.5.35.

$$\hat{\hat{\mathbf{J}}}^{\boldsymbol{PAS}} = J_{iso}\begin{bmatrix}1 & 0 & 0\\ 0 & 1 & 0\\ 0 & 0 & 1\end{bmatrix} + (\Delta J)\begin{bmatrix}-\frac{1}{2}(1-\eta_j) & 0 & 0\\ 0 & -\frac{1}{2}(1+\eta_j) & 0\\ 0 & 0 & 1\end{bmatrix} \tag{1.5.35}$$

$$\text{where } \Delta J = J_{zz}^{PAS} - J_{iso} \text{ and } \eta_j = \frac{J_{yy}^{PAS} - J_{xx}^{PAS}}{J_{zz}^{PAS} - J_{iso}} \tag{1.5.36}$$

The *J*-coupling anisotropy ΔJ combined with the dipolar coupling can have a dramatic effect on the intensities of the peaks in solid-state NMR spectra. Sometimes *J*-

coupling is not observed, (in spite of the resolution being sufficient to resolve them) because of (i) rapid forming and reforming of the chemical bonds so that a particular nucleus jumps in between different molecules, also called fast chemical exchange, (ii) the nuclear spin under observation undergoes rapid longitudinal relaxation due to the presence of a quadrupolar nucleus, or (iii) poor resolution due to the presence of large dipolar coupling, because the *J*-couplings are of the order of Hz while the dipolar couplings are of the order of several kHz.

1.5.1.9 Dipolar coupling

The dipolar interaction (D) between two magnetic moments of is defined as.

$$\hat{\mathbf{H}} = b_{12}(3(\hat{\mathbf{I}}_1 \cdot \vec{e}_{12})(\hat{\mathbf{I}}_2 \cdot \vec{e}_{12}) - \hat{\mathbf{I}}_1 \cdot \hat{\mathbf{I}}_2) \quad (1.5.37)$$

where $\hat{\mathbf{I}}_1$ and $\hat{\mathbf{I}}_2$ are the two spin vectors and $\vec{e}_{12}$ is the internuclear vector orientation.

In general, to the first order accuracy, Eq. 1.5.37 can be expressed as:

$$\hat{\mathbf{H}} = b_{12}\frac{1}{2}(3\cos^2\theta - 1)(3\hat{\mathbf{I}}_{1z}\hat{\mathbf{I}}_{2z} - \hat{\mathbf{I}}_1 \cdot \hat{\mathbf{I}}_2) \quad (1.5.38)$$

where b_{12} is the strength of the dipolar coupling:

$$b_{12} = \frac{\mu}{4\pi}\frac{\gamma_j\gamma_k\hbar}{r_{jk}^3} \quad (1.5.39)$$

and the orientational dependence is expressed in terms of $\frac{1}{2}(3\cos^2\theta - 1)$,where θ is the angle between the internuclear vector and the applied field. Furthermore, the dipolar coupling strength depends on the inverse cube of the internuclear distance, hence measurement of these couplings are invaluable in structural studies.

1.5.1.10 Magic Angle Spinning

In solution NMR experiments the effects of chemical shift anisotropy, heteronuclear dipolar couplings, and homonuclear dipolar couplings average out due to rapid tumbling of the molecules. In solid-state NMR spectroscopy, however, the above mentioned phenomena give rise to very broad spectral lines. To average out these effects in solid-state NMR spectroscopy the sample is spun about an axis that is oriented at an angle of 54.74° from the vertical axis of the applied magnetic field (B_o). This angle is called the magic angle which is defined by the orientation of the body diagonal in a cube (Figure 1.5.11).

In order to suppress the homonuclear dipolar broadening the spinning of the sample at the magic angle should be at a rate equal to or greater than the dipolar line widths, because under this condition it will have the equal chances of being in X, Y and Z axis and thereby averaging out the orientation dependence. Spinning the sample at the magic angle with respect to the applied field (B_o**)** still has limited use for high-γ nuclei like ^{1}H and ^{19}F, which may have dipolar coupling strengths of hundreds of kHz.

It was seen previously the orientational dependence of every term in NMR Hamiltonian depends on $[\frac{1}{2}(3\cos^2\theta - 1)]$. Thus these interactions can be eliminated to first order accuracy is the following condition is met.

$$\frac{1}{2}(3\cos^2\theta - 1) = 0 \qquad (1.5.40)$$

This occurs when $\theta = 54.74°$, hence the magic angle. When spinning sufficiently fast all orientations are effectively averaged to this angle.

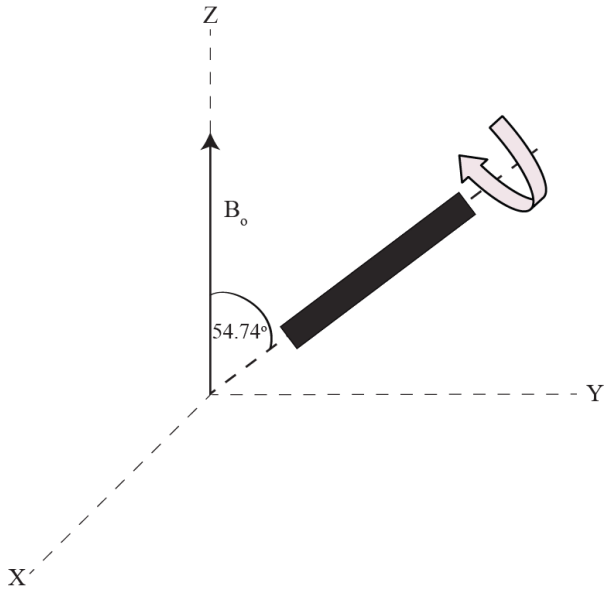

Figure 1.5.11: Demonstration of magic angle with respect to the applied magnetic field (B_z)

1.5.1.11 Quadrupolar Coupling

A nucleus with spin > ½ is called a quadrupolar nucleus, due its electric quadrupole moment resulting from its non-spherical shape. The nuclear electric quadrupole interacts with electric field gradients produced by the surrounding electrons and, giving rise to an additional term in $\hat{\mathbf{H}}$. As the electric field gradient is a function the electron density, it is an orientationally dependent; therefore, the quadrupolar coupling interaction is orientationally dependent as described by the qudrupolar coupling tensor.

The Hamiltonian for quadrupolar coupling can be given according to Eq. 1.5.41.

$$\hat{\mathbf{H}} = \frac{eQ}{2I(2I-1)} \hat{\mathbf{I}} \cdot \hat{\boldsymbol{\omega}}_j^{\mathbf{Q}}(\boldsymbol{\theta}) \cdot \hat{\mathbf{I}} \qquad (1.5.41)$$

where $\hat{\boldsymbol{\omega}}_j^{\mathbf{Q}}(\boldsymbol{\theta})$ is the quadrupolar coupling tensor and $\hat{\mathbf{I}}$ is the spin vector of quadrupolar nucleus, eQ is the electric quadrupole moment of the nucleus. This can be analyzed in the

same way as the dipolar coupling tensor and has an isotropic value which is averaged out to zero but has a an asymmetry parameter and quadrupolar coupling tensor. The first order quadrupolar coupling can be defined as Eq. 1.5.42.

$$\boldsymbol{\omega_j^Q(\theta)} = \frac{3\pi C_q}{\mathbf{I(2I-1)}} \times \frac{\mathbf{1}}{\mathbf{2}}(3\cos^2\theta - 1) \qquad (1.5.42)$$

where C_q is the quadrupolar coupling constant. In the absence of a magnetic field, the nuclear spin states of a quadrupolar nucleus are not degenerate in the presence of an electric field gradient. This electric field gradient depends on the local electron-density and thus is strongly dependent on molecular structure. For instance molecules with high symmetry, such as tetrahedral systems, will not have an electric field gradient at the nucleus of the central atom, in which case, the spin states are degenerate just as a spin-½ nucleus. Rapid motion such as molecular reorientation and vibrations can lead to dramatic modulations in electric field gradient. These in turn give rise to time independent variations in quadrupolar coupling interaction which can be a very efficient relaxation pathway. As a result, quadrupolar nuclei can be difficult to observe in solution-state and often cause neighboring spin-½ nuclei coupled to them to relax much faster broadening their lines in the spectrum. For example the N–H protons of secondary amines are difficult to observe whereas those of NH_4^+ salts can give rise to nice sharp 1:1:1 triplet.

In the solid-state quadrupolar nuclei can be observed requiring a very large frequency shift range requiring specialized pulse sequences such as the quadrupolar-echo. The discussion of these methods are beyond the scope of the present work. However, the, the effect of dipolar coupling of a quadrupolar nucleus to a spin-½ nucleus on the spectrum of the spin-½ needs some discussion. Even though the dipolar coupling in this

case can be very weak, magic angle spinning (see section 1.5.3) cannot remove them effectively - no matter how fast the sample is spun. This is known as residual coupling effect, which is a consequence of the magic angle in the lab frame is being the same as the magic angle in the combined lab-quadrupolar frame, and hence the isotropic averaging of this coupling cannot be achieved. As a result the spectrum of a spin-½ nucleus manifests these residual coupling as unequally spaced multiplets, where each line has a unique shape reflecting a very narrow powder pattern.

If a quadrupolar nucleus A, with spin S is coupled with a spin-½ nucleus X, and their $\hat{\hat{\mathbf{J}}}$ and $\hat{\hat{\mathbf{D}}}$ are coaxial, then the splitting of the states of the spin-½ nucleus may be given by the Eq. 1.5.43 and 1.5.44.

$$\nu(\mathrm{m_s}) = \nu_\mathrm{X} - \mathrm{m_A} J_{iso} + \frac{3\mathrm{D}'\omega_\mathrm{j}^\mathrm{Q}}{20\nu_\mathrm{s}}\left[\frac{2\mathrm{S(S+1)}-3\mathrm{m_A^2}}{2(2\mathrm{S}-1)}\right] \tag{1.5.43}$$

$$\nu(\mathrm{m_s}) = \nu_\mathrm{X} - \mathrm{m_s} J_{iso} + \mathrm{K(S, m_A)} \tag{1.5.44}$$

where ν_X is the Larmor frequency of spin-1/2 nucleus, J_{iso} is the isotropic part of the $\hat{\hat{\mathbf{J}}}$. The constant $\mathrm{K(S, m_A)}$ is defined as Eq (1.5.45).

$$\mathrm{K(S, m_A)} = \frac{3\mathrm{D}'\omega_\mathrm{j}^\mathrm{Q}}{20\nu_\mathrm{s}}\left[\frac{2\mathrm{S(S+1)}-3\mathrm{m_A^2}}{2(2\mathrm{S}-1)}\right] \tag{1.5.45}$$

and D' is the effective dipolar coupling constant defined as given in Eq. 1.5.46,

$$\mathrm{D}' = \mathrm{D} - \Delta\mathrm{J}/3 \tag{1.5.46}$$

where $\Delta\mathrm{J}$ is defined as anisotropy in scalar coupling. $\mathrm{K(S, m_A)}$ can be defined as the second-order shift which depends on $\mathrm{m_A^2}$. If $\mathrm{m_A} = \pm\mathrm{S}$, $\mathrm{K(S, m_A)}$ becomes:

$$\mathrm{K(S, m_A)} = \Delta = -\frac{3\omega_\mathrm{j}^\mathrm{Q}\mathrm{D}'}{20\nu_\mathrm{s}} \tag{1.5.47}$$

Thus, the second order shift from equation (1.5.43) may be given as:

$$^{2}\Delta\nu(m_s)= \nu(m_A) - \nu_X + m_A J_{iso} = -\Delta[\frac{2S(S+1)-3m_A^2}{2(2S-1)}] \qquad (1.5.48)$$

For example the coupling of nucleus A (spin-3/2) with the nucleus X (spin-½) can be given as:

$$\hat{H}_j^Q \cong \frac{\omega_j^Q}{6}(3\hat{\mathbf{I}}_{\mathbf{jz}}^{\mathbf{2}} - \hat{\mathbf{I}}_{\mathbf{j}}\cdot\hat{\mathbf{I}}_{\mathbf{j}}) \qquad (1.5.49)$$

In case of isotropic liquids $\omega_j^Q = 0$. In case of solids, ω_j^Q is given as in Eq. 1.5.50.

$$\omega_j^Q = \frac{3eQ\bar{V}_{zz}(\theta)}{4S(2S-1)} \qquad (1.5.50)$$

where S is the spin of the quadrupolar nucleus. Energy level diagram and the effect of residual dipolar coupling on the *J*-coupling pattern is shown in Figure 1.5.12 and 1.5.13.

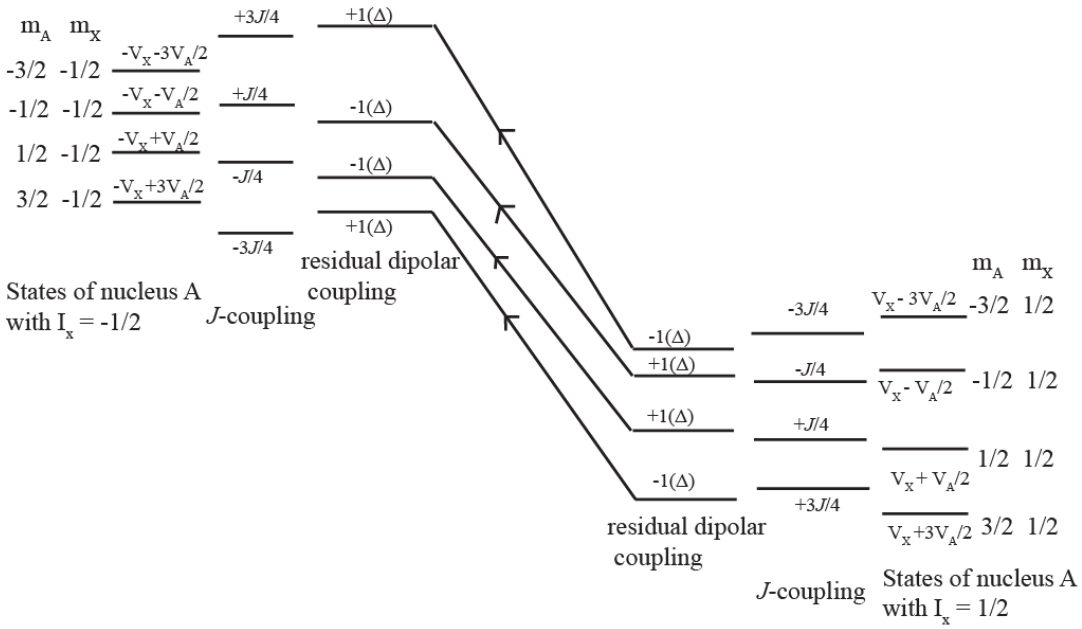

Figure 1.5.12: Effect of the coupling of a quadrupolar nucleus A (spin-3/2) to a nucleus X (spin-1/2) on the energy levels of the spin-1/2 nucleus X. 'ν' represents the frequency, *J*, the scalar coupling and Δ, residual dipolar coupling.

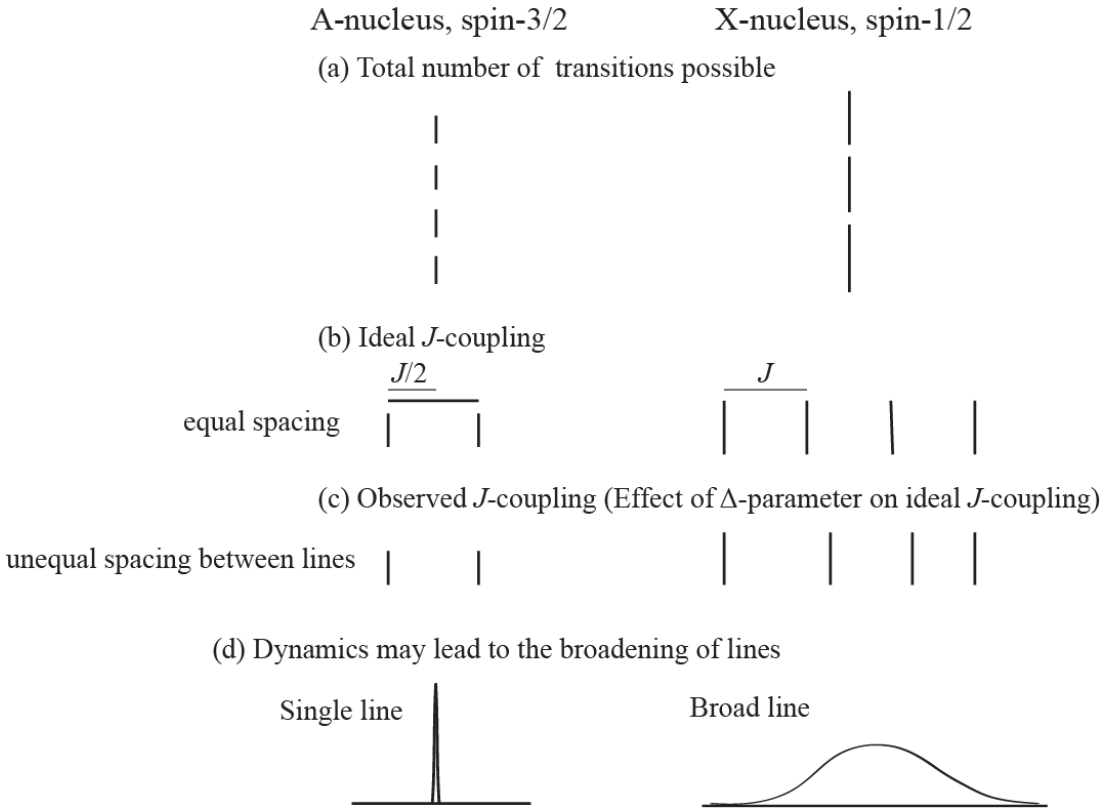

Figure 1.5.13: Effect on the *J*-coupling of spin-1/2 nucleus (X) due to the coupling of a quadrupolar nucleus A (spin-3/2) to a spin-1/2 nucleus (X). *J* is the scalar coupling and Δ is the residual dipolar coupling.

1.5.2 Pulses

A radio-frequency pulse can be defined as composed of an electric component as well as a magnetic component, as it is an electromagnetic wave having a sinusoidal function. A radio-frequency pulse rotates the bulk magnetization around the x-axis if the pulse is applied along the x-axis. The angle of rotation is proportional to the duration of the radio-frequency pulse applied. Depending on the length of the pulses and delay between the pulses, different rotations of the magnetization vector can be produced.

Depending on the frequency of the radio-frequency pulse, different nuclei are measured, e.g., ^{1}H, ^{15}N, ^{13}C, etc. A pulse is used to create coherences for a NMR signal.

1.5.3 Direct Polarization

Direct polarization (DP) is the most common experiment in NMR spectroscopy where a 90° pulse is applied on a nucleus, rotating its z-magnetization (I_z) by 90° to -Y axis from its original position (i.e. Z-axis). During the return of magnetization to its original position an FID (Free Induction Decay) is recorded in the XY plane of the signal as a function of time (Fig 1.5.14). Usually the DP spectrum is recorded by simultaneously decoupling the other nuclei, which have direct *J*-coupling and dipolar-coupling interaction with the observed nucleus. This spectrum can also be recorded without decoupling, depending on the information required (about *J*-coupling etc).

If the observed nucleus is completely decoupled from all other interactions, the information about exact CSA of the observing nucleus can be obtained. In the case of partial decoupling, the FID may contain information about CSA and dipolar couplings to the remaining nuclei.

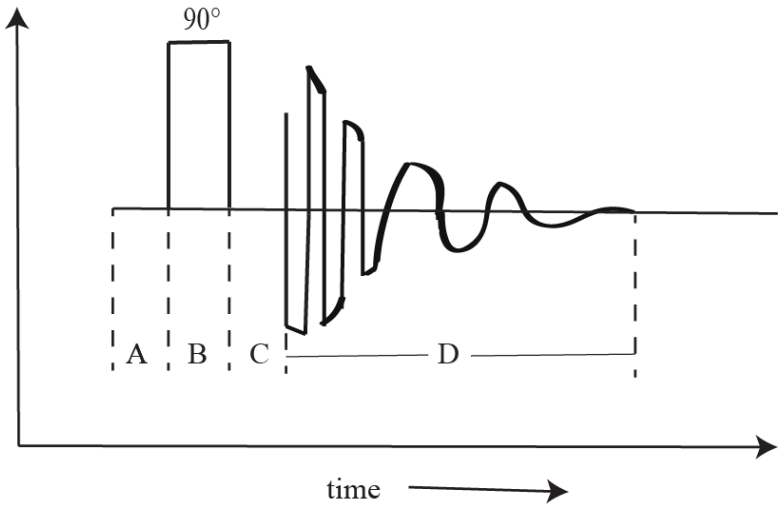

Figure 1.5.14: Demonstration of direct polarization experiment sequence. A is the preparation time for 90° pulse, B is the time duration of 90° pulse, C is the predelay in the acquisition of signal and D is the time to acquire FID signal.

1.5.4 Cross Polarization

Cross polarization (CP) is a technique to transfer polarization from one spin to another spin through the proper match of the Hartmann-Hahn condition (Figure 1.5.13). Cross polarization combined with MAS (CPMAS) can provide very useful information, not only giving an enhancement in signal intensity in very short time but also providing highly resolved spectra. Cross polarization is difficult at an MAS speed at which all the CSA interactions are removed.

Generally, CP is a technique in which polarization of a highly abundant spin-active nucleus (^{1}H or ^{19}F) is transferred to a dilute-spin (^{13}C, ^{15}N etc.) nucleus to observe its signal with improved signal-to-noise ratio. Dilute-spin nuclei generally have low sensitivity due to (a) low natural abundance, and (b) low gyromagnetic ratios. Also, these nuclei have very long relaxation times because of the much weaker heteronuclear dipolar

interactions. The dipolar interactions contribute towards relaxation, thus, the dipolar coupling strength can be related to the relaxation process.

One important advantage of the cross polarization experiments is that after cross polarization the relaxation time (T_1) of the dilute-spin nucleus depends on the relaxation time of the abundant nucleus, which is usually much shorter than that of the dilute-spin nucleus. The main disadvantage of the cross polarization experiment is that the signal intensities are not proportional to the number of spins in different environments, i.e., these intensities are not quantitative.[51]

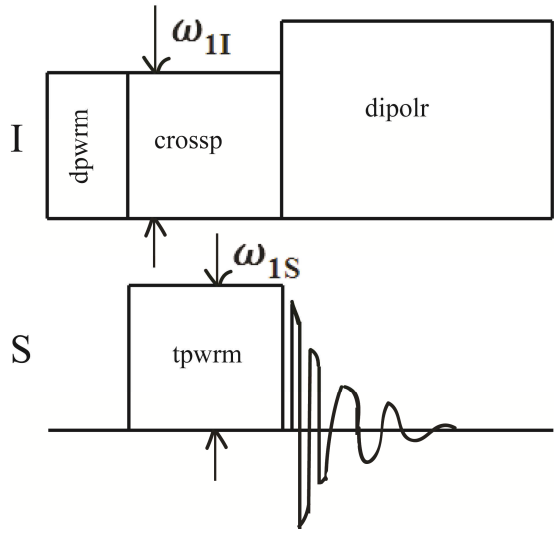

Figure 1.5.15 Demonstration of cross polarization experiment sequence. Where dpwrm - ^{1}H 90° pulse, dipolr- decoupling power, tpwrm - ^{13}C 90° pulse with decreased power, crossp = matching conditions of the powers for ^{1}H and ^{13}C nuclei.

Cross polarization occurs via dipolar interactions, i.e., interaction through space, between a highly abundant nucleus, e.g., ^{1}H and a low-abundant nucleus, e.g., ^{13}C. First a ^{1}H 90° pulse is applied which rotates magnetization from z axis to –y axis (Fig 1.5.15). Once it is along this axis, another pulse is applied on the y-axis whose magnetic field

helps to keep this magnetization vector in the same position. This situation is called "spin-lock" and the magnetic field generated by the above applied pulse is known as "spin-lock field" [$B_1(^1H)$]. With the spin lock in place a pulse is applied on the X-channel [with field B_1^X (contact)]. The time during which these two pulses are applied together is called **"**contact-time**"**. After the contact time, the ^{1}H-irradiation is extended to decouple protons with field [$B_1(^1H)${decouple}] while observing nucleus X on the other channel. For efficient cross polarization the radiofrequency fields for ^{1}H and ^{n}X should be matched as shown in Eq. 1.5.51.

$$\gamma^H B_1^H = \gamma^X B_1^X \quad \text{[Hartmann-Hahn Match]} \qquad (1.5.51)$$

To set this match either B_1^X or B_1^H can be varied. But the safest way is to vary B_1^H because γ^x is usually significantly smaller than γ^H **(**So for a matching condition according to Eq. 1.5.47, B_1^X will be the four times to B_1^H). If we set $B_1^H(90°)$, i.e., spin lock to equal to B_1^H (decouple) then the 90° pulse duration gives the field strength for decoupling protons in CP setup. For effective spin lock, B_1^H (in kHz) must be greater than the half-height line width from the static ^{1}H line. Normally these line widths are of 40 kHz. The CP enhancement can be described as follows:

$$\frac{(\frac{S}{N})^{CP}}{(\frac{S}{N})^{90°}} = \frac{\gamma_I}{\gamma_S} \qquad (1.5.52)$$

Because the gyromagnetic ratio of the proton is four times greater than that of carbon, the expected enhancement is a factor of 4 as given in Eq. 1.5.53.

$$\frac{(\frac{S}{N})^{CP}}{(\frac{S}{N})^{90°}} = \frac{\gamma_{1_H}}{\gamma_{13_C}} = 4 \qquad (1.5.53)$$

Cross polarization provides much improved sensitivity not only through the enhancement factor, which arises from the magnetization transfer from the strong

abundant nucleus, but also because the experiment can be performed on the relaxation times of the abundant nucleus which is often orders of magnitude shorter. For example, ^{1}H to ^{13}C CP can be performed as much as 10 times faster, in addition to the enhancement factor of 4, giving an overall improvement in S/N on the order of 12. Magic Angle Spinning gives much improved resolution for weak nuclei as the homogeneous broadening due to homonuclear coupling is absent. The combination of CP and MAS provides a sensitive higher resolution technique that is relatively easily implemented for routine experiment and consequently revolutionized solid-state NMR spectroscopy as a characterization method.

1.5.5 Decoupling

It is essential to get high-resolution in solid-state NMR spectroscopy. Nuclear magnetic resonance decoupling is a specific method used in NMR spectroscopy, where a sample is irradiated by a radiofrequency radiation at a certain frequency or frequency range to eliminate the effect of *J*-coupling fully or partially between certain nuclei to simplify a NMR spectrum. This effect of coupling causes NMR signals to split into multiple peaks, which are separated by several Hertz in the NMR spectrum. The application of decoupling eliminates the splitting of the signals fully or partially in the NMR spectroscopy and helps in determining the structures of chemical compounds easily. In the homonuclear decoupling, a nucleus that is being irradiated by the radio-frequency (R_f) radiation is the same as the nucleus being observed. If the coupling is fully removed, high-resolution in achieved in NMR spectroscopy. In the case of proton, windowed phase-modulated Lee-Goldburg (wPMLG) sequence is used for homonuclear

decoupling. In the heteronuclear decoupling a nucleus being irradiated by radio frequency (R_f) radiation is different than the observed nucleus. For a given nucleus, only a selected frequency range can be irradiated by a low-power radiofrequency pulse or the entire chemical shift range can be irradiated in the broad band decoupling or in the composite-pulse decoupling.

1.5.6 SIMPSON (NMR spectrum simulation program)

SIMPSON[55] is a general-purpose software package for simulation for all kinds of solid-state NMR experiments based on time-dependent quantum mechanics of nuclear spin. It computes the NMR signal by propagating the density matrix through the time and by using terms of the Hamiltonians, prescribed by the pulse sequence, and spin system. As magic angle spinning makes the Hamiltonian time dependent at each time point, the Hamiltonian is computed from which the propagator is constructed and subsequently use to propagate the density matrix through that time point. This calculation is repeated for every time point in the FID, and the FID has to be computed for each orientation. For example, for 20 possible rotor positions, points along the rotor phase with 30 crystal orientations and 1000 time points are computed giving a total of 600,000 data points for a single simulation. This process is repeated for each rotor period. These simulations were not possible in the past due to severely limited computational capabilities. The main advantage of SIMPSON is that there is no intrinsic limitation to the number of spins, but that it is limited for the secular part, because it does not include the residual dipolar coupling terms. This program uses the M. Mehring conventions[64] for all tensors to define anisotropy, asymmetry and Euler angles. The Euler angles (α, β, γ)[65] relate two

orthogonal coordinate systems having a common origin as shown in Figure 1.5.16. The usual ranges for the Euler angles (α, β, γ) are (1) $0 \leq \alpha \leq 360°$ (2) $0 \leq \beta \leq 180°$ and (3) $0 \leq \gamma \leq 360°$.

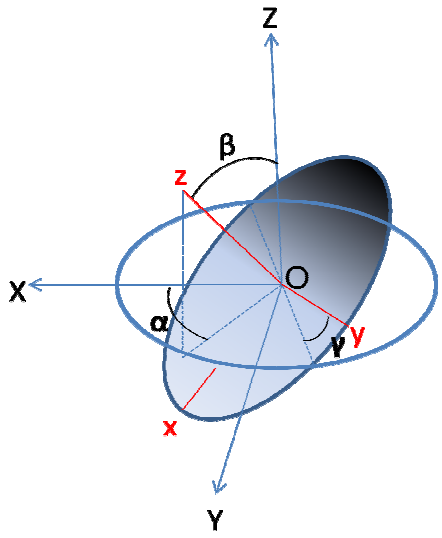

Figure 1.5.16: Presentation of the Euler angles (α, β, γ) for moving a coordinate system (X, Y, Z which represents a principal axis system) to a second coordinate system (x, y, z representing lab frame system).

The SIMPSON input file consists of the following section: (1) spinsys, (2) par, (3) pulseq, and (4) main. The '**spinsys**' section consists of information about the different channels on which the experiments are performed. It also contains the different Hamiltonians related to different interactions along with the Euler angles through which the system can be transferred from the principal axis frame to the lab frame. The **pulseq** section provides us with different propagators with which the density matrix can be propagated. In the 'main' section the simulation is compiled and the time-dependent signal is converted to the frequency domain with Fourier transformation and different processing parameters.

spinsys: The R_f channels of the experiment and the nuclei are defined by channels and nuclei using the general notation like ^{1}H, ^{19}F, ^{119}Sn, etc. Also, the interactions such as chemical shift, chemical shift anisotropy, *J*-coupling interactions, dipole interactions and quadrupole interactions as well as their orientational dependence defined by various internal nuclear Hamiltonian are included in this section which can be defined in terms of isotropic chemical shift (δ_{iso}), chemical shift anisotropy (δ_{aniso}), asymmetry (η) and different Euler angles (α, β, γ).

par: The par section consists of adjustable spectral window simulation parameters like start and detect operator, spin rate, proton Larmor frequency, sampling conditions, e.g., number of sampling points (np), spectral width (sw), number of different orientations for powder averaging, the information flow from the program ("verbose"– A row of flags that sets the level of information printed when running the simulation) and variables to define the R_f field strength and rotor synchronization.

pulseq: This part is used for external manipulations. The input can be given for any type of pulse sequence. It consists of the pulse, which includes a pulse of duration δt, R_f-field amplitude of $\omega_{RF}/2\pi$ and phase φ on the channels numbered successively. 'for' is defined to denote how many times to collect the data (e.g. to a limit of total number of points np). 'delay' defines the current propagator to include a free precession period of time δt. 'max dT' denotes the maximum time step over which the Hamiltonian may be considered time independent. 'acq', collects a data point corresponding to the detection operator.

main: This part is concerned with the experiment processing to compute the calculations and obtain the result in terms of the defined dimensions for the spectrum, e.g., 1D or 2D

etc. The simulation is started using the command ‘fsimpson’, which returns the dataset resulting from the SIMPSON calculation. The data set may be saved by using the command, ‘fsave’. Other useful commands for this section are, ‘fft’, used for fast Fourier transformation, ‘fzerofill’ for zero-filling, ‘fphase’ for phasing, ‘fbc’ for baseline correction, ‘faddlb’ for apodization (multiplying the signal by a function usually exponential to increase signal to noise ratio) etc. Here we can also combine two FID’s by using ‘fadd’ command or can subtract two FID’s using ‘fsub’ command.

The actual simulation process can be defined as (1) the computation of the density matrix at time t is performed with the help of propagator u(t) and the initial density matrix ρ(0), defined as $\rho(t) = u(t)\rho(0)u(t)^{-1}$, (2) the trace of $[I_+\rho(t)]$ matrix is computed, (3) step(2) provides a time dependent signal s(t), (4) L.B. and G.B. functions are performed on s(t) to give a modified time dependent signal (5) this time dependent signal is converted to the frequency domain by Fourier transformation.

$$\rho(0) \xrightarrow{u(t)} \rho(t) \longrightarrow Tr[I_+\rho(t)] \longrightarrow s(t) \xrightarrow{L.B., G.B.} s'(t) \xrightarrow{F.T.} s(\nu)$$

A typical input file for the SIMPSON simulation has been given on page 45 and its result with the experimental spectrum has been shown in Figure 1.5.13.

Typical SIMPSON simulation input file for $^{119}Sn\{^1H\}$ solid-state NMR spectrum at MAS-19 kHz has been shown on page 46 and the resulted spectrum is shown in Figure 1.5.17on page 49.

SIMPSON simulation input file for ^{119}Sn{^{1}H} solid-state NMR spectrum at MAS 24 kHz

```
spinsys {
channels 119Sn 19F
nuclei 119Sn 19F  19F
shift 1 424 -39500 0.60 0 165 0
shift 2 -293 -26000 0 0 0 0
shift 3 -293 -26000 0 0 15 0
jcoupling 1 2 1320 -800 0 0 0 0
jcoupling 1 3 1320 3200 0 0 0 0
jcoupling 2 3 0 0 0 0 0 0
dipole 1 2 4266 0 0 0
dipole 1 3 3200 0 0 0
dipole 2 3 -1152 0 0 0       }
par {
   start_operator          I1z
   detect_operator         I1m
   sw                      500000
   spin_rate               24000
   gamma_angles            20
   variable dwell          1e6/sw
   crystal_file            rep30
   np                      1024
   verbose                 1101
   variable rf1            138888.8
   variable t90            0.25e6/rf1
   proton_frequency        500.13e6
}
proc pulseq {} {
  global par
  maxdt 1.0
  reset
 pulse $par(t90) $par(rf1) x 0 0
  acq
  for {set i 1} {$i < $par(np)} {incr i} {
  delay $par(dwell)
  acq }  }
proc main {} {
global par
set f [fsimpson]
fzerofill $f 32768
faddlb $f 300 0.5
fft $f
fphase $f -rp -13 -lp -130 -scale 200.06
fsave $f $par(name).spe
}
```

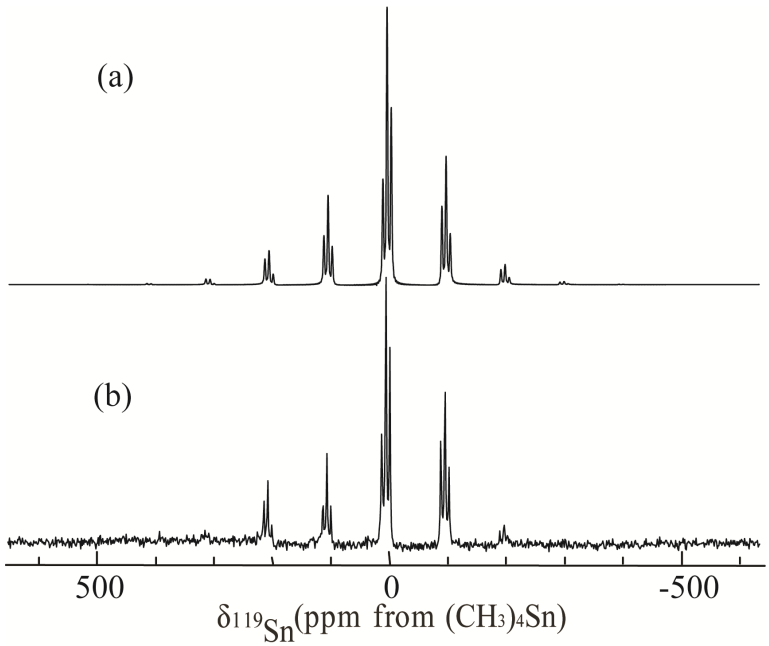

Figure: 1.5.17 $^{119}Sn\{^{1}H\}$ MAS NMR spectra of Me_3SnF at a spinning rate of 19 kHz: (a) SIMPSON simulated spectrum, (b) experimental spectrum. A 90° pulse width of 2.7 μs with an acquisition time of 4.096 ms and recycle delay of 30 s was used. The decoupling power on ^{1}H channel used was of 57.8 kHz; 1816 number of scans with signal-to-noise ratio of 85.7.

References

1. Frankland, E. *J. Chem. Soc.* **1849**, *2*, 263.
2. (a) Davis, A.G. *Organotin Chemistry*, 2nd Edition; WILEY-VCH Verlag GmbH & Co. KGaA: Weinheim, 2003; 1-27. (b) Lefferts, J. L.; Molloy, K. C., Hossain, M. B.; Helm, D. V. D.; Zuckerman, J. J. *J. Organomet. Chem*. **1982**, *240*, 349.
3. Clark, H.C.; O'Brien, R.J.; Trotter, J. *J. Chem. Soc*. **1964**, 2332.
4. Yasuda, K.; Kawasaki, Y.; Kasai, N.; Tanaka, T. *Bull. Chem. Soc. Jpn.* **1965**, *38*, 1216.
5. Bai, H.; Harris, R.K**.** *J. Magn. Reson*. **1992**, *96*, 24.

6. Bai, H.; Harris, R.K.; Reuter, H. *J. Organomet. Chem*. **1991**, *408*, 167.
7. Holleman, A. F.; Wiberg, N. *Inorganic Chemistry*, Academic Press, San Diego, California, 2001, 526.
8. Smith, W. C *Angew. Chem., Int. Ed.* **1962**, *1*, 467.
9. Hasek, W. R.; Smith, W. C.; Engelhardt, V. A. *J. Am. Chem. Soc.* **1960**, *82*, 543.
10. Silvey, G. A.; Cady, G. H. *J. Am. Chem. Soc.* **1950**, *72*, 3624.
11. Brown, F.; Robinson, P.L. *J. Chem. Soc. (London)* **1955**, 3147.
12. Tullock, C.W.; Fawcett, F.S.; Smith, W.C.; Coffman, D.D. *J. Am. Chem. Soc.* **1960**, *82*, 539.
13. Campbell, R. H.; Gudzinowicz, B. J. *Anal. Chem.* **1961**, *33*, 842.
14. Bartlett, N.; Robinson, P. L. *Chem. Ind. (London)* **1956**, 1351.
15. Azeem, M.; Brownstein, M.; Gillespie, R.J. *Can. J. Chem.* **1969**, *47*, 4159.
16. Smith, W. C. *Angew. Chem., Int. Ed.* **1962**, *1*, 467.
17. Gillespie, R. J.; Hargittai, I. *The VSEPR Model of Molecular Geometry*, Allyn and Bacon, Boston, MA, 1991
18. Muetterties, E. L.; Philips, W. D. *J. Am. Chem. Soc.* **1959**, *81*, 1084.
19. Gibson, J. A.; Ibbott, D. G.; Janzen, A. F. *Can. J. Chem.*, **1973**, *51*, 3203.
20. Janzen, A. F. *Coord. Chem. Rev.* **1994**, *130*, 355.
21. Klemperer, W. G.; Krieger, J. K.; McCreary, M. D.; Muetterties, E. L.; Traficante, D. D.; Whitesides, G. M. *J. Am. Chem. Soc.* **1975**, *97*, 7023.
22. Taha, A. N.; True, N. S.; LeMaster, C. B.; Lemaster, C. L.; Crawford, S. M. N. *J. Phys. Chem. A*, **2000** *104*, 3341.
23. Berry, R. S. *J. Chem. Phys.* **1960**, *32*, 933.

24. Mauksch, M.; Schleyer, P. V. R. *Inorg. Chem.* **2001**, *40*, 1756.

25. Hasek, R.W.; Smith, W.C.; Engelhardt, V.A. *J. Am. Chem. Soc.* **1960**, *82*, 543.

26. Miller, T. M.; Viggiano, A. A.; Dolbier, W. R., Jr.; Sergeeva, T. A.; Friedman, J. F. *J. Phys. Chem. A.* **2007**, *111*, 1024.

27. Tunder, R.; Siegel, B. *J. lnorg. Nucl. Chem* **1963**, *25*, 1097.

28. Waterfeld, A.; Mews, R. *Angew. Chem., Int. Ed.* **1982**, *21*, 354.

29. Tullock, C.W.; Coffman, D.D.; Muetterties, E.L. *J. Am. Chem. Soc.* **1963**, 357.

30. Bittner, J.; Fuchs, J.; Seppelt, K. *Z. Anorg. Allg. Chem.* **1988**, *557*, 182.

31. Christe, K. O.; Curtis, E. C.; Schack, C. J.; Pilipovich, D. *Inorg. Chem.* **1972**, *11*, 1679.

32. Muetterties, E. L. *J. Am. Chem. Soc.* **1960**, *82*, 1082.

33. Padma, D. K. *J. Fluorine Chem.* **1974**, *4*, 441.

34. Mallouk, T. E.; Rosenthal, G. L.; Müller, G.; Brusasco, R.; Bartlett, N. *Inorg. Chem.* **1984**, *23*, 3167.

35. Bai, S.; Wang, W; Dybowski, C. *Anal. Chem.* **2010**, *82*, 4917.

36. Borisov, A.; Hazendonk, P.; Hayes, P. *J. Inorg. Organomet. Polym.* **2010**, *20*, 183.

37. Silvey, G. A.; Cady, G. H. *J. Am. Chem. Soc.* **1950**, *72*, 3624.

38. Rayleigh, D. P.; Levitt, M. H.; Griffin, R. G. *Chem. Phys. Lett.* **1988**, *146*, 71.

39. Harris, R. K.; Jackson, P. *Chem. Rev. (Washington, DC, U.S.)* **1991**, *91*, 1427.

40. Munowitz, M. G.; Griffin, R. G.; Bodenhausen, G.; Huang, T. H. *J. Am. Chem. Soc.* **1981**, *103*, 2529.

41. Chaudhary, P.; Gerken, M; Goettel, J.; Hazendonk, P.; Mercier, H. P. A. *CSC Conference*, Toronto **2010**, INP 116.
42. Watanabe, T.; Hayashi, M.; Hayashi, S.; Fukuyama, H.; Nagata, K. *International Conference on molten Slags Fluxes and Salts* **2004**, 669.
43. Miller J. M. *Prog. Nucl. Magn. Reson.* **1996**, *28*, 255.
44. Groβ, U.; Rudiger, S.; Grimmer, A. R.; Kemnitz, E. *J. Fluorine Chem.* **2002**, *115*, 193.
45. Harris, R. K.; Monti, G. A.; Holstein, P. *Studies in Physical and Theoretical Chemistry*, 1998, *84*, Elsevier, 667.
46. Ellis, D. A.; Martin, J. W.; Muir, D. C. G.; Mabury, S. A. *Anal*., 2003, *128*, 756.
47. Ulrich, A. S. *Prog. Nucl. Magn. Reson.* 2005, *46*, 1.
48. Liu, J; Nagapudi, K; Kiang, Y. H.; Martinez, E.; Jona, J. *Drug Dev. Ind. Pharm*. **2009**, *35*, 969.
49. Offerdahl, T. J.; Salsbury, J. S.; Dong, Z.; Grant, D. J.; Schroeder, S. A.; Prakash, I.; Gorman, E. M.; Barich, D. H.; Munson, E. J. *J. Pham. Sci.* **2005**, *94*, 2591.
50. Levitt, M. H. *Spin Dynamics*, 1st Edition; John Wiley & Sons Ltd.: Oxford, 2001.
51. Lecture notes from Dr. Paul Hazendonk (Department of Chemistry and Biochemistry, University of Lethbridge), *Solid-state NMR Spectroscopy, Chem 5000B,* 2010.
52. Dewar, M. J. *Solid State NMR Spectroscopy*, Blackwell Science, Oxford, 2002.
53. Dyer, J.R. *Applications of Absorption Spectroscopy of Organic Compounds*, Eastern Economy Edition, Prentice Hall of India Private Limited: New Delhi, 2002.

54. Banwell, C. N.; McCASH, E. M. *Fundamentals of Molecular Spectroscopy*, 4th Edition; Tata McGraw-Hill Publishing Company Limited: New Delhi, 1998.

55. Smith, S. A.; Palke, W. E.; Gerig, J. T. *Concepts Magn. Reson.* **1992**, *4*, 107.

56. Smith, S.A.; Palke, W. E.; Gerig, J. T. *Concepts Magn. Reson.* **1992**, *4*, 181.

57. Harris, R. K.; Olivieri, A. C. *Prog. NMR Spectrosc.* **1992**, *24*, 435.

58. Olivieri, A. C. *Solid State Nucl. Magn. Reson.* **1992**, *1*, 345.

59. Harris, R. K. *J. Magn. Reson.* **1988**, *78*, 389.

60. Pines, A.; Gibby, M. G.; Waugh, J. S. *J. Chem. Phys.* **1973**, *59*, 569.

61. Hediger, S.; Meier, B. H.; Kurur, N. D.; Bodenhausen, G.; Ernst, R. R. *Chem. Phys. Lett.* **1994**, *223*, 283.

62. Meier, B. H. *Chem. Phys. Lett.* **1992**, *188*, 201.

63. Raleigh, D.P.; Levitt, M.H.; Griffin, R.G. *Chem. Phys. Lett.* **1988**, *146*, 71.

64. Bak, M.; Rasmussen, J. T.; Neilson, N. C. *J. Magn. Reson.* **2000**, *147*, 296.

65. Smith, S. A.; Palke, W. E.; Gerig, J. T. *Concepts Magn. Reson.* **1992**, *4*, 107.

Chapter-2

Experimental Section

Synthesis of different fluorine containing compounds

2.1 Standard techniques

Most compounds used in the course of this work are moisture and air-sensitive; consequently all manipulations were carried out under rigorously anhydrous inert-atmosphere conditions. Glass and metal vacuum line systems, a dry-nitrogen-filled glove bag, and the oxygen- and moisture-free atmosphere of a Vacuum Atmospheres (Omni Lab) drybox were used.

Volatile materials that were non-corrosive towards glass in the absence of water were manipulated on a Pyrex-glass vacuum line equipped with grease-free 6-mm J. Young glass stopcocks equipped with PTFE barrels (Figure 2.1.1). Pressures inside the manifold were monitored using a Heise gauge (model CC, 0–1000 mmHg, beryllium/copper Bourdon tube, Dresser Instruments). The final vacuum was monitored by a Varian thermocouple gauge connected to the vacuum line between the liquid-nitrogen trap and the vacuum pump.

Volatile materials, which attacked glass, were handled on a metal vacuum line constructed from nickel and 316 stainless steel, and equipped with 316 stainless steel valves and fittings (Autoclave Engineers Inc.), PTFE, and FEP (Figure 2.1.2). Pressures were measured at ambient temperature using Baratron capacitance manometers (MKS, Type 626A, effective range 0 – 1000 mmHg) having inert wetted surfaces constructed of Inconel, in conjunction with a digital readout.

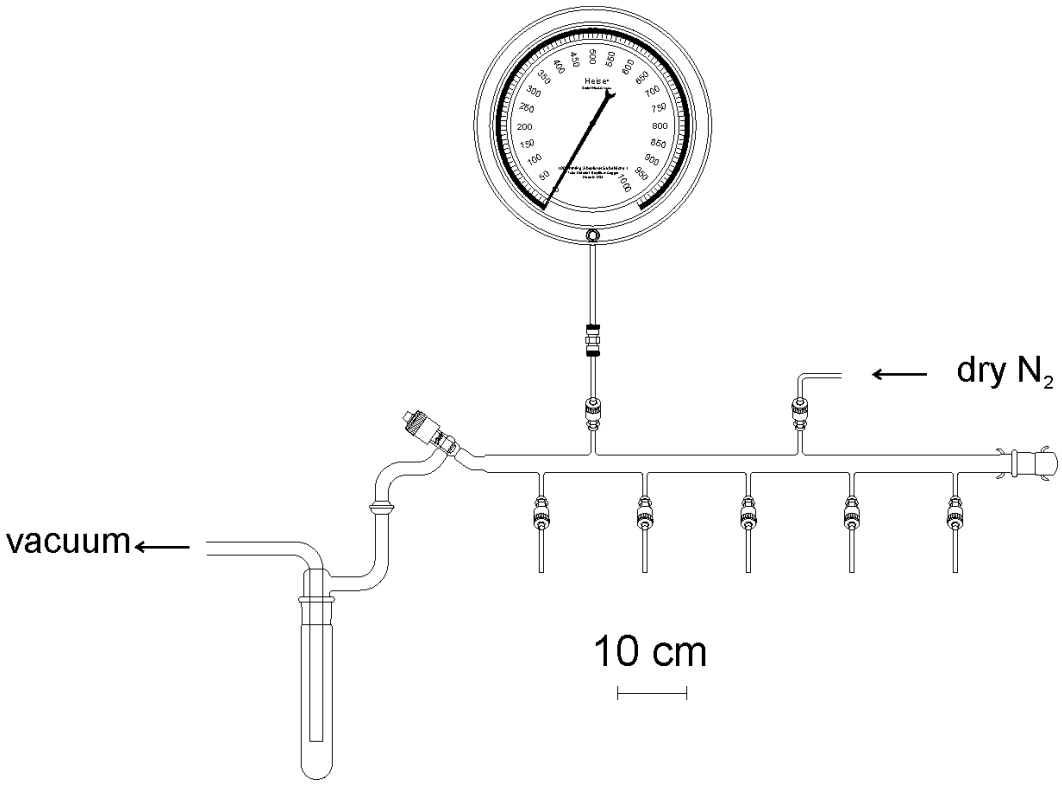

Figure 2.1.1 Glass vacuum line system equipped with J. Young PTFE/glass stopcocks and a Heise gauge (M.Sc. thesis from Jared Nieboer).

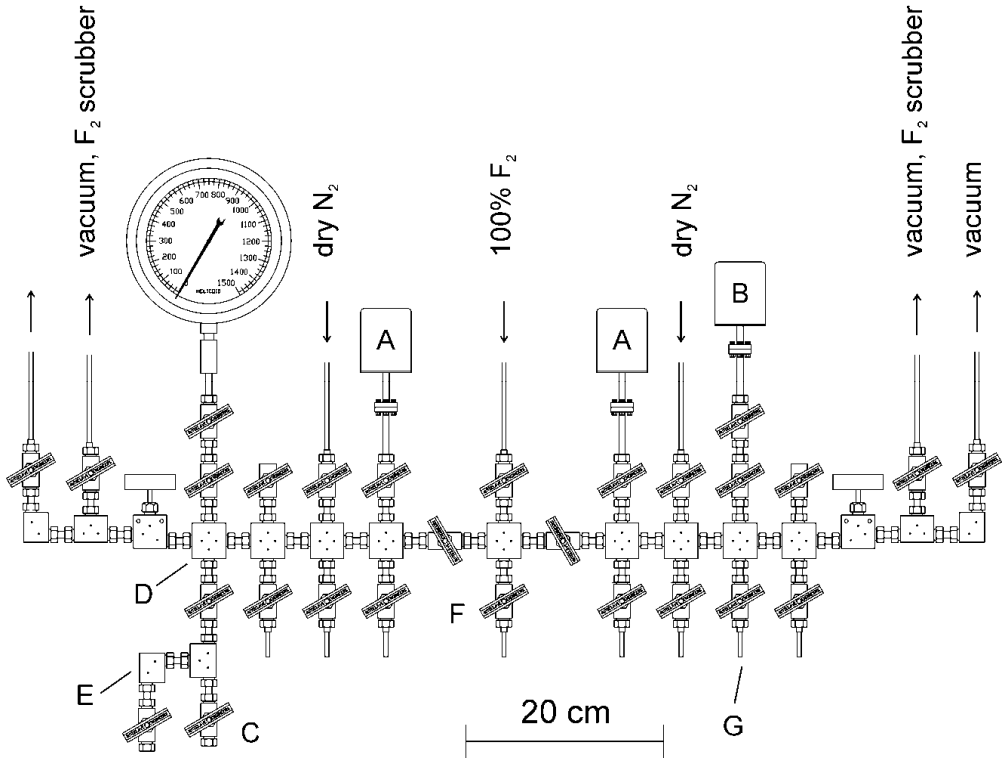

Figure 2.1.2 Metal vacuum system; (A) MKS type 626A capacitance manometer (0-1000 Torr), (B) MKS Model PDR-5B pressure transducers (0-10 Torr), (C) 3/8-in. stainless-steel high-pressure valves (Autoclave Engineers, 30VM6071), (D) 316 stainless-steel cross (Autoclave Engineers, CX6666), (E) 316 stainless-steel L-piece (Autoclave Engineers, CL6600), (F) 316 stainless steel T-piece (Autoclave engineers, CT6660), (G) $^{3}/_{8}$-in o.d., $^{1}/_{8}$-in. i.d. nickel connectors, (H) $^{1}/_{8}$-in o.d., $^{1}/_{8}$-in. i.d. nickel tube. (M.Sc. thesis from Jared Nieboer).

Vacuum on the glass (ca. 10^{-5} Torr) and metal lines (ca. 10^{-4} Torr) was attained by the use of Edwards two-stage direct-drive RV8 Edward vacuum pumps. Two vacuum pumps were used on a metal vacuum line, one for the rough vacuum and the other for the fine vacuum. The rough pump was connected to a fluoride/fluorine trap consisting of a stainless-steel cylinder (75 cm length, 17 cm outer diameter) packed with soda lime absorbent (EMD, 4-mesh). Removal and disposal of volatile reactive fluorinated compounds was accomplished by pumping through and entrapment on a bed of soda lime followed by trapping of the volatile reaction products, CO_2 and H_2O, in a glass liquid-nitrogen trap. The second vacuum pump provided the high vacuum source for the manifold and was cold trapped with a glass liquid-nitrogen trap.

All the preparative work involving SF_4, AsF_5, SbF_5, and anhydrous HF was carried out in ¼-in or 4-mm outer diameter FEP tubes which were heat-sealed at one end and connected through 45° flares to Kel-F or 37° flares to stainless steel valves. The FEP sample tubes were dried under dynamic vacuum overnight on a glass vacuum line prior to transfer on the metal line where they were checked for leaks, passivated with fluorine at 1 atm for 12 hours, re-evacuated and then back filled with dry N_2 before transferring to the dry box. Pyrex-glass reaction vessels were dried under dynamic vacuum overnight periodically flamed out by use of a Bunsen burner.

Nuclear magnetic resonance (NMR) spectra were recorded on samples prepared in 4-mm o.d. FEP tubes. The NMR tubing had one end heat sealed by pushing the end of the FEP tube into the hot end of a thin-walled 5-mm o.d. NMR tube and the other end was fused to a ¼-in. o.d. thick-walled FEP tubing which was heat-flared for direct attachment to a Kel-F valve (Figure 2.1.3(a)). The 4-mm sample tubes used for NMR

spectroscopy were heat sealed under dynamic vacuum with a heat gun while the sample was frozen at –196 °C. All heat-sealed samples were stored submerged in liquid nitrogen (–196 °C) until they could be spectroscopically characterized. For NMR measurements, the 4-mm FEP tubes were inserted into standard 5-mm precision NMR tubes before insertion into the NMR probe.

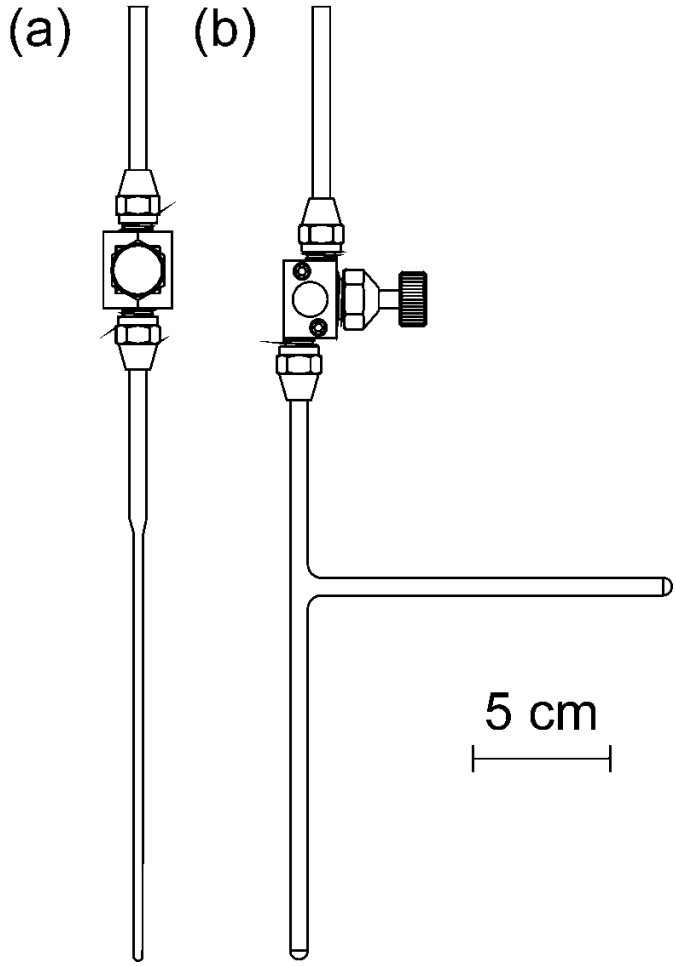

Figure 2.1.3 Common FEP reactors used to conduct experiments: (a) 4-mm o.d. reaction vessel equipped with a Kel-F valve. (b) ¼-in. o.d. FEP T-reactor equipped with Kel-F valve (M.Sc. thesis from Jared Nieboer).

Raman spectra of solids that are stable at room temperature and which do not attack glass were recorded on samples in Pyrex-glass melting point capillaries. Before use, the melting point capillaries were heated under dynamic vacuum for 24 h at 200 °C and then stored in the drybox where they were loaded with the appropriate materials. The end of the loaded melting point capillary was temporarily sealed with Kel-F grease before removal from the drybox. The capillaries were then immediately heat-sealed with an oxygen-natural gas torch.

Vessels were attached to vacuum lines through thick-walled FEP tubing and ¼-in. PTFE Swagelok connectors or ¼-in. stainless-steel Ultra-Torr connectors fitted with viton rubber O-rings.

2.2 Preparation of inserts for solid-state NMR spectroscopy

Solid-state NMR spectra of $[SF_3][SbF_6]$ and $[SF_3][AsF_6]$ were recorded with the use of an FEP insert, which was prepared by using a 3.2-mm o.d. FEP tube through heat-sealing it at one end and then loading the required material in it inside the glove box. The filled inserts were plugged using a FEP plug and the plug was fused to the insert-walls outside of the dry box, permanently sealing the insert. This FEP insert was inserted in the 4-mm zirconia rotor before recording spectra at low temperature.

2.3 Purification of HF, C_5H_5N, SbF_5, 4-picoline, triethylamine

Anhydrous hydrogen fluoride (Air Products) was stored at room temperature in a nickel storage vessel equipped with a monel (Autoclave Engineers) valve. Hydrogen fluoride was dried over potassium hexafluoronickelate(VI) in a ¾-in o.d. FEP vessel

(Figure 2.3.1), equipped with a stainless steel valve, prior to transfer to reaction vessels by vacuum distillation on the metal vacuum line through connections constructed of FEP.

Pyridine (Sigma-Aldrich, 99.8%) was added to CaH_2 in a glass storage bulb equipped with a Teflon J. Young stopcock inside a glove bag. Then, the liquid was vacuum distilled from the original storage bulb onto fresh CaH_2 in a glass bulb equipped with a Teflon J. Young stopcock.

Antimony pentafluoride, SbF_5 (Ozark-Mahoning Co.) was purified by vacuum distillation in a Teflon and glass apparatus connected with PTFE Swagelok unions and stored in a glass U-tube equipped with PTFE J. Young stopcocks, which was kept in a dessicator. Subsequent transfers of SbF_5 were performed through a glass Y-piece with PTFE Swagelok connections.

Triethylamine and 4-picoline were added to molecular sieves (4Å) in glass bulbs inside the glove bag, followed by vacuum distillation onto fresh molecular sieves in glass storage bulbs equipped with a Teflon J. Young stopcock.

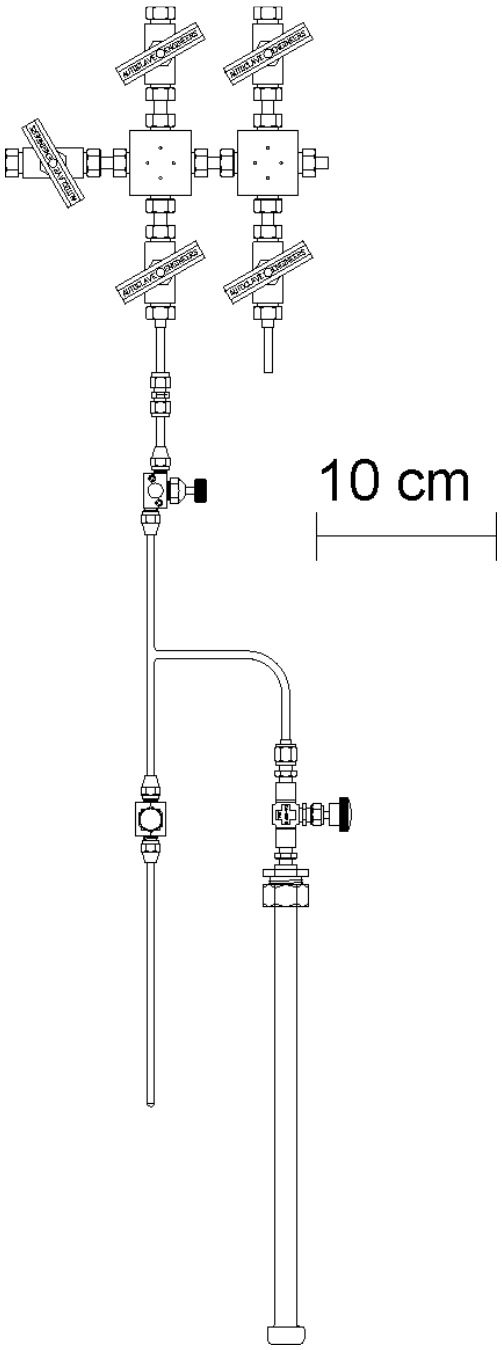

Figure 2.3.1 A ¾-in. o.d. FEP vessel equipped with a stainless steel valve and a FEP T-piece connection for distillation of HF to reactors (M.Sc. thesis from Jared Nieboer).

2.4 SF_4 Adducts: Synthesis and Characterization

2.4.1 Reaction between SF_4 and pyridine

On the glass vacuum line, 0.056 g (7.1×10^{-4} mol) of pyridine was transferred to a 4-mm o.d. FEP reactor equipped with a Kel-F valve. The reactor was connected to the metal vacuum line and approximately 1.16×10^{-3} mol SF_4 was vacuum distilled into the FEP reactor. The reactor was slowly warmed up to –78°C and properly agitated for the completion of reaction. Excess SF_4 was removed under dynamic vacuum by warming up the reactor to –60°C. Low-temperature Raman and solution-state ^{19}F, ^{1}H and ^{13}C NMR spectra were recorded. The reactor was warmed up to –38°C where pyridine was recovered under dynamic vacuum.

2.4.2 Reaction between SF_4 and lutidine

Inside the glove bag, 0.094 g (8.8×10^{-4} mol) of lutidine was transferred to a 4-mm o.d. vacuum dried FEP reactor. The lutidine was used without purification. Approximately 6.51×10^{-3} mol SF_4 was vacuum distilled into the reactor. The reactor was slowly warmed up to –78°C and properly agitated for the completion of reaction. The excess SF_4 was removed at –60°C. The low-temperature Raman spectra were recorded and compared with that of the reactants. The reactor was warmed up to –38°C where lutidine was recovered after pumping off all volatiles. The recovered lutidine contained traces of HF_2^-.

2.4.3 Reaction between SF_4 and 4-picoline:

On the glass vacuum line, 0.094 g (1.0×10^{-3} mol) of 4-picoline was transferred to a 4-mm o.d. vacuum dried FEP reactor. Approximately 6.51×10^{-3} mol SF_4 was vacuum distilled onto the 4-picoline. The reactor was slowly warmed up to –78°C and properly agitated for the completion of reaction. The excess SF_4 was removed at –60°C. The low-temperature Raman spectrum was recorded and compared with the reactants. The reactor was warmed up to –35°C where the 4-picoline was recovered after pumping off volatiles. The recovered 4-picoline contained traces of HF_2^-.

2.4.4 Reaction between SF_4 and triethylamine:

On the glass vacuum line, 0.074 g (7.3×10^{-4} mol) of triethylamine was transferred to a 4-mm o.d. vacuum dried FEP reactor. Approximately 1.592×10^{-3} mol SF_4 was vacuum distilled onto the triethylamine. The reactor was slowly warmed up to –78°C and properly agitated for the completion of reaction. The excess SF_4 was removed at –60°C. The low-temperature Raman spectrum was recorded at -110°C. The reactor was warmed up to –35°C where the triethylamine was recovered after removal of volatiles under dynamic vacuum. The recovered triethylamine contained traces of HF_2^-.

2.4.5 Reaction between SF_4 and 4,4'-bipyridine:

On the glass vacuum line 0.025 g (1.6×10^{-4}mol) of 4,4'-bipyridine was transferred to a 4-mm o.d. vacuum dried FEP reactor. Approximately 1.16×10^{-3} mol SF_4 was vacuum distilled onto the 4,4'-bipyridine. The reactor was slowly warmed up to –78°C and properly agitated for the completion of reaction. The excess SF_4 was removed

at –60°C. Low-temperature Raman and solution state ^{19}F, ^{1}H and ^{13}C NMR spectra were recorded. The reactor was warmed up to room temperature where a solid adduct was obtained which was stable under dynamic vacuum and indicated a mass ratio of 1.00**:**0.89. The exact nature of the product, however, could not be determined so far.

2.4.6 Reaction between SF_4 and quinoline, isoquinoline and 2,2'-bipyridine:

The above mentioned procedure was attempted for the reaction between SF_4 and quinoline, isoquinoline and 2,2'-bipyridine but low-temperature Raman spectroscopy indicated no product formation.

2.5 Preparation of Me_3SnF

Trimethyltin fluoride was prepared by metathesis reaction of trimethyltin chloride with potassium fluoride according to the literature.[2] Trimethyltin chloride (Alfa Aesar) and potassium fluoride (99%) (Fischer Scientific Company) were used without further purification to carry out the metathesis reaction in tetrahydrofuran (THF) under vacuum (Eq. 1). For this purpose THF was dried over sodium before use.

$$Me_3SnCl + KF \xrightarrow{THF} Me_3SnF + KCl \qquad \text{(Eq. 1)}$$

Solid Me_3SnF was isolated by filtration and stored inside the drybox.

2.6 Synthesis of the SF_3^+ salts

The $[SF_3][SbF_6]$ and $[SF_3][AsF_6]$ salts were prepared according to literature reports.[3,4,5]

2.6.1 Preparation of $[SF_3][SbF_6]$

On the glass vacuum line, 0.116 g (5.35×10^{-4} mol) of SbF_5 was transferred to a 4-mm o.d. vacuum-dried FEP reactor. Approximately 2.81×10^{-3} mol SF_4 was vacuum distilled into the reactor. The reactor was slowly warmed up to –78°C and properly agitated for the completion of reaction. The excess SF_4 was removed by warming the reactor up to ambient temperature where a white salt was obtained which was stable under dynamic vacuum.

2.6.2 Preparation of $[SF_3][AsF_6]$

On the steel vacuum line, approximately 3.0×10^{-3} mol of SF_4 was vacuum distilled into a 4-mm o.d. FEP reactor. Approximately 1.5×10^{-3} mol AsF_5 was vacuum distilled into the reactor. The reactor was slowly warmed up to –78°C and properly agitated for the completion of reaction. The excess SF_4 was removed by warming the reactor up to ambient temperature where a white solid salt was obtained which was stable under dynamic vacuum. The low-temperature Raman spectrum was recorded.

2.7 Raman Spectroscopy:

All Raman spectra were recorded on a Bruker RFS 100 FT Raman spectrometer equipped with a quartz beam splitter, a liquid-nitrogen cooled Ge detector, and low-

temperature accessory. The backscattered (180°) radiation was sampled. The useable Stokes range was 50-3500 cm^{-1} with a spectral resolution of 2 cm^{-1}. A Nd:Yag laser with a 1064-nm line was used for excitation of the sample. Spectra were recorded on solution samples in either 4-mm or ¼-in. FEP reactors using Laser powers of 150–200 mW. All the spectra were collected between the temperature range +35°C to –110°C.

2.8 Single Crystal X-ray Diffraction

2.8.1 Crystal Growth of $[SF_3](HF)[SbF_6]$

Approximately 0.018 g of $[SF_3][SbF_6]$ was loaded in a ¼" FEP T-reactor inside the dry box followed by distillation of ca. 1.28 mL anhydrous HF. Upon warming to room temperature, the solid dissolved completely. This reactor was placed in a cryo-bath at –70°C. Anhydrous HF was slowly pumped off to –60°C leaving behind pale yellow crystals.

2.8.2 Low-Temperature Crystal Mounting

A low-temperature crystal mounting technique was utilized for the thermally unstable and moisture-sensitive crystals of $[SF_3](HF)[SbF_6]$. The FEP reactor containing crystals was cut open below the Kel-F valve under a flow of dry nitrogen while the lower part of the FEP reactor, which contained the crystals, was immersed in dry ice at –78°C. The crystals were then quickly transferred from the chilled tube into an aluminum trough that was cooled by a flow of dry-nitrogen, which was passed through a 5-L Dewar of liquid nitrogen (Figure 2.8.1). The temperature of the trough had been adjusted to approximately –85°C and had been measured with a copper-constantan thermocouple

inserted midway into the stream ca. 2-mm above the trough. A crystal was selected under a microscope and mounted on a glass fibre using an inert perfluorinated polyether, Fomblin Z-25 (Ausimont Inc.) while being kept in the cold nitrogen stream. The polyether selected for crystal mounting was sufficiently viscous to adhere to the crystal, engulf it, and freeze quickly thereafter. The glass fibre had previously been attached using an epoxy to a metallic pin that was, in turn, mounted on a magnetic base, which was attached to a magnetic wand, while picking the crystal. The pin with the crystal was quickly (<30 s) transferred from the wand to the goniometer head of the X-ray instrument using cryotongs, which had been chilled with liquid nitrogen prior to use, and attached to the magnetic base on the goniometer head.

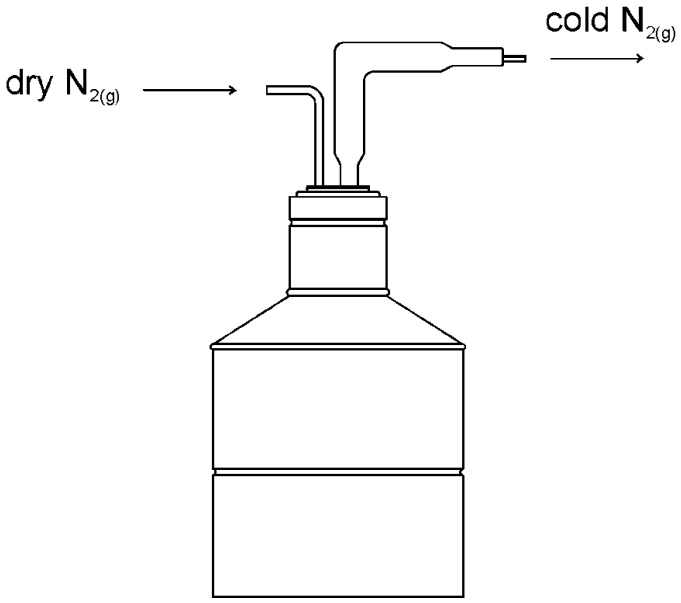

Figure 2.8.1 Crystal mounting apparatus consisting of a five-liter liquid nitrogen Dewar equipped with a rubber stopper, a glass dry nitrogen inlet and a silvered-glass cold nitrogen outlet with aluminium cold trough. (M.Sc. thesis from Jared Nieboer).

2.8.3 Collection and Reduction of X-ray data

X-ray data was collected at −120 °C on a Bruker SMART APEX-II X-ray diffractometer, which was equipped with an Apex II 4K charge-coupled device (CCD) area detector, a Kryo-Flex low-temperature device, and a Mo Kα radiation (λ = 0.71073 Å) source with a graphite monochrometer. The crystal-to-detector distance was 6.120 cm. A hemisphere of data was collected with 30 s exposure time. Cell reduction was carried out using the Program *SAINT*[8] which applied Lorentz and polarization corrections to three-dimensionally integrated diffraction spots.

2.8.4 Solution and Refinement of Structures

Calculations were performed using the *SHELXTL-plus v.6.14* package[9] for structure determination, refinement and molecular graphics. The *Xprep* program was used to confirm the unit cell dimensions and the crystal lattice. The crystal structure was solved using direct method. Successive difference Fourier syntheses revealed all lighter atoms. The structures were minimized by least squares refinement based on the square of the structure factors, F^2 (equivalent to intensity). Atom positions were refined anisotropically and the extinction coefficient was calculated for the crystal structure. Both residual values, R_1 based on F and the weighted residual values wR_2 based on F^2, are available in the structure refinement tables along with the goodness of fit *GooF*. They represent the following equations:

$$R_1 = \frac{\sum || Fo | - | Fc ||}{\sum | Fo |}$$ The conventional R-factor based upon the structure factor.

$$wR_2 = \sqrt{\frac{\sum[w(Fo^2 - Fc^2)^2]}{\sum[w(Fo^2)^2]}}$$ The weighted R-factor based on the square of the structure factors (observed and calculated, F^2 (based upon intensity).

$$GooF = \sqrt{\frac{\sum[w(Fo^2 - Fc^2)]}{(n-p)}}$$ The *GooF* is based upon intensity where *n* is the number of reflections, *p* is the number of parameters refined.

2.9 NMR Spectroscopy

2.9.1 Solution-State NMR Spectroscopy

All the solution-state NMR spectra were recorded on a 300 MHz Bruker Avance II NMR spectrometer. All the samples were contained in 4-mm FEP inliners and the NMR spectra were collected unlocked and were referenced externally. Fluorine-19 NMR spectra were referenced externally relative to neat $CFCl_3$ ($\delta(^{19}F) = 0$ ppm), while ^1H and ^{13}C NMR spectra were referenced relative to neat TMS ($\delta(^{13}C) = 0$ ppm; $\delta(^1H) = 0$ ppm) at room temperature. The resonance frequencies for ^1H, ^{19}F and ^{13}C were 300.13, 282.40 and 100.61 MHz, respectively, on the 300 MHz Bruker Avance II NMR spectrometer.

2.9.2 Solid-state NMR

All the solid-state NMR spectra were recorded on a 500 MHz Varian-Inova NMR spectrometer. All of the synthesized SF_3^+ salt samples were contained in 3.2-mm o.d. FEP inserts and all NMR spectra were collected unlocked at low temperature and were referenced externally. Fluorine-19 NMR spectra were referenced externally relative to neat hexafluorobenzene ($\delta(^{19}F) = -166.4$ ppm), while ^1H and ^{13}C NMR spectra were

referenced relative to adamantane, ($\delta(^{13}C)$ = –38.5 ppm; $\delta(^{1}H)$ = 1.63 ppm) at room temperature. Trimethyltin fluoride was packed in the rotors directly without the use of FEP inserts.

References:

1. Muetterties, E. L. *J. Am. Chem. Soc.* **1960**, *82*, 1082.
2. Krause, E. *Ber. Dtsch. Chem. Ges.* **1918**, *51*, 1447.
3. Azeem, M.; Brownstein, M.; Gillespie, R.J. *Can. J. Chem.* **1969**, *47*, 4159.
4. Gillespie, R.J.; Moss, K.C. *J. Chem. Soc.* **1966**, 1170.
5. Bacon, J.; Dean, P.A.W.; Gillespie, R.J. *Can. J. Chem.* **1969**, *47*, 1655.
6. Bartlett, N.; Robinson, P. L. *J. Chem. Soc.* **1961**, 3417.
7. Gibler, D.D.; Adams, C. J.; Fischer, M.; Zalkin, A.; Bartlett, N. *Inorg. Chem.* **1972**, *11*, 2325.
8. Bruker; Apex2 and Saint-plus. Bruker AXS Inc.: Madison, Wisconsin, USA, 2006.
9. Sheldrick, G. M.; 6.14 ed.; Bruker AXS INC.: Madison, Wisconsin, USA., 2003.

Chapter-3

3. Solid-State NMR Spectroscopy of Trimethyltin Fluoride

3.1 Introduction

Trimethyltin fluoride, Me_3SnF, is one of the examples of triorganotin fluorides and is of current interest owing to its use as a common fluorinating agent in organofluorine chemistry.[1] It is pentacoordinate about tin in the solid-state[2] while being monomeric in solution.[3] Trimethyltin fluoride can be characterized by different techniques, such as IR-spectroscopy, Raman spectroscopy, solution NMR spectroscopy, and solid-state NMR spectroscopy.

Trimethyltin fluoride differs in many properties from its halide analogs. It has a very high melting point (>360°C), which is indicative of its polymeric structure[4] while the other halides (-Cl, -Br and –I) have relatively low melting points (around 35°C).[5] Trimethyltin fluoride is only soluble in solvents such as hot ethanol while the other halide analogs are readily soluble in organic solvents.[5] Trimethyltin fluoride gives needle-shaped crystals from hot ethanol in which trimethyltin groups and fluorine atoms arrange alternately along the needle axis (a-axis in Figure 3.1) as suggested by the X-ray diffraction work by Clark *et al*.[4] The structure of trimethyltin fluoride, however, cannot be easily refined, since the structure exhibits severe disorder. Possible disordered models of this chain polymer were suggested in which the structure can be interpreted either in terms of planar [4,7] trimethyltin groups.[4] In one proposed structure, the trimethyltin group is non-planar with a Sn-F covalent bond distance of 2.1 Å and a Sn$\cdots$F distance between 2.2 to 2.6 Å.[4] The other model proposed trimethyltin groups being planar and tilted alternately with respect to the axis of the needle crystals (a-axis in Figure 3.1). In both

cases, Sn was assumed to be pentacoordinate and the Sn—F—Sn bridges to be bent. The infrared spectrum of Me_3SnF reported by Okawara *et al.* [8] gave only one strong absorption in the Sn-C stretching region at 555 cm^{-1}. This indicated a planar arrangement of the SnC_3 moiety, because a pyramidal arrangement about Sn would render the symmetric and asymmetric SnC_3 stretching vibrations infrared active.[8] Based on these results a planar SnC_3 moiety was suggested for Me_3SnF, in which the tin atom is five coordinate with three methyl groups and two fluorine atoms. The ligands around tin represents a trigonal bipyramidal configuration. The model of the crystal structure exploited by Yasuda *et al.*[7] considers that planes of the planar trimethyl groups are parallel to one another while the fluorine atoms tilt alternately by giving a Sn—F·····Sn bond angle of 141°, a short Sn—F distance of 2.15 Å and a calculated long Sn····F distance of 2.45 Å.[7] In addition, the F—Sn·····F angle in the disorder model was 141º, instead of the previously assumed 180º.

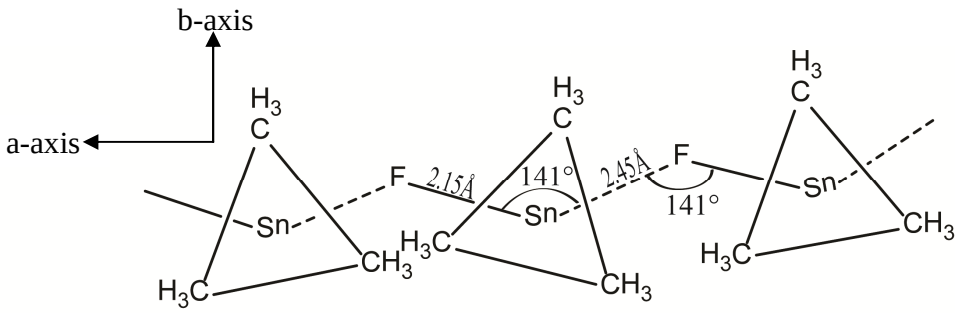

Figure 3.1: Structure of penta-coordinate Me_3SnF in solid-state

Polymeric organotin fluorides such as trimethyltin fluoride, triphenyltin fluoride, tributyltin fluoride, and tri(iso-butyl)tin fluoride can be characterized by solid-state NMR spectroscopy in powder form to determine its coordination number and obtain distance

information.[9,10,11,12] In the solid-state, distances between the tin and fluorine can be obtained with the help of dipolar-coupling information between ^{119}Sn and ^{19}F.

Harris et al. studied Me_3SnF by solid-state NMR spectroscopy. In their analysis of the NMR spectra of Me_3SnF, Harris *et al.*[2] utilized analytical expressions of the AX spin system theory and it was assumed that the $\hat{\hat{\boldsymbol{\sigma}}}$ and $\hat{\hat{\mathbf{J}}}$ tensors are axially symmetric and both co-axial with $\hat{\hat{\mathbf{D}}}$, whose orientation is determined by r_{AX}, the internuclear vector, as shown in Scheme-II.[2]

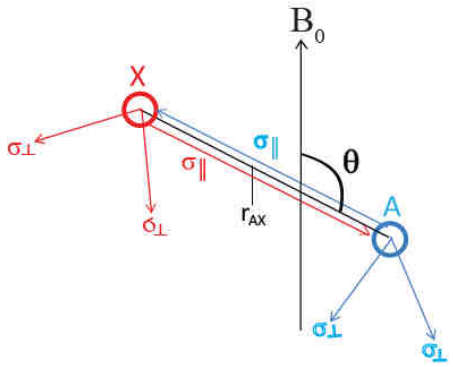

(Scheme-I)

The spin Hamiltonian of an AX spin system was given by Harris *et al.* as shown in Eq. 3.1[2]

$$\hbar^{-1}\hat{\mathbf{H}} = -\omega_A^0\left[1-\left\{\sigma_A^{iso}+\frac{1}{2}\delta_A^{aniso}(3\cos^2\theta-1)\right\}\right]\hat{\mathbf{I}}_{\mathbf{ZA}} - \omega_X^0\left[1-\left\{\sigma_X^{iso}+\frac{1}{2}\delta_X^{aniso}(3\cos^2\theta-1)\right\}\right]\hat{\mathbf{I}}_{\mathbf{ZX}} + \mathbf{J}_{AX}^{iso}\hat{\mathbf{I}}_{\mathbf{ZA}}\hat{\mathbf{I}}_{\mathbf{ZX}} - D'(3\cos^2\theta-1)\hat{\mathbf{I}}_{\mathbf{ZA}}\hat{\mathbf{I}}_{\mathbf{ZX}} \quad (3.1)$$

Where $\omega_A^0 = \gamma_A B_0$ and $\omega_X^0 = \gamma_X B_0$ are the Larmor frequencies of A and X in the absence of shielding, and σ_A^{iso} and σ_X^{iso} are the isotropic A and X shielding constants. The

chemical shift anisotropies $\delta_A^{aniso}$and δ_X^{aniso} were defined as $\sigma_A^{\parallel} - \sigma_A^{iso}$ and $\sigma_X^{\parallel} - \sigma_X^{iso}$, respectively. The angle between the internuclear distance vector and the applied magnetic field (B_0) can be defined as θ. The effective dipolar coupling D' is given in Eq. 3.2

$$D' = D - \frac{\Delta J}{3} \tag{3.2}$$

where ΔJ is the anisotropy of the $\hat{\hat{\mathbf{J}}}$ tensor, which can be shown to be $\Delta J = J_{\parallel} - J_{\perp}$. The symbol D is the dipolar coupling constant between nucleus A and nucleus X given in Eq. 3.3.

$$D = \frac{\mu_o}{4\pi} \frac{\gamma_A \gamma_X}{r_{AX}^3} \tag{3.3}$$

where r_{AX} is the internuclear distance between A and X nucleus. The shielding is axially symmetric and are defined by two unique $\sigma_{\parallel}$ and $\sigma_{\perp}$components as shown in Scheme-II for A or X nucleus. The *J*-tensors can be defined in a similar manner.

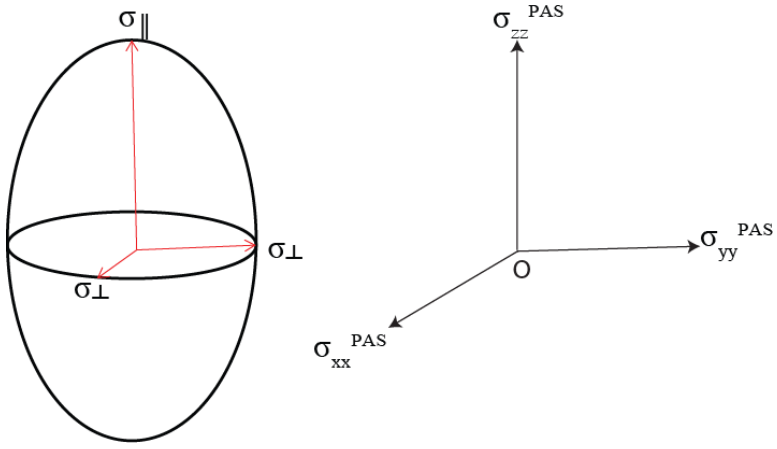

(Scheme-II)

Note that for this treatment only the secular term of heteronuclear coupling interactions are considered and the homonuclear interactions are ignored.[2] This is a reasonable assumption for fast MAS. The transition frequencies of nucleus A can be simplified to the form in Eq. 3.4, where m_X is the spin quantum number of the X nucleus.

$$\omega_A = \omega_A^0 - \left[1 - \left\{\sigma_A^{iso} + \frac{1}{2}\delta_{\mathrm{A}}^{\mathrm{aniso}}(3\cos^2\theta - 1)\right\}\right] - \mathrm{J_{AX}}m_X + D'(3\cos^2\theta - 1)m_X \quad (3.4)$$

This can be reduced further to Eq. 3.5 [2]

$$\omega_A = \omega_A^{iso} - \frac{1}{2}\omega_A^0\delta_{\mathrm{A}}^{\mathrm{eff}}(3\cos^2\theta - 1) - \mathrm{J_{AX}}m_X \quad (3.5)$$

where $\delta_{\mathrm{A}}^{\mathrm{eff}}$ is the effective shielding tensor given by Eq. 3.6.[2]

$$\delta_{\mathrm{A}}^{\mathrm{eff}} = \delta_{\mathrm{A}}^{\mathrm{aniso}} - \frac{2\mathrm{D}'}{\omega_{\mathrm{A}}^0}\mathrm{m_X} \quad (3.6)$$

The sideband manifolds for each m_x is separately analyzed to give $\delta_{\mathrm{A}}^{\mathrm{aniso}}$ and D', which is dependant on r_{AX} and ΔJ as shown in Eq 3.7.

$$\mathrm{D}' = \mathrm{D} - \frac{\Delta \mathrm{J}}{3} = \frac{\mu_{\mathrm{o}}}{4\pi}\frac{\gamma_{\mathrm{A}}\gamma_{\mathrm{X}}}{\mathrm{r}_{\mathrm{AX}}^3} - \frac{\Delta \mathrm{J}}{3} \quad (3.7)$$

The theory of an AX spin system can be extended to the AX_2 spin system by assuming that $\hat{\hat{\boldsymbol{\sigma}}}$ and the $\hat{\hat{\mathbf{J}}}$ are tensors of the X nuclei and are equivalent and coaxial with the X—A· · · · X bond axis, which would have to be linear as shown in Scheme-III.

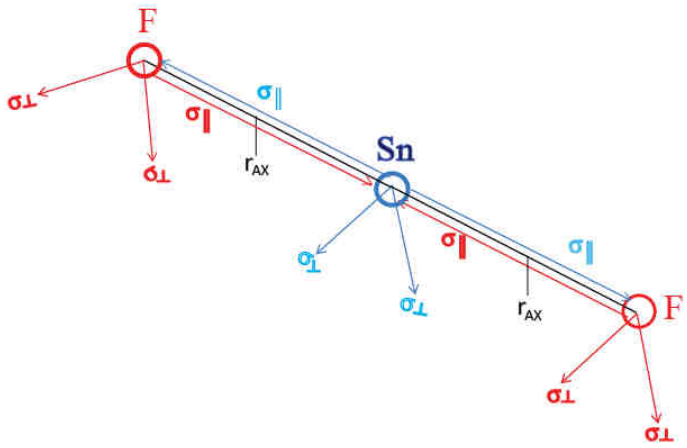

(Scheme-III)

These assumptions are only suited to structures that have the symmetry to allow $\vec{\mathbf{J}}$ and $\vec{\boldsymbol{\sigma}}$ to be axial as well as coaxial with r_{AX}. If these conditions are met, the analytical expression for AX spin-system can be adapted to the AX_2 case.[2] However, for systems where the two X-nuclei are magnetically inequivalent, as for a bent configuration, such analytical expressions would not be valid. In such a case the NMR spectra could only be handled with numerical simulations using software such as SIMPSON.[13] In this manner, true values for the spectral parameters such as shielding, scalar coupling, and dipolar coupling tensors can be obtained. Software of this kind was not available prior to 2000.

The solid-state NMR study by R. K. Harris and Haiping Bai for a variety of polymeric triorganotin fluorides determined spectral parameters by assuming these systems as AX_2 spin systems with a linear AX_2 moiety.[2,14] Spectral parameters obtained by Harris *et al.* are given in Table 3.1. They found that polymeric trialkyl and triaryl fluorides have very large ^{119}Sn chemical shift anisotropies, which would be indicative of low symmetry around tin. In their analysis, they determined the values for chemical shielding anisotropy and D'. The latter in turn is related to D and ΔJ [15,16,17] for each m_x

value. In the Figure 3.2 a linear relationship between the *J*-anisotropies and the internuclear distances of Sn—F is shown, where the ΔJ values can be inferred from the r_{AX} values obtained by X-ray crystallography.

Table 3.1 ^{119}Sn NMR data for different solid triorganotin fluorides

Compound	δ_{iso} (^{119}Sn) (ppm)	$^{1}J(^{119}Sn\text{-}^{19}F)$ (Hz)	δ_{aniso} (ppm)	η	Structure type
Me_3SnF	+24.3	1300	–221	0.00[a]	Polymeric
Bu_3SnF	–9.3	1291	–207	0.42[b]	Polymeric
$(iso\text{-}Bu)_3SnF$	–13.1	1260	–208	0.00[a]	Polymeric
Ph_3SnF	–211.9	1530	–255	0.00[a]	Polymeric
Mes_3SnF	–82.2	2300	42	0.10[c]	Monomeric

[a]axial symmetry between the chemical shift tensors was assumed, hence η = 0.00 (reference 14), [b]experimentally determined asymmetry (reference 9), [c]experimentally determined asymmetry (reference 14)

Harris *et al.*[2,14] obtained a sideband manifold of triplets (δ_{iso}= 24.3 ppm) in the ^{119}Sn{^{1}H} MAS NMR spectrum of Me_3SnF with $^{1}J(^{119}Sn\text{-}^{19}F)$ of 1300 Hz. To apply the analytical expression for the ^{119}Sn NMR frequencies, they assumed the magnetic equivalence of the two fluorine nuclei and an asymmetry parameter of 0.00 for the Sn shielding tensor. Based on this analysis they determined that the chemical shift anisotropy is 221 ppm.[14] From the effective dipolar coupling they were able to estimate ΔJ = –800 Hz and +3500 Hz for the fluorine distances of 2.15Å and 2.45Å, respectively, taken from the X-ray study by Yasuda *et al.*[7] The former Sn—F distance was more

accurately determined than the latter and thus, the same will be true for the corresponding ΔJ's derived from this analysis.[2]

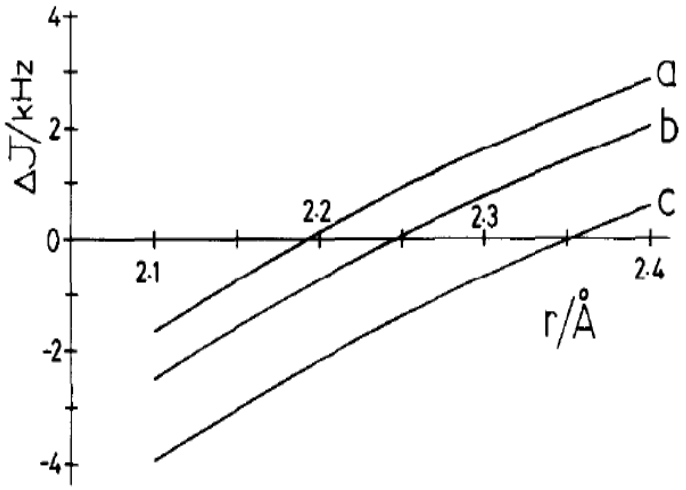

Figure 3.2 Relationship between the Sn-F internuclear distance (r) and the anisotropy in *J*-coupling, Δ*J* (^{119}Sn-^{19}F) for (a) Me_3SnF, (b) $(i\text{-}Bu)_3SnF$ and (c) Ph_3SnF. Reprinted from the Journal of Magnetic Resonance, 96, Bai, H. and Harris, R.K., "The Effects of Interplay of Shielding, Dipolar Coupling, and Indirect Coupling Tensors in the Tin-119 NMR Spectra of Solid Triorganyl Tin Fluorides", 24-30, copyright (1992), with permission from Elsevier.

In the first ^{1}H NMR study on solid trimethyltin fluoride, the molecular motions in trimethyltin fluoride were studied by S. E. Ulrich, measuring the second moments of the CH_3 signal as a function of temperature on a static sample.[18] Second moments are related to the homonuclear dipolar coupling between two protons, which can be used to calculate the internuclear distance between two protons. He concluded that the closest distance between protons in the adjacent methyl groups in the same polymer chain is 1.77 Å, which is less than the sum of the van der Waal radii[19] of two hydrogen atoms (2.4 Å).[18]

The structural analysis of methyltin polymers using ^{13}C solid-state NMR spectroscopy by Lockhart and Manders provided an empirical relationship between ^{1}J (^{119}Sn-^{13}C) and Me—Sn—Me bond angle (θ) for a variety of organotin polymers, which can be given as Eq. 3.8.[20,21,22]

$$|^{1}J| = (10.7 \pm 0.5)(\theta) - (778 \pm 64) \quad (3.8)$$

They determined the ^{1}J (^{119}Sn-^{13}C) for Me_3SnF to be 550 Hz, which correlates to a calculated angle of 124.10 ± 0.18°, which is larger than that for a planar geometry.

In the past, solid-state NMR work was restricted to HX or FX type dual-channel probe experiments at moderate spinning speeds where it was impossible to decouple ^{1}H and ^{19}F nuclei simultaneously and to remove D_{Sn-F} contribution to the sideband manifold, making high-resolution in ^{119}Sn NMR spectroscopy elusive and accurate measurement of Sn shielding tensors difficult. Today with the ^{1}H-^{19}F-^{n}X (HFX) triple-channel probes, it is possible to obtain ^{1}H and ^{19}F double decoupled and single decoupled $^{19}F\{^{1}H\}$ as well as $^{1}H\{^{19}F\}$ spectra, leading to high-resolution spectra. This technique is not common due to the experimental difficulty to decouple ^{1}H and fluorine ^{19}F simultaneously, as their resonance frequencies are very close (i.e., 499.99 MHz for ^{1}H and 469.79 MHz for ^{19}F at 11.7 T).

Only the $^{13}C\{^{1}H\}$[15,24] and the $^{119}Sn\{^{1}H\}$[14,23] NMR spectra have been reported in the literature for solid Me_3SnF. To the best of our knowledge there is no literature available on the high-resolution, simultaneously ^{1}H- and ^{19}F- decoupled solid-state NMR spectra of ^{119}Sn and ^{13}C as well as one dimensional ^{1}H- decoupled ^{19}F solid-state NMR spectra. It is of primary importance to obtain sufficient resolution for all nuclei in a system to obtain true values for the spectral parameters independently.

The solution-state ^{119}Sn NMR spectrum of Me_3SnF dissolved in CH_3OH, showed a doublet at +30.0 ppm with a $^1J(^{119}Sn\text{-}^{19}F)$ of 1630 Hz, while the ^{19}F NMR spectrum has a singlet at –156.0 ppm, with tin satellites having $^1J(^{119}Sn\text{-}^{19}F)$ of 1630 Hz, which supports its monomeric nature.[24] This is in contrast to the solid-state ^{119}Sn spectra containing triplets, thus inferring a penta-coordinate arrangement about Sn by assuming equivalence of the fluorine atoms.[2,23]

In one of the attempts to understand the structure of Me_3SnF in detail, dimethylphenyltin fluoride Me_2PhSnF was prepared and its structure was investigated by Beckmann *et al.* [25] This compound has a melting point of 124-126°C which is lower than the melting point of Me_3SnF (360°C). The lower melting point of Me_2PhSnF was explained by the lower symmetry of trialkyltin group in Me_2PhSnF. Its structure is also polymeric with a penta-coordinated tin. The X-ray analysis of Me_2PhSnF presents a distorted rod-like polymeric arrangement with an almost symmetric Sn—F—Sn bridge and F—Sn—F angle of 179.44(7)°. The Sn—F bond lengths are 2.162(1) and 2.179(1) Å. In the crystal lattice it forms stapled layers of parallel and isolated polymer chains having the shortest distance of 3.656(4) Å between them.[21] The solid-state $^{119}Sn\{^1H\}$ NMR spectra showed a triplet at –49.3 ppm with $^1J(^{119}Sn\text{-}^{19}F)$ of 1235 Hz indicating its polymeric structure.[25]

In an another attempt, $[Me_3SnF_2]^-$ was prepared by combining the 5:2 molar ratio of $Bu_4NF\cdot 3H_2O$ and Me_3SnCl.[24] Its solution-state NMR study in methanol gave a triplet in $^{119}Sn\{^1H\}$ NMR spectrum at –20 ppm, and a singlet in the $^{19}F\{^1H\}$ NMR spectrum at –133.5 ppm with ^{119}Sn satellites ($^1J(^{119}Sn\text{-}^{19}F)$ of 1318 Hz), indicating that the two fluorine atoms are equivalent.[24] However, the X-ray structure of this anion revealed a

slightly distorted trigonal-bipyramidal anion geometry with axial fluorine atoms deviating from linearity by an angle of 1.8°. The two Sn—F distances were 2.596 and 2.607 Å.[26] Thus one cannot assume that the $\hat{\hat{\boldsymbol{\sigma}}}$ and the $\hat{\hat{\mathbf{J}}}$ are axially symmetric and both co-axial with $\hat{\hat{\mathbf{D}}}$.

It is possible to get triplets in $^{119}Sn\{^{1}H\}$ NMR spectrum even when the two ^{19}F are not equivalent, as a strongly coupled AXY system can resemble to an AX_2 spin system if the resolution is not sufficient. This would be true under fast MAS rate, where the ΔJ and D effects have been largely removed. An example of magnetically inequivalent AXY spin system is shown in Scheme-IV, where angle β represents the angle X—A·····Y and the X and Y atoms have different orientation with respect to A. An example of such a strongly coupled spin system could be a bent F—Sn·····F system, where the fluorine tensors no longer need to be thought of as being axially symmetric. Even though the fluorine tensor components can still be the same, they will have different orientations. Hence, their isotropic chemical shift values can be the same, yet the nuclei are inequivalent.

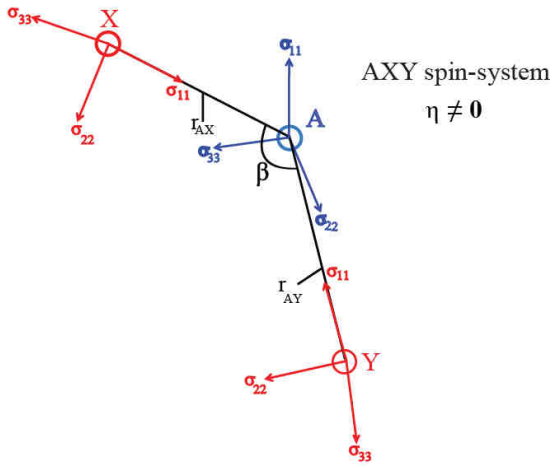

(Scheme-IV)

3.2 Solid-state NMR experiments

High-resolution ^{1}H, ^{19}F, ^{119}Sn, ^{13}C and $^{119}Sn\{^{1}H\}$ solid-state MAS NMR spectra were recorded using a Varian INOVA 500 wide-bore spectrometer equipped with T-3 Varian four-channel HFXY probes and are shown in Figures 3.3, 3.4, 3.5, 3.6, 3.7, 3.8, 3.9. The correct recycle delay for each nucleus was determined using the saturation recovery experiment. The pulse widths were calibrated by using nutation measurements. All spectra shown were recorded using either the 2.5-mm probe, the 3.2-mm probe, or the 4.0-mm four-channel HFXY probe with maximum MAS rotor spinning rates of 30 kHz, 25 kHz, or 18 kHz, respectively. The maximum powers used for the 2.5-mm, 3.2-mm, and 4.0-mm probes were 125, 100, and 62.5 kHz, which correspond to 90° pulse widths of 2.0 μs, 2.5 μs, and 4.0 μs, respectively. For each nucleus at least two experiments at different spinning frequencies ranging from 14-24 kHz were recorded to determine the isotropic chemical shift.

Chemical shielding anisotropy (σ_{aniso}) is defined by $\sigma_{aniso} = \sigma_{zz} - \sigma_{iso}$ and isotropic chemical shielding (σ_{iso}) is defined by $\sigma_{iso} = (\sigma_{xx} + \sigma_{yy} + \sigma_{zz})/3$ in the principal axis system according to the Mehring convention.[28] To convert $\sigma_{iso}(^{19}F)$ to chemical shift, δ_{iso}, $CFCl_3$ (σ_{iso} (^{19}F) = 0 ppm) was used as reference, $\delta_{iso} = \sigma_{iso(r)} - \sigma_{iso(s)}$, where the subscripts 'r' and 's' refer to the reference and sample, respectively. The asymmetry parameter (η), which indicates the deviation of the chemical shift tensor from cylindrical symmetry, is defined as $\eta = \frac{\delta_{yy}^{PAS} - \delta_{xx}^{PAS}}{\delta_{aniso}}$.

High-resolution, simultaneously ^{1}H and ^{19}F double-decoupled ^{13}C NMR spectra (Figure 3.3) were collected using the four-channel 3.2-mm probe in three-channel ^{1}H-^{19}F-

^{13}C mode. The 90° pulse width for the $^{13}C\{^{1}H,^{19}F\}$ spectrum was 2.0 μs using a recycle delay of 30 s at a spinning rate of 21 kHz. The acquisition time for the spectrum was 20.0 ms for 2000 number of complex points, and the decoupling powers on the ^{1}H and ^{19}F channels were 60 and 40 kHz, respectively. A total number of 1726 transients were recorded. The signal has an isotropic chemical shift of 2.3 ppm with a line width of 80 Hz.

Direct-polarization and cross-polarization were used to record $^{1}H\{^{19}F\}$ NMR spectra (Figure 3.4). Direct-polarization $^{1}H\{^{19}F\}$ NMR spectra were collected using the 2.5-mm four-channel-HFXY probe in three-channel-HFC mode. The 90° pulse width was 2.0 μs long and a recycle delay of 15 s was used. The acquisition time was 4.096 ms for 2048 complex points. A decoupling power of 50 kHz was used on the ^{19}F channel. The line width was of 1506 Hz. A total number of 16 transients was recorded. The ^{19}F- to ^{1}H-cross-polarization technique was employed to record the $^{1}H\{^{19}F\}$ NMR spectrum (Figure 3.4b). For cross polarization the matching power used was 40.6 kHz to match the Hartmann-Hahn condition and the contact time used was 2.5 ms. A total of 136 number of transients was recorded.

The $^{19}F\{^{1}H\}$ NMR spectra at various spinning rates were collected using the 2.5-mm four-channel HFXY probe in three-channel ^{1}H-^{19}F-^{13}C mode (Figure 3.5 and 3.7). The 90° pulse width was 2.0 μs and the recycle delay was 360 s. The acquisition time was 4.096 ms for 2048 complex points. The decoupling power used was 63 kHz. The best line width achieved was 287 Hz at a spinning rate of 24 kHz.

The high-resolution double-decoupled $^{119}Sn\{^{1}H,^{19}F\}$ NMR spectra (Figure 3.8) were collected using 2.5-mm four-channel probe in three-channel ^{1}H-^{19}F-^{119}Sn mode. For

the acquisition of the $^{119}Sn\{^{1}H,^{19}F\}$ NMR spectrum, a 90° pulse width of 4.0 μs was used with a recycle delay of 30 s at a spinning rate of 18 kHz. The acquisition time for the spectrum was 4.096 ms for 2048 complex points. Two-pulse phase-modulated (tppm)[27] decoupling was used on the ^{1}H channel with a decoupling power of 125 kHz. The pulse width used for tppm decoupling was 5 μs with a phase of 13°. The decoupling power used on ^{19}F channel was 46.8 kHz. A total number of 900 scans was collected, which gave a signal-to-noise ratio of 50.2 and a line width of 461 Hz.

The high-resolution single-decoupled $^{119}Sn\{^{1}H\}$ NMR spectra (Figure 3.9) were collected using the 2.5-mm four-channel HFXY probe in three-channel ^{1}H-^{19}F-^{119}Sn mode at different spinning rates. The 90° pulse width used was 2.7 μs with a recycle delay of 30 s, and an acquisition time of 4.096 ms was used for 2048 complex points. The decoupling power on the ^{1}H channel was 57.8 kHz. A total of 1816 scans was collected giving a signal-to-noise ratio of 85.7, and the best line width obtained was of 231 Hz.

3.3 Results

The spectral parameters for the ^{13}C and the ^{1}H nuclei were determined independently as the $^{13}C\{^{1}H,^{19}F\}$ and $^{19}F\{^{1}H\}$ NMR spectra are not influenced by each other and by the remaining nuclei. In the $^{13}C\{^{1}H,^{19}F\}$ and $^{19}F\{^{1}H\}$ NMR spectra, the effect of tin is seen as satellites, however, not on the central peaks of each sideband. In contrast, the ^{19}F and ^{119}Sn nuclei share parameters in the $^{119}Sn\{^{1}H\}$ NMR spectra and thus their NMR spectra are strongly interdependent. The spectral parameters for the ^{19}F and ^{119}Sn nuclei can be determined independently by simulating the spectra over various spinning rates and achieve self consistency in them.

Solid-state ^{13}C MAS NMR Spectroscopy

Double-decoupled $^{13}C\{^{1}H,^{19}F\}$ MAS NMR spectroscopy of Me_3SnF revealed only a single resonance (Figure 3.3). The isotropic carbon chemical shift was 2.3 ppm with satellites due to coupling to the ^{119}Sn nucleus with $^{1}J(^{119}Sn\text{-}^{13}C)$ of 511.4 Hz. This sole CH_3 resonance peak in this spectrum indicates the equivalence of all the methyl groups on the NMR time scale.

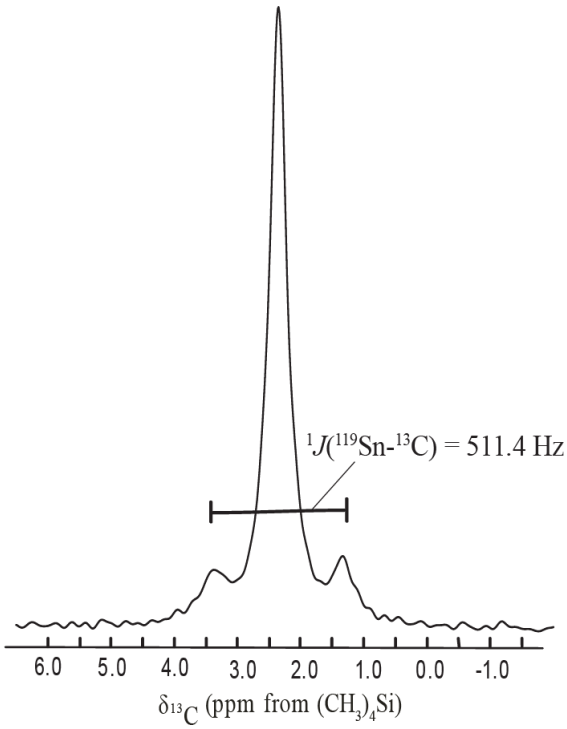

Figure 3.3: $^{13}C\{^{1}H,^{19}F\}$ MAS NMR spectrum of Me_3SnF at a spinning rate of 21 kHz. Acquisition parameters are: 90° pulse width of 2.0 μs; acquisition time of 20.0 ms; recycle delay of 30 s; decoupling power of 60 kHz on ^{1}H channel and 40 kHz on ^{19}F channel; 1726 number of scans with signal-to-noise ratio of 26.6.

Solid-state ^{1}H MAS **NMR Spectroscopy**

The $^{1}H\{^{19}F\}$ MAS NMR spectrum contains two distinct proton signals, one of which is assigned to the methyl protons at 0.3 ppm and another at around 7.0 ppm,

corresponding to water (Figure 3.4). The presence of moisture was confirmed by ^{19}F to ^{1}H cross polarization, in which polarization transfer from fluorine to water protons cannot take place due to the high mobility of the water molecules and the large average distance between the ^{19}F and the ^{1}H nuclei. In this case, only one proton signal for the CH_3 was observed (Figure 3.4).

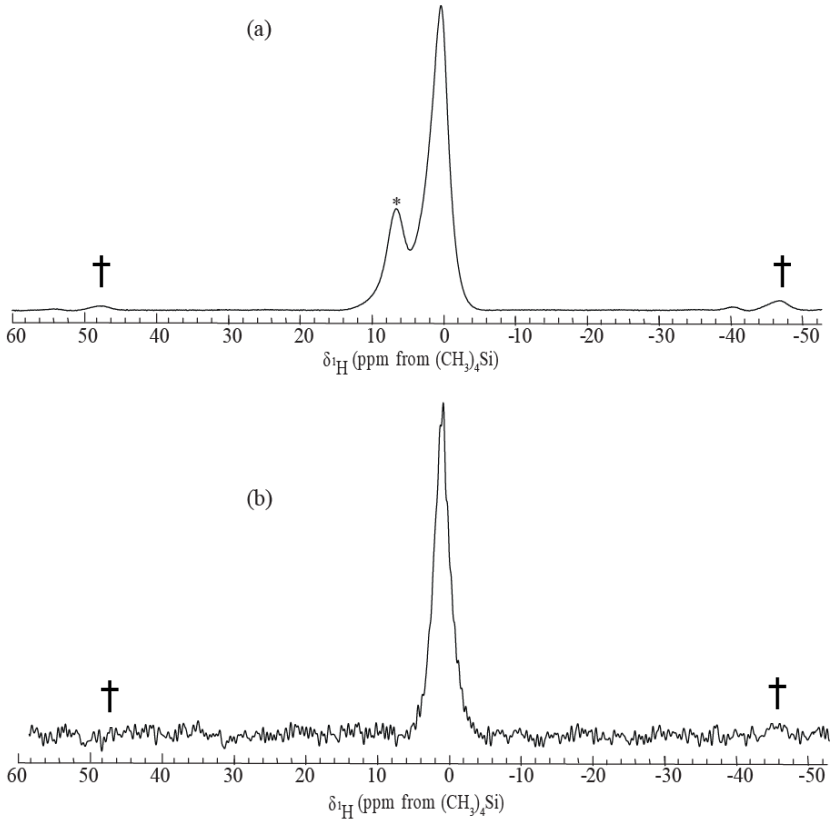

Figure 3.4 (a) $^{1}H\{^{19}F\}$ MAS NMR spectrum of Me_3SnF at a spinning rate of 24 kHz; and (b) $^{1}H\{^{19}F\}$ (^{19}F to ^{1}H CP) MAS NMR spectrum of Me_3SnF. Acquisition parameters are: 90° pulse width of 2.0 μs; acquisition time 4.096 ms; recycle delay of 4 s; decoupling power on ^{19}F channel used was 50 kHz; 136 number of scans, line width of 1506 Hz. Additional parameters for cross polarization are crossp 1300 and contact time 2.5 ms. The peak marked with '*' is probably due to water in the crystal lattice because it is not present in the ^{19}F to ^{1}H cross-polarized experiment. '†' denote spinning sidebands.

Solid-state ^{19}F MAS NMR Spectroscopy

The $^{19}F\{^{1}H\}$ MAS NMR spectrum shows a side-band pattern centered around the isotropic chemical shift of –134.3 ppm. Figure 3.5(b) shows the experimental spectrum and Figure 3.5(a) depicts the simulated spectrum. This spectrum contains additional features due to couplings to the ^{119}Sn nuclei. The resolution was good enough to resolve the ^{119}Sn satellite signals and, hence, to determine the $^{1}J(^{119}Sn\text{-}^{19}F)$ coupling constant of 1320 Hz. The dipolar coupling values were optimized as shown in Figure 3.5 and found to be consistent at different spinning rates. Fluorine-19 NMR parameters obtained from spectral simulations using SIMPSON are given in the Table 3.2.

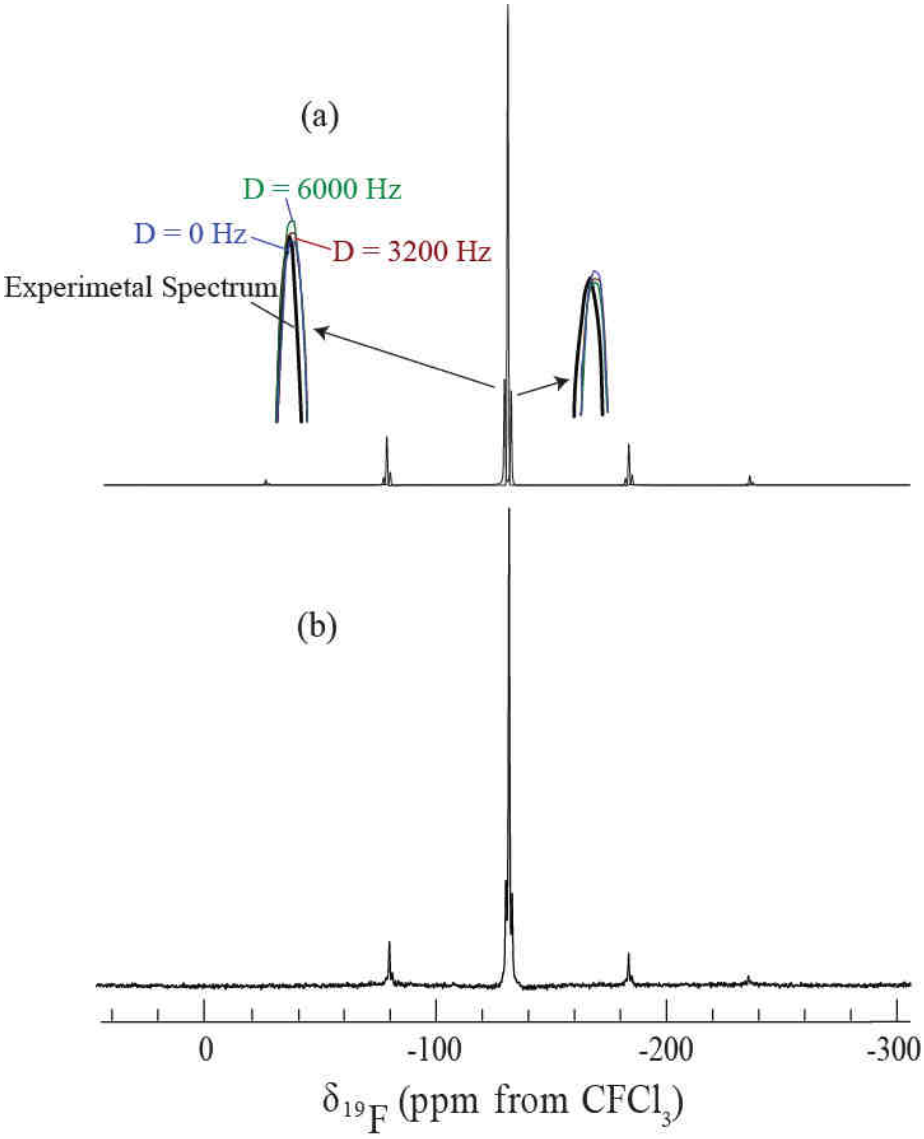

Figure 3.5 (a) Simulated and (b) experimental spectrum of $^{19}F\{^{1}H\}$ MAS NMR spectrum of Me_3SnF at a spinning rate of 24 kHz. Acquisition parameters: 90° pulse width of 2.0 μs; acquisition time of 4.096 ms; recycle delay of 360 s; decoupling power on ^{1}H channel used was of 63.0 kHz; 8 number of scans with signal-to-noise ratio of 398.

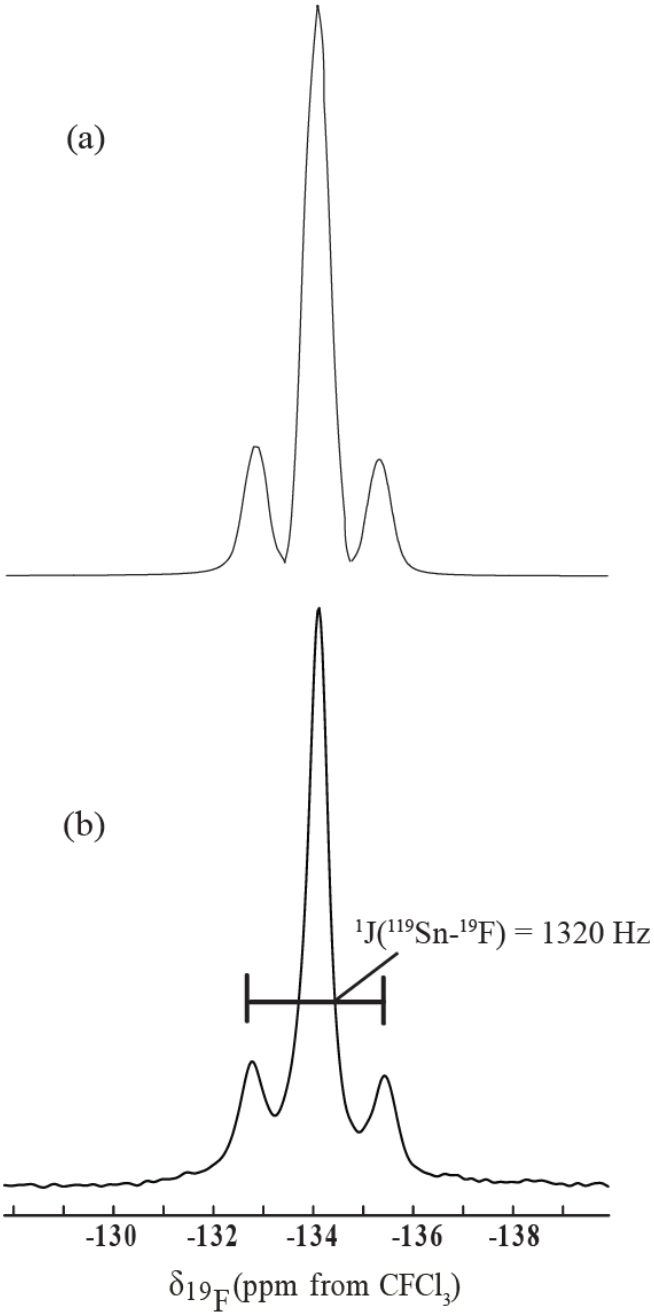

Figure 3.6 Isotropic line of the (a) simulated and (b) experimental spectrum of $^{19}F\{^{1}H\}$ MAS NMR spectrum of Me_3SnF at a spinning rate of 24 kHz. Acquisition parameters: 90° pulse width of 2.0 μs; acquisition time of 4.096 ms; recycle delay of 360 s; decoupling power on ^{1}H channel used was of 63.0 kHz; 8 number of scans with signal-to-noise ratio of 398.

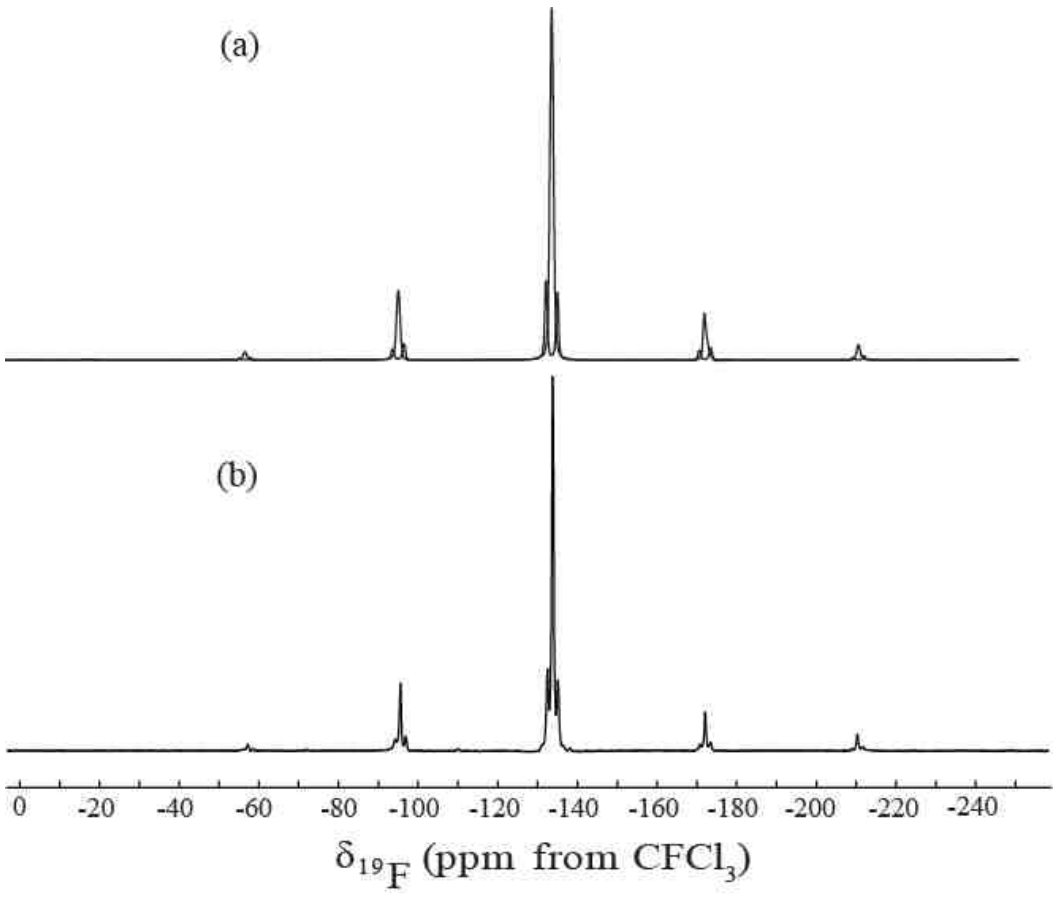

Figure 3.7 (a) Simulated and (b) experimental spectrum of $^{19}F\{^{1}H\}$ MAS NMR spectrum of Me_3SnF at a spinning rate of 18 kHz. Acquisition parameters: 90° pulse width of 2.0 μs; acquisition time of 4.096 ms; recycle delay of 360 s; decoupling power on ^{1}H channel used was of 63.0 kHz; 8 number of scans with signal-to-noise ratio of 398.

Table 3.2 Parameters for $^{19}F\{^{1}H\}$ MAS NMR spectra

NMR parameters		NMR parameters	
δ_{iso} (ppm)	-134.3 ± 0.1	Dipolar coupling (^{119}Sn-$^{19}F_1$)[c] (Hz)	4266
δ_{aniso}(ppm)[a]	-55.35 ± 0.42	Dipolar coupling (^{119}Sn-$^{19}F_2$) (Hz)	3200
η[b]	0.60 ± 0.05	Dipolar coupling ($^{19}F_1$-$^{19}F_2$)[d] (Hz)	-1185
$^{1}J(^{119}Sn$-$^{19}F)$ (Hz)	1320 ± 20	Angle Sn—F·····Sn (°)[e]	141
$\Delta J(^{119}Sn$-$^{19}F_1)$ (Hz)[f]	-800		
$\Delta J(^{119}Sn$-$^{19}F_2)$ (Hz)[f]	3200 ± 100		

[a]δ_{aniso}: The range of chemical shifts of a molecule with respect to the external magnetic field (according to M. Mehring convention).[28]

[b]asymmetry (η): It indicates the line shape deviation from axially symmetric tensor (according to M. Mehring convention).[28]

[c]Dipolar coupling value is based on the r_{Sn-F1}= 2.15 Å, which was determined by X-ray crystallography.

[d]Estimated dipolar coupling by comparing the experimental and simulated spectra

[e]Angle Sn—F·····Sn indicates that the Sn—F·····Sn moiety is bent along the axis of fluorine atom, (known from X-ray crystallography).[13]

[f] ΔJ values were taken from Figure 3.2.

Solid-state ^{119}Sn MAS NMR Spectroscopy

Solid-state ^{119}Sn{^{1}H,^{19}F} MAS NMR Spectroscopy

The ^{119}Sn{^{1}H,^{19}F} NMR spectra show only one spinning side-band manifold, indicating the presence of only one Sn environment and, thus, confirming that only one tin is present in the crystallographic asymmetric unit (Figure 3.8). Figure 3.8(b) is the experimental spectrum and Figure 3.8(a) depicts its simulated spectra. The NMR parameters for ^{119}Sn{^{1}H,^{19}F} NMR spectrum obtained using SIMPSON simulations are given in the Table 3.3. The isotropic chemical shift for the ^{119}Sn nucleus is +24.3 ± 0.1 ppm and the chemical shift anisotropy is 211.92 ± 2.68 ppm. The asymmetry parameter was determined as 0.60 ± 0.05. Simulations showing the effect of variation in the asymmetry parameter on the sideband pattern are shown in Figure 3.8, which clearly shows that 0.60 ± 0.05 is the best fit for experimental spectrum. In a high-resolution experiment using the tppm decoupling sequence for ^{1}H and cw for ^{19}F, satellites could be resolved around the isotropic signal (Figure 3.9). These satellites arise from the ^{2}J(^{119}Sn-^{117}Sn) coupling. Notice that the isotropic signal contains well resolved tin satellites well above the baseline. The ^{2}J(^{119}Sn-^{117}Sn) was determined by simulating the tin satellite parameters using the shielding parameters of tin nucleus determined previously. This is the first observation of such a ^{2}J(^{119}Sn-^{117}Sn) coupling for this system in the solid-state. This is likely a consequence of being able to do ^{1}H and ^{19}F decoupling, giving a better resolution compared to the earlier two channel (HX) ^{119}Sn NMR studies.

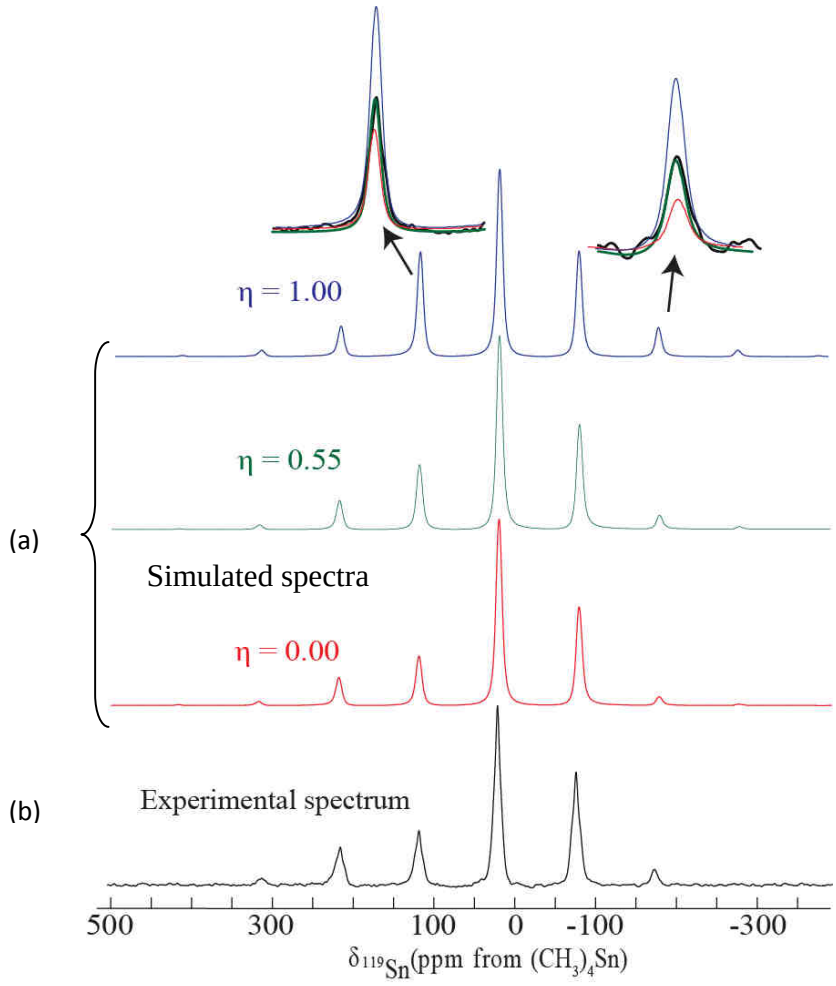

Figure 3.8 Effect of variation of the asymmetry (η) parameter of CSA on the intensity of the peaks in the simulated $^{119}Sn\{^{1}H,^{19}F\}$ MAS NMR spectrum of Me_3SnF at a spinning rate of 18 kHz. Figure 3.8 (a) represents the simulated spectra and Figure 3.8 (b) represents the experimental spectrum.

Table 3.3 Parameters for $^{119}Sn\{^{1}H, ^{19}F\}$ MAS NMR spectra

δ_{iso} (ppm)	δ_{aniso} (ppm)[a]	η[b]
+24.3 ± 0.1	-211.92 ± 2.68	0.60 ± 0.05

[a] δ_{aniso}: The range of chemical shifts of a molecule with respect to the external magnetic field (according to M. Mehring convention) [28]

[b] asymmetry (η): It indicates the line shape deviation from axially symmetric tensor (according to M. Mehring convention) [28]

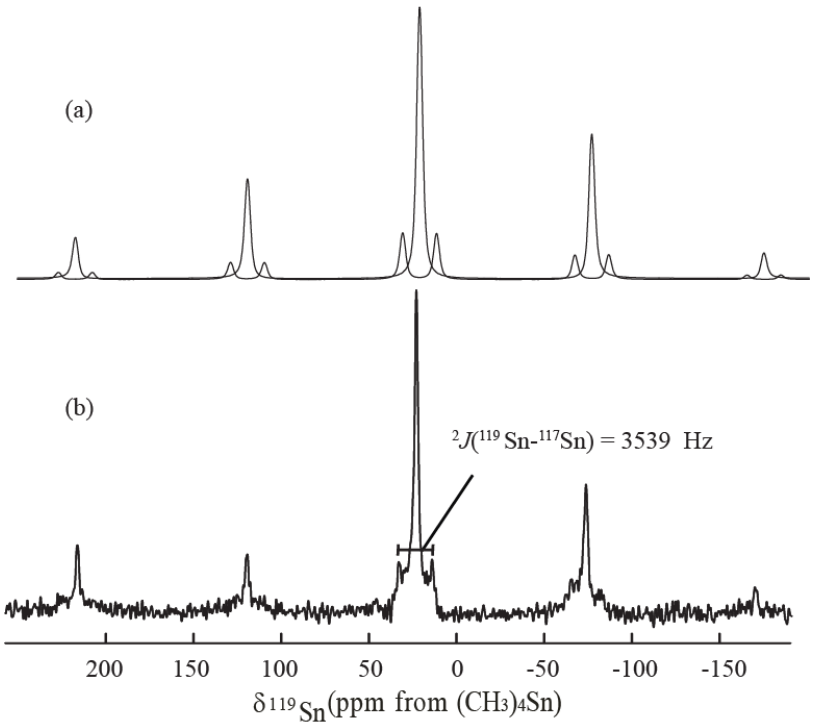

Figure 3.9 Solid-state $^{119}Sn\{^1H,^{19}F\}$ MAS NMR spectrum of Me_3SnF at a spinning rate of 18 kHz: (a) simulated and (b) experimental spectrum. Acquisition parameters: 90° pulse width of 4.0 μs; acquisition time of 4.096 ms; recycle delay of 30 s; decoupling power of 125 kHz on ^1H channel with tppm decoupling and pw = 5 μs; decoupling power used for ^{19}F of 56.8 kHz; 900 scan with a signal-to-noise ratio 50.2.

The isotope pattern resulting from $^2J(^{119}Sn\text{-}^{117}Sn)$ coupling in the $^{119}Sn\{^1H,^{19}F\}$ NMR spectrum is better understood from the following discussion. The natural abundance of ^{119}Sn nucleus is 8.58% and that of ^{117}Sn is 7.61%. The third NMR-active nucleus ^{115}Sn is only 0.35% abundant, so its presence can be neglected. In this way the relative abundances of the spin-inactive ^{118}Sn and these nuclei with respect to ^{117}Sn are $^{118}Sn : {}^{119}Sn : {}^{117}Sn = 11.01 : 1.12 : 1.00$.

Table 3.4: Calculation of the intensity of peaks due to ^{2}J-coupling among tin isotopes

Sn—^{19}F—^{119}Sn—^{19}F —Sn (mass no)		Probability ratio of simultaneous occurrence of different isotopes		Normalized Peak ratio (%)
118	118	11.01 × 11.01 =	121.22	100
117 118	118 117	1 × 11.01 + 11.01 × 1 =	22.02	18
119 118	118 119	1.12 × 11.01 + 11.01 × 1.12 =	24.66	20†
117 119 119 117	119 117 119 117	1 × 1.12 + 1.12 × 1 + 1.12 × 1.12 + 1 × 1 =	4.49	0.04*

† not observed, *can be neglected

On the basis of the calculation given in Table 3.4, the relative intensity of the ^{119}Sn satellites in the ^{119}Sn{^{1}H,^{19}F} NMR spectrum, due to ^{2}J(^{119}Sn-^{119}Sn) coupling should be 20% with respect to the main ^{119}Sn signal. However, the spinning rate of the sample is fast enough to eliminate the ^{2}J(^{119}Sn-^{119}Sn) coupling anisotropy, thus eliminating the possibility of observing ^{2}J(^{119}Sn-^{119}Sn) coupling. The relative intensity of the ^{117}Sn satellites due to ^{2}J(^{119}Sn-^{117}Sn) coupling should be 18% with respect to the main ^{119}Sn signal, which was observed in the ^{119}Sn{^{1}H,^{19}F} NMR spectrum (Figure 3.9). The ^{2}J(^{119}Sn-^{117}Sn) coupling was 3539 Hz for trimethyltin fluoride (Table 3.3).

Solid-State ^{119}Sn{^{1}H} NMR Spectroscopy

High-resolution proton-decoupled ^{119}Sn{^{1}H} MAS NMR spectra were collected at various spinning rates as shown in Figure 3.10, with the corresponding simulated spectra on the side. All the spectra consist of sideband patterns of triplets. The shielding

parameters and heteronuclear coupling parameters for ^{119}Sn and ^{19}F nuclei have been determined previously. These are now employed in the simulation of the $^{119}Sn\{^{1}H\}$ spectra to determine the remaining coupling parameters. The triplet in the $^{119}Sn\{^{1}H\}$ NMR spectrum is often considered as indicative of equivalence between fluorine nuclei. This would be true if the magic angle spinning rate is sufficiently large to average the dipolar couplings and *J*-anisotropies (ΔJ). Note however that the triplets in the $^{119}Sn\{^{1}H\}$ MAS NMR spectra exhibit a roofing effect (unsymmetrical intensities triplet), presumably due to residual effects from the ΔJ and dipolar coupling (Fig 3.14 and 3.15) still present at this spinning rate, which indicate that the fluorine nuclei are not equivalent. Consequently individual values should be obtained for each fluorine nucleus.

Estimates for both ΔJ values were obtained through simulations as illustrated in Figures 3.11 and 3.12. The effect of varying angle-β is shown in Figure 3.13. The dipolar coupling value for one of the fluorines is based on the known internuclear distance from X-ray crystallography. That of the parameter for the other fluorine environment was obtained through simulation, as shown in Figures 3.14 and 3.15. The NMR parameters consistent with the $^{119}Sn\{^{1}H\}$ NMR spectra obtained over various spinning rates are given in the Table 3.5.

Table 3.5 Parameters for $^{119}Sn\{^{1}H\}$ MAS NMR spectra

NMR parameters		NMR parameters	
δ_{iso} (ppm)	+24.3 ± 0.1	Angle F—Sn·····F (β)[b]	165 ± 3°
δ_{aniso} (ppm)[a]	-211.92 ± 2.68	Dipolar coupling	4266
$\Delta J(^{119}Sn\text{-}^{19}F_1)$ (Hz)	-800[d]	$(^{119}Sn\text{-}^{19}F_1)$ (Hz)	[2.15]
		$[r_{Sn-F}(Å)]$	
$\Delta J(^{119}Sn\text{-}^{19}F_2)$ (Hz)	3200 ± 100	Dipolar coupling	3200 ± 100
		$(^{119}Sn\text{-}^{19}F_2)$ (Hz)	[2.37 ± 0.02]
		$[r_{Sn-F}(Å)]$	
$^{1}J(^{119}Sn\text{-}^{19}F_1)$ (Hz)	1320 ± 20		
		η[c]	0.60 ± 0.05
$^{1}J(^{119}Sn\text{-}^{19}F_2)$ (Hz)	1320 ± 20		

$Sn\text{-}F_1$, short Sn—F distance

$Sn\text{-}F_2$, long Sn·····F distance

[a] δ_{aniso}: The range of chemical shifts of a molecule with respect to the external magnetic field (according to M. Mehring convention) [28]

[b] angle F—Sn·····F(β): It indicates one of the angle between two ^{119}Sn to ^{19}F chemical shift tensors or *J*-coupling tensors [29]

[c] asymmetry (η): It indicates the line shape deviation from axially symmetric tensor (according to M. Mehring convention) [28]

[d] ΔJ values were taken from Figure 3.2.

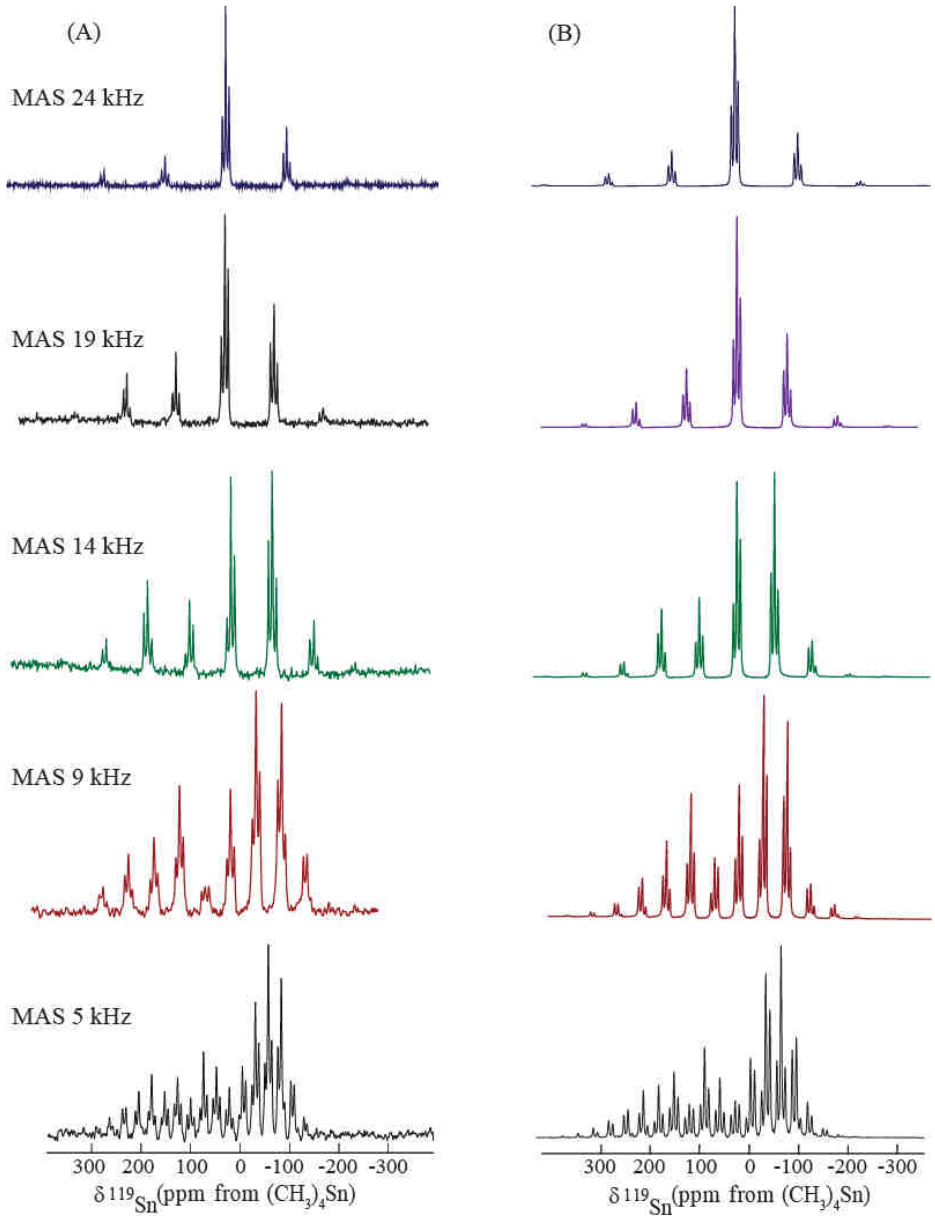

Figure 3.10 Summary of (A) experimental and (B) simulated $^{119}Sn\{^{1}H\}$ MAS NMR $^{119}Sn\{^{1}H\}$ spectra of Me_3SnF at different spinning rates from 5 kHz to 24 kHz. Simulated spectra are on right hand side and experimental spectra are on left hand side. Acquisition parameters are: 90° pulse width of 2.7 μs; acquisition time of 4.096 ms; recycle delay of 30 s; decoupling power on ^{1}H channel of 57.8 kHz; 1816 number of scans with signal-to-noise ratio of 85.7.

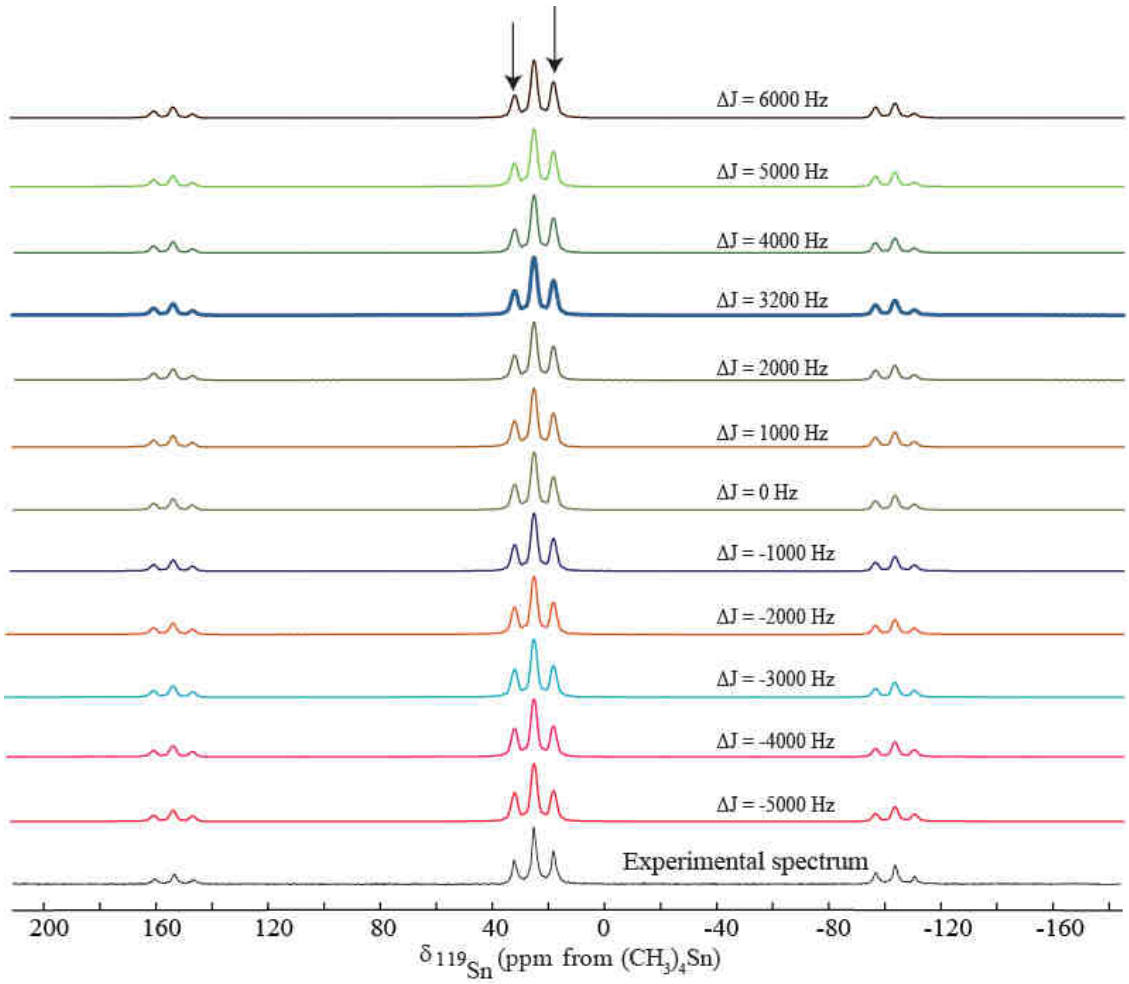

Figure 3.11 Effect of variation of *J*-anisotropy of Sn—F_2 bond on the intensity of the peaks in the $^{119}Sn\{^1H\}$ MAS NMR spectrum of Me_3SnF at spinning speed of 24 kHz. The of *J*-anisotropy of Sn—F_1 bond is fixed to -800 Hz. Dipolar coupling for Sn—F_1 bond and Sn—F_2 bond are 4266 and 3200 Hz respectively.

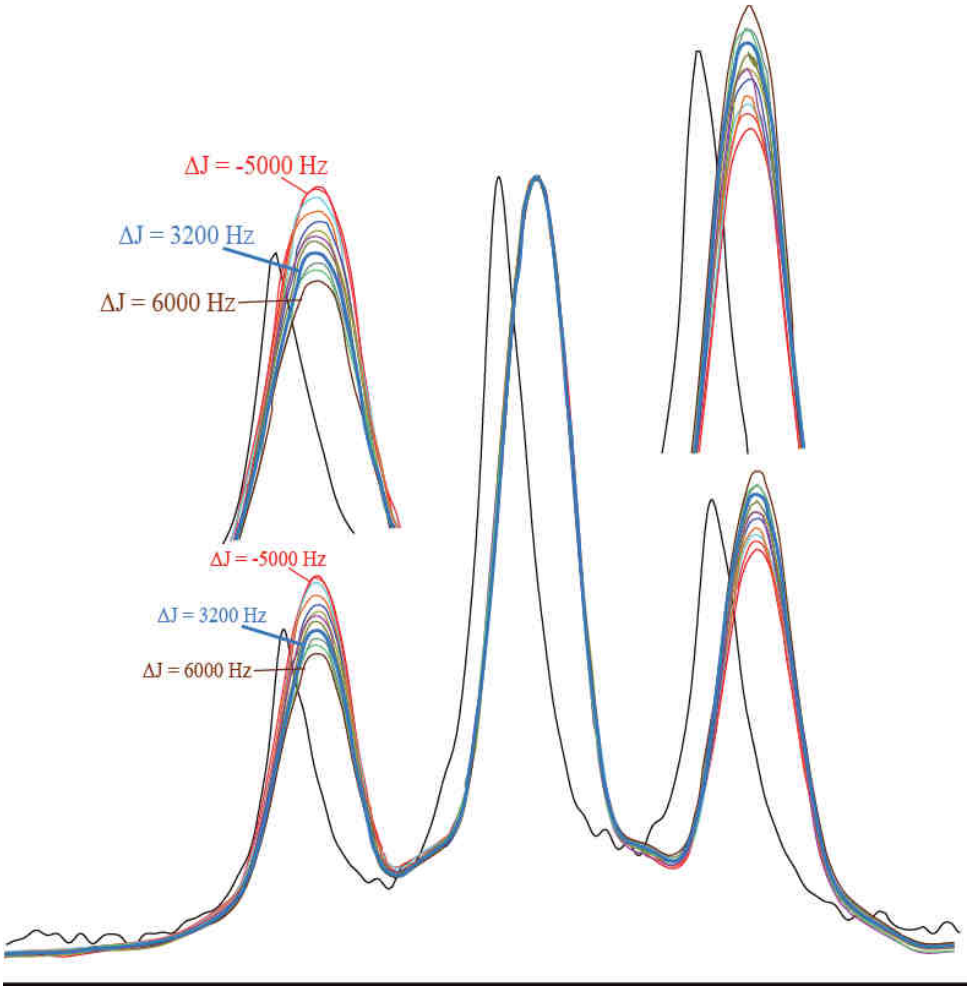

Figure 3.12 Effect of variation of *J*-anisotropy of Sn—F_2 bond on the intensity of the central peak in the $^{119}Sn\{^1H\}$ MAS NMR spectrum of Me_3SnF at MAS 24 kHz in Figure 3.10. The of *J*-anisotropy of Sn—F_1 bond is fixed to -800 Hz. Dipolar coupling for Sn—F_1 bond and Sn—F_2 bond are 4266 and 3200 Hz respectively.

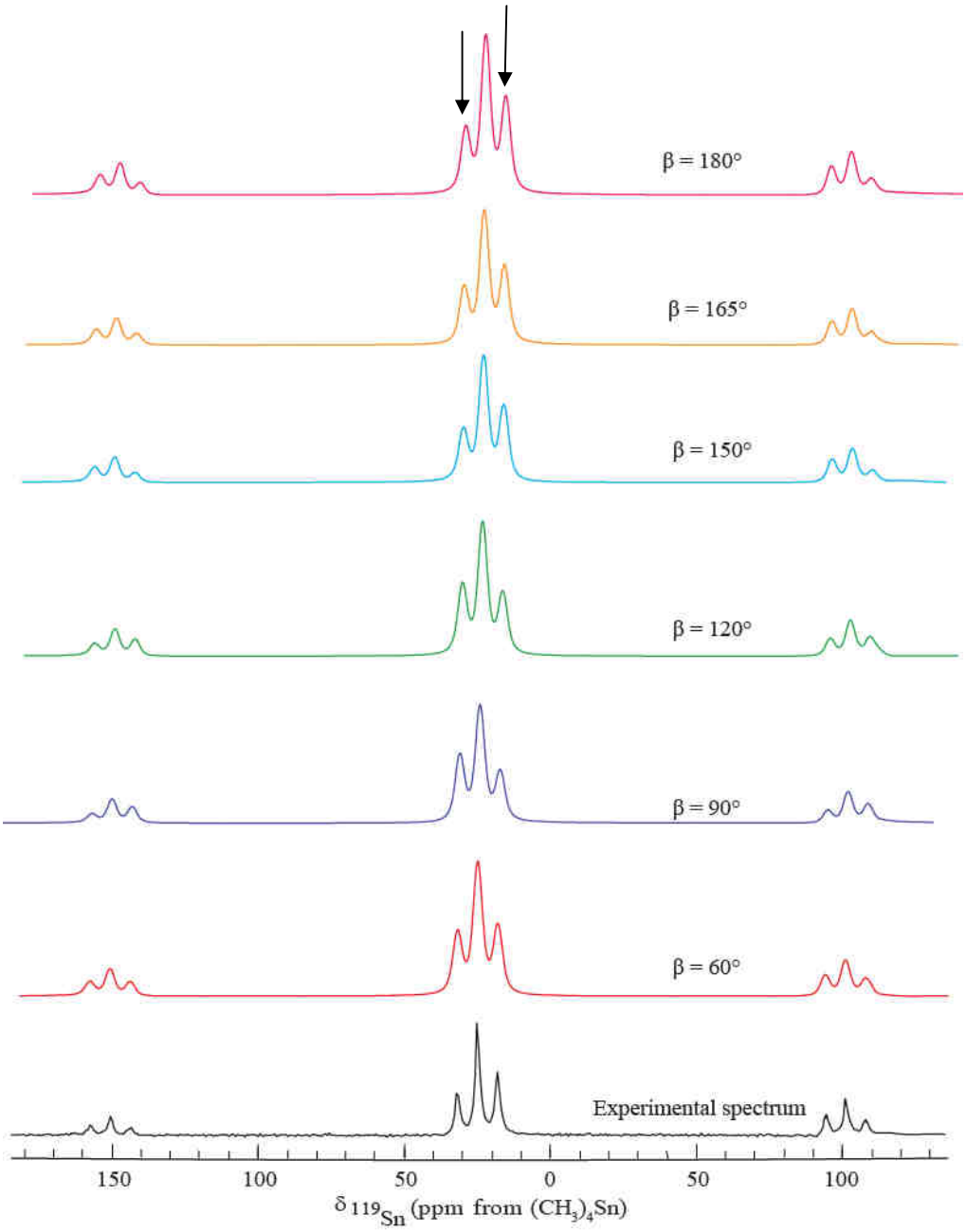

Figure 3.13 Effect of variation of the β-angle (angle F—Sn· · · · F) on the intensity of the peaks in the simulated $^{119}Sn\{^{1}H\}$ MAS NMR spectrum of Me_3SnF at a spinning rate of 24 kHz. Dipolar couplings for the Sn—F_1 and Sn—F_2 bond are 4266 and 3200 Hz, respectively. *J*-anisotropy of Sn—F_1 bond and Sn—F_2 bond are -800 and 3200 respectively.

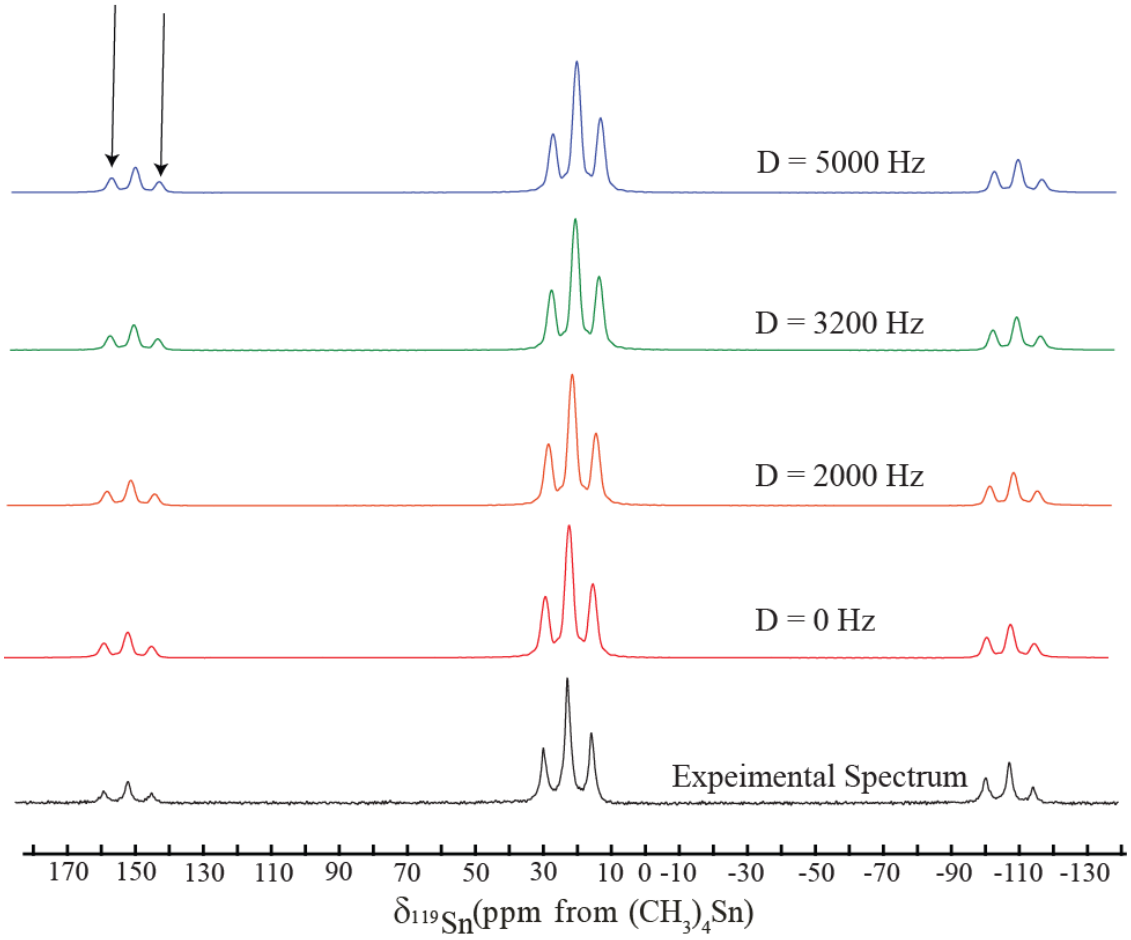

Figure 3.14 Effect of variation of dipolar coupling of Sn—F_2 bond on the intensities of the peaks in the $^{119}Sn\{^1H\}$ MAS NMR spectrum of Me_3SnF at MAS 24 kHz. The dipolar coupling of Sn—F_1 bond is fixed as 4266 Hz. Angle F—Sn· · · · · F is 165° and *J*-anisotropy of Sn—F_1 bond and Sn—F_2 bond are -800 and 3200 respectively.

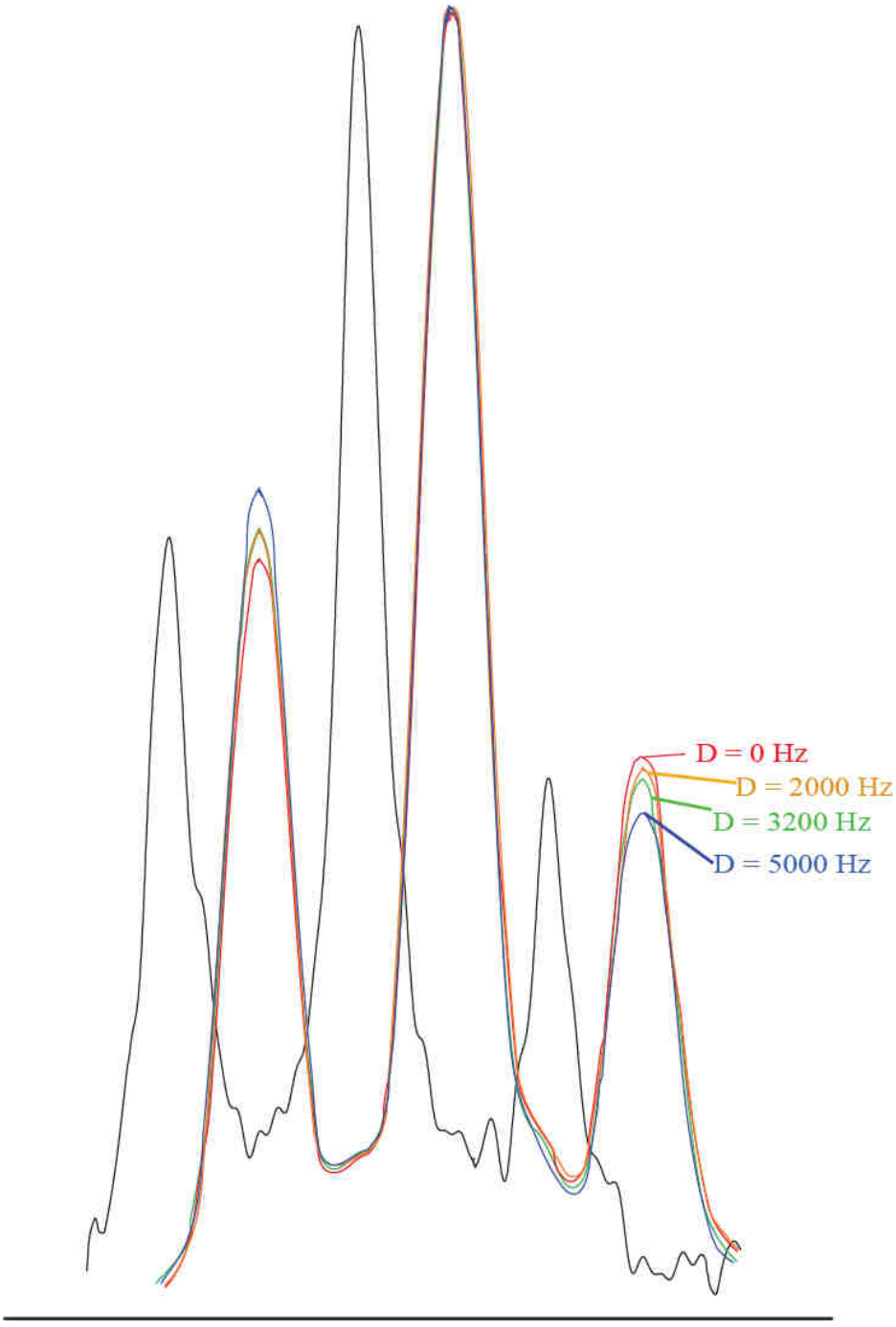

Figure 3.15 Effect of variation of dipolar coupling of Sn—F_2 bond on the intensity on one of the sideband signal in the $^{119}Sn\{^1H\}$ MAS NMR spectrum of Me_3SnF at MAS 24 kHz in Figure 3.13. The dipolar coupling of Sn—F_1 bond is fixed as 4266 Hz. *J*-anisotropy of Sn—F_1 bond and Sn—F_2 bond are -800 and 3200 respectively.

3.4 Discussion

Solid-State ^{13}C NMR Spectroscopy

The single ^{13}C resonance and the lack of spinning sidebands are most likely the result of very rapid interchange of the three methyl groups about tin at ambient temperature, resulting in them being equivalent on the NMR time-scale. The $^{13}C\{^{1}H\}$ NMR study of Me_3SnF by Lockhart and Manders[20] revealed a $^{1}J(^{119}Sn\text{-}^{13}C)$ coupling of 550 Hz, which was not well resolved due to coupling to ^{19}F nuclei and poor signal-to-noise ratio. The high-resolution double-decoupled $^{13}C\{^{1}H,^{19}F\}$ NMR spectrum provided the more accurate coupling for $^{1}J(^{119}Sn\text{-}^{13}C)$ of 511.4 Hz (Figure 3.3) with a line width of 80 Hz and good signal-to-noise ratio. Presumably, the fast motion about the Sn—C bond reduces the heteronuclear proton to carbon dipolar coupling, facilitating proton decoupling and, thus, improving the resolution significantly. The Me—Sn—Me angle was calculated from the $^{1}J_{Sn\text{-}C}$ (511.4 Hz) using the empirical relationship given by Lockhart and Manders (Eq. 3.5),[20,21,22] giving value of 120.5 ± 0.4°. This angle supports the average trigonal planar arrangement of the methyl groups about tin.

Solid-State ^{1}H NMR Spectroscopy

One-channel $^{1}H\{^{19}F\}$ NMR work on trimethyltin fluoride is novel as $^{1}H\{^{19}F\}$ NMR methods are not commonly available. The $^{1}H\{^{19}F\}$ CP NMR spectrum contains one signal corresponding to the methyl protons. Typically ^{1}H NMR spectra are severely broadened by the strong homonuclear dipolar coupling. In contrast, the methyl signal in the ^{1}H NMR spectrum is relatively narrow. This high resolution is presumably a consequence of rapid motion of the CH_3 groups about Sn—C bond, where the dipolar

coupling among protons are reduced. This is further supported by the fact that the sideband intensities are significantly reduced (Fig 3.4).

Solid-state ^{19}F MAS NMR Spectroscopy

A singlet was obtained in the $^{19}F\{^{1}H\}$ NMR spectrum indicating that only one fluorine environment can be discerned. The isotropic chemical shift at –134.3 ppm is in good agreement with the solution-state value of –156.0 ppm, where Me_3SnF is known to be monomeric.[24] The $^{1}J(^{119}Sn\text{-}^{19}F)$ coupling constant of 1320 Hz is also very close to that found in solution state (1630 Hz) [24] (Figure 3.6). The asymmetry parameter of 0.60 ± 0.05 indicates the non-linearity of the Sn—F·····Sn moiety (Table 3.2). This is in agreement with the X-ray study by Clark *e. al.*[4] At a spinning rate of 24 kHz, both, the homonuclear and heteronuclear, dipolar couplings with ^{19}F are reduced and, thus, do not affect the sideband intensities, allowing the true chemical shielding tensor parameters to be obtained with high accuracy.

Solid-state ^{119}Sn MAS NMR Spectroscopy

Solid-state $^{119}Sn\{^{1}H,^{19}F\}$ MAS NMR Spectroscopy

In the case of $^{119}Sn\{^{1}H,^{19}F\}$ NMR spectrum, an asymmetry parameter of 0.60 ± 0.05 indicates the nonlinearity of the F—Sn·····F moiety. This spectrum also revealed the $^{2}J(^{119}Sn\text{-}^{117}Sn)$ coupling for the first time, which supports the polymeric structure of Me_3SnF. The first observation of such a $^{2}J(^{119}Sn\text{-}^{117}Sn)$ coupling was made by R. K. Harris in 1985 on tetrakis(trimethylstannyl)methane, which was 328 ± 8 Hz.[30] In this compound the carbon is tetrahedral and the spin polarization is propagated through σ-

bonds. The $^{2}J(^{119}Sn\text{-}^{117}Sn)$ in Me_3SnF was found to be 3539 Hz. These types of large $^{2}J(^{119}Sn\text{-}^{117}Sn)$ scalar-couplings have been rarely mentioned in literature. For example, the $^{2}J(^{119}Sn\text{-}^{119}Sn)$ coupling constant for $[(CH_3)_2SnFe(CO)_4]_2$ was found to be 1798 Hz and the $^{2}J(^{119}Sn\text{-}^{117}Sn)$ will be of the same order of magnitude, because the ratio of γ for ^{119}Sn to ^{117}Sn is 1.046.[31] The *J*-coupling can be explained in these compounds based on the alternate ways for the spin polarization, e.g., it can be propagated through π-bonds due to the participation of the higher orbitals.

Solid-state $^{119}Sn\{^{1}H\}$ MAS NMR Spectroscopy

Recall that the roofing effect in the triplets observed in the $^{119}Sn\{^{1}H\}$ MAS NMR spectra indicate that the two fluorine atoms are not magnetically equivalent. The two distinctly different dipolar couplings and *J*-anisotropies give rise to slight differences in the sideband intensities of the isotope peaks. Simulations of the $^{119}Sn\{^{1}H\}$ NMR spectra provided the dipolar coupling for the second fluorine nucleus, for which the Sn·····F bond length is not known exactly. The short Sn—F distance is known to be 2.15 Å as determined by X-ray crystallography. The dipolar coupling value obtained here provided an estimate of 2.37(±0.02) Å for the long Sn·····Fdistance, which is very close to the value estimated in the literature.[7] Furthermore, the F—Sn·····F angle was estimated as 165°, which is a new observation. In summary, the structure of Me_3SnF must be considered as if the Sn—F·····Sn and F—Sn·····F groups are bent, with two different bond lengths, and the methyl groups are on average planar undergoing rapid motion. This situation is illustrated in Scheme-V,

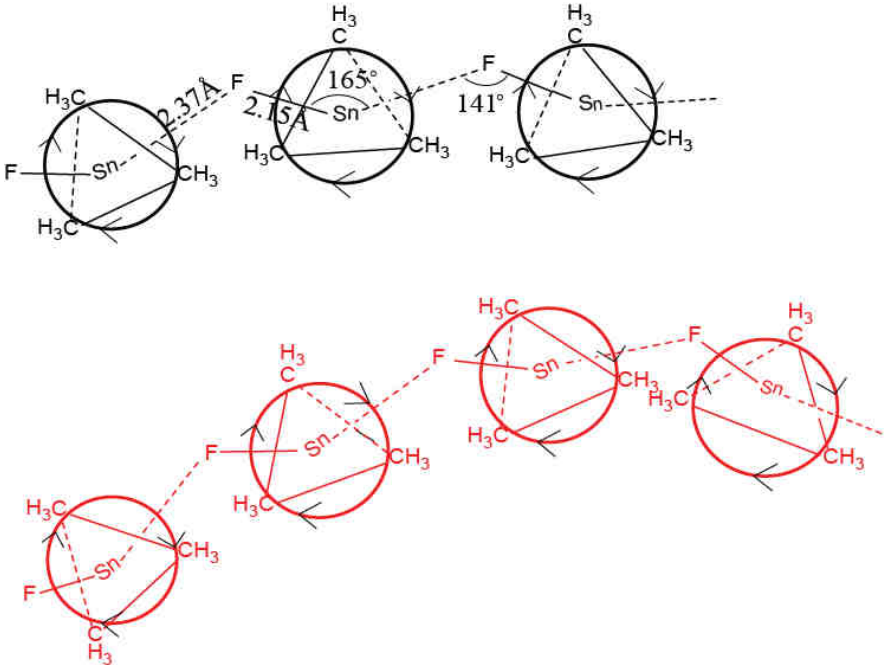

(Scheme-V)

A comparison of the data of the present study with those reported in literature is given in Table 3.6. It is evident that high-resolution NMR spectroscopy is necessary to get the accurate spectral parameters. It may appear that the line width in the $^{119}Sn\{^{1}H\}$ NMR spectrum is broad, however, previous measurements did not employ the double decoupling, hence, their resolution and signal-to-noise ratio may not have been sufficient to appreciate the broad base to the peak structure causing them to underestimate the true line-width.

Table 3.6 Comparison of literature data with the present work data for Me_3SnF

NMR experiment	Literature Data	Experimental Data
^{13}C	δ (^{13}C) = 2.3 ppm ^1J (^{119}Sn -^{13}C) = 550 Hz Line Width=120 Hz	δ (^{13}C) = 2.3 ppm ^1J (^{119}Sn -^{13}C) = 511 .4 Hz Line Width=80 Hz
$^{119}Sn\{^1H\}$	δ (^{119}Sn) = 24.3 ppm ^1J (^{119}Sn -^{19}F) = 1300 Hz Line Width = 110 Hz	δ (^{119}Sn) = 24.3 ppm ^1J (^{119}Sn -^{19}F) = 1320±20 Hz Line Width = 225 Hz
$^{119}Sn\{^1H,^{19}F\}$	----------	δ (^{119}Sn) = 24.3 ppm ^2J (^{119}Sn-^{119}Sn) = 3703 Hz[a] ^2J (^{119}Sn-^{117}Sn) = 3539 Hz Line Width = 461 Hz
$^{19}F\{^1H\}$	----------	δ (^{19}F) = –134.3 ppm ^1J (^{119}Sn-^{19}F) = 1320 Hz Line Width = 287 Hz

[a]calculated

3.5 Conclusion

For the first time, high-resolution simultaneously ^1H- and ^{19}F-decoupled solid-state NMR spectra were obtained for ^{13}C and ^{119}Sn along with single proton-decoupled ^{19}F. The asymmetry of the shielding tensors for tin and fluorine and the inequivalence of the fluorine environments strongly support a structure to Me_3SnF that is bent at both Sn and F, as well as one Sn–F bond length is longer than the second. Spectral simulations showed the dependence of the ^{119}Sn NMR signal on the orientations and dipolar couplings of the two fluorine atoms about Sn, which ultimately provided the information about the non-linearity of F—Sn·····F angle (Table 3.5). The simulation of the dipolar coupling gave the best estimation for the long Sn·····F distance as 2.37(±0.02) Å. The ^2J(^{119}Sn-^{117}Sn) coupling constant was observed for the first time for Me_3SnF which is

consistent with the polymeric structure of Me_3SnF. In addition, the two $^{119}Sn\{^1H,^{19}F\}$ and $^{19}F\{^1H\}$ NMR experiments are novel.

In the present work, the model for Me_3SnF based on one-dimensional NMR spectroscopy was obtained (Scheme-V). A series of very slow spinning (500 Hz to 2 kHz) $^{119}Sn\{^1H\}$ NMR spectra should offer the best chance to get more accurate *J*–anisotropies for the two fluorine environments, because at very slow spinning speed the effect of *J*–anisotropies should be more pronounced and should remove any uncertainty in the tensor measurements. With the help of REDOR experiments,[32] the dipolar couplings may be best observed by the application of some specialized homonuclear dipolar coupling sequences under fast magic angle spinning condition. A two-dimensional heteronuclear spin-echo double-resonance (SEDOR)[33] correlation experiment represents the best opportunity to observe the relative tensor orientations of the principal axis of the Sn and F tensors, which ultimately leads to the determination of the β–angle (F—Sn· · · · · F angle).[26] Also, Double-Quantum-Filtered (DQF)[34,35] experiments can verify the $^2J(^{119}Sn\text{-}^{119}Sn)$ and $^2J(^{119}Sn\text{-}^{117}Sn)$ coupling constants based on the antiphase modulations for the *J*-couplings. A series of $^{117}Sn\{^1H,^{19}F\}$ NMR spectra may also be recorded to verify the $^2J(^{119}Sn\text{-}^{117}Sn)$ couplings.

Also, an attempt can be made to grow better quality crystals of Me_3SnF and try to record new X-ray data. Because of the advancements in technology, it may be possible to collect better quality data in comparison to the previous X-ray studies.

References:

1. a) (i) Herzog, A.; Liu, FQ; Roesky, H. W.; Demsar, A.; Keller, K.; Noltemeyer, M.; Pauer, F. *Organometallics* **1994**, *13*, 1251. (ii) Roesky, H. W.; Keller, K. *J. Fluorine Chem.* **1998**, *89*, 3. (iii) Edelson, B.S.; Stoltz, B.M. and Corey, E.J. *Tetrahedron Lett.* **1999**, *40*, 6729 b) Krause, E. *Ber. Dtsch. Chem. Ges*. **1918**, *51*, 1447.
2. Bai, H.; Harris, R. K. *J. Magn. Reson*. **1992**, *96*, 24.
3. Dakternieks, D.; Zhu, H. *Inorg. Chim. Acta*. **1992**, *196*, 19.
4. (i) Clark, H. C.; O'Brien, R. J.; Trotter, J. *J. Chem. Soc*. **1964**, 2332. (ii) Clark, H.C.; O'Brien, R.J.; Trotter, J. *Proc. Chem. Soc.* **1964**, 85.
5. Davis, A. G. *Organotin Chemistry,* 2nd Edition; WILEY-VCH Verlag GmbH & Co. KGaA: Weinheim, 2003.
6. Savall, B. M.; Powell, N. A.; Roush, W. R. *Org. Lett.* **2001**, *3*, 3057.
7. Yasuda, K.; Kawasaki, Y.; Kasai, N.; Tanaka, T. *Bull. Chem. Soc. Jpn.* **1965**, *38*, 1216.
8. Okawara, R.; Webster, D. E.; Rochow, E. *J. Am. Chem. Soc.* **1960**, *82*, 3287.
9. Harris, R. K.; Packer, K. J.; Reams P. *Chem. Phy. Lett.* **1985**, *115*, 16.
10. Harris, R.K.; Sebald, A. *Magn. Reson. Chem.* **1989**, *27*, 81.
11. Harris, R.K.; Sebald, A. *Magn. Reson. Chem.* **1987**, *25*, 1058.
12. Harris, R.K.; Lawrence, S.E.; Oh, S.W. *J. Mol. Struct.* **1995**, *347*, 309.
13. Bak, M.; Rasmussen, J. T.; Nielsen, N. C. *J. Magn. Reson.* **2000**, *147*, 296.
14. Bai, H.; Harris, R. K.; Reuter H. *J. Organomet. Chem*. **1991**, *408*, 167.
15. David, L. B.; Wasylishen, R. E. *J. Biomol. NMR* **2003**, *25*, 73.

16. Power, W. P.; Lumsden, M. D.; Wasylishen, R. E. *J. Am. Chem. Soc.* **1991**, *113*, 8257.
17. Power, W. P.; Wasylishen, R. E. *Inorg. Chem.* **1992**, *31*, 2137.
18. Ulrich, S. E.; Dunell, B. A. *J. Chem. Soc. (Faraday Trans.)* **1972**, 68, 680.
19. Bondi, A. *J. Phys. Chem.*, **1964**, *68*, 441.
20. Lockhart, T. P.; Manders, W. F. *J. Am. Chem. Soc.* **1985**, *107*, 5863.
21. Casella, G.; Ferrante, F.; Saielli, G. *Inorg. Chem.* **2008**, *47*, 4796.
22. Lockhart, T. P.; Manders, W. F. *J. Am. Chem. Soc.* **1987**, *109*, 7015.
23. Harris, R. K.; Packer, K. J.; Reams P. *J. Mol. Struct.* **1986**, *141*, 13.
24. Dakternieks, D.; Zhu, H. *Inorg. Chim. Acta.* **1992**, *196*, 19.
25. Beckmann, J; Horn, D.; Jurkschat, K.; Rosche, F; Schürmann, M; Zachwieja, U; Dakternieks, D; Duthie, A; Lim, A. E. K. *Eur. J. Inorg. Chem.* **2003**, *1*, 164.
26. Heuer, L.; Ernst, L.; Schmutzler, R.; Schomburg, D. *Angew. Chem. Int. Ed. Engl.* **1989**, *28*, 1507.
27. Bennett, A. E.; Rienstra, C. M.; Auger, M.; Lakshmi, K. V.; Griffin, R. G. *J. Chem. Phys.* **1995**, *103*, 6951.
28. Mehring, M. *Principles of High Resolution NMR in Solids*, Springer-Verlag, New York, 1983.
29. Smith, S. A.; Palke, W. E.; Gerig, J. T. *Concepts Magn. Reson.* **1992**, *4*, 107.
30. Harris, R. K.; Mitchell, T. N.; Nesbitt, G. J. *Magn. Reson. Chem.* **1985**, *23*, 12, 1080.
31. Gielen, M.; Willem, R.; Wrackmeyer, B. *Physical Organomettalic Chemistry* Volume 3; John Wiley & Sons Ltd.: Oxford, 2002.

32. Gullion, T.; Schaefer, J. *J. Magn. Reson.* **1989**, *81*, 196.

33. Bechmann, M; Helluy, X; Marichal, C.; Sebald, A. *Solid State Nucl. Magn. Reson.* **2002**, *21*, 71.

34. Gullion, T. *Con. Magn. Reson.* **1998**, *10*, 277.

35. Levitt, M. H.; Titman, J. J.; Gregory, D. H.; Duma, L.; Emsley, L.; Brown, S. P. *J. Chem. Phys.* **2005**, *122*, 194313.

Chapter-4

4. Adducts of SF_4 with Nitrogen-Containing Bases

4.1 Introduction

Sulfur tetrafluoride can act as a weak Lewis acid as demonstrated by its fluoride-ion acceptor properties towards CsF and $[N(CH_3)_4]F$.[1] Sulfur tetrafluoride reacts with nitrogen bases that have at least one hydrogen bonded to nitrogen upon HF elimination.[2,3] For example, NH_3 reacts with SF_4 yielding S_4N_4. The reaction of SF_4 with nitrogen bases that do not have hydrogen bonded to nitrogen have been investigated only in a few studies. In one of the publication in 1960 it was said that pyridine and triethylamine form a 1:1 adduct with SF_4 to give $SF_4 \cdot py$ and $SF_4 \cdot NEt_3$ adduct and it was said that the result was based on a "crude tensometric" study.[4] Four types of adducts between SF_4 and pyridine were suggested based on elemental analysis, i.e., $SF_4 \cdot py$, $SF_4 \cdot 2py$, $SF_4 \cdot 4py$, and $SF_4 \cdot 8py$.[5] Matrix-isolation infrared spectroscopy provided additional evidence for the 1:1 adduct between SF_4 and pyridine.[6] However, significant signal overlap resulted in rather inconclusive results for the $SF_4 \cdot py$ adduct. These findings found their way into inorganic chemistry textbooks,[7] although unambiguous characterization is still missing.

The significance of these types of reactions is that the study of these complexes can provide information about reaction pathways and the exact nature of the nitrogen to sulfur coordinate bond.[6]

The goal of this study is to investigate the reaction of SF_4 with a variety of nitrogen bases such as pyridine, lutidine, 4–picoline, triethylamine, quinoline, isoquinoline, 4,4'–bipyridine, 2,2'–bipyridine and study them by Raman and NMR spectroscopy.

4.2 Results and Discussion

4.2.1 Synthesis and Stability of SF_4 Adducts

Pyridine was allowed to react with excess SF_4 at –80°C. Removal of excess SF_4 under dynamic vacuum at –60°C yielded a white solid (Eq. 4.1). The solid was stable under dynamic vacuum below –42°C. The product was studied by low-temperature Raman spectroscopy. When the adduct was warmed up to –38°C to remove SF_4 under dynamic vacuum, pyridine was recovered.

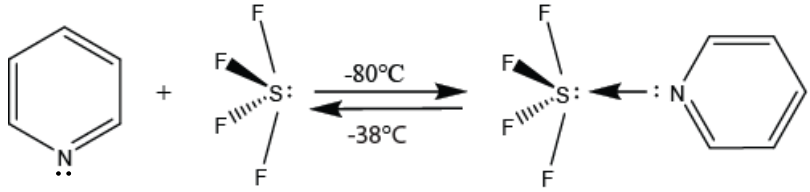

(4.1)

The SF_4·pyridine adduct formation mentioned in Eq. 4.1 was also verified by low-temperature solution-state ^{19}F, ^{1}H, and ^{13}C NMR spectroscopy.

Lutidine was reacted with excess sulfur tetrafluoride at –80°C. The reactor was agitated to allow for proper mixing. The product was studied by low-temperature Raman spectroscopy which indicated the formation of a new compound (Eq. 4.2). When the adduct was warmed up to –38°C under dynamic vacuum to remove SF_4, lutidine was recovered with traces of HF_2^-.

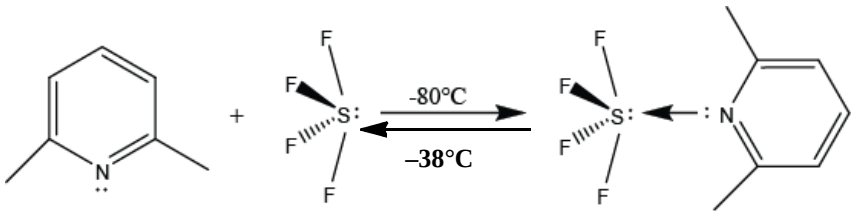

(4.2)

Similarly, 4–picoline and triethylamine were reacted with excess sulfur tetrafluoride at –80°C (Eq. 4.3 and Eq. 4.4, respectively). The reactors were agitated for

proper mixing. The products were studied by low-temperature Raman spectroscopy which indicated the product formation in the similar way as indicated above. When the adduct was warmed up to –35°C to remove SF_4, 4–picoline and triethylamine were recovered with traces of HF_2^-.

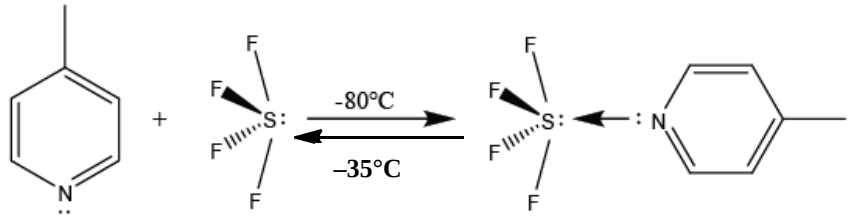

(4.3)

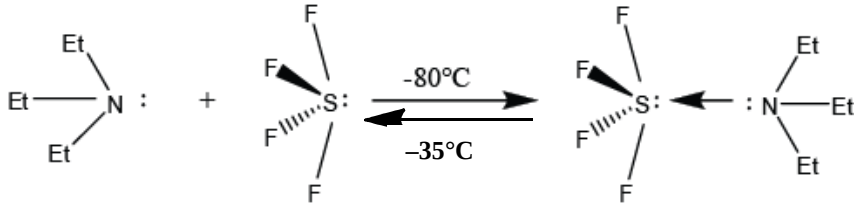

(4.4)

A reaction took place in case of SF_4 and 4,4'–bipyridine but the exact nature of the product is not known so far. The reaction was verified with low-temperature Raman spectroscopy which gave rise to a set of signals that cannot be attributed to the reactants. Surprisingly, the product was stable upon warming to ambient temperature even under dynamic vacuum. The mass balance of this reaction suggests an approximate 1:1 stoichiometry.

The reactions of SF_4 with quinoline (Eq. 4.5), isoquinoline (Eq. 4.6), and 2,2'–bipyridine (Eq. 4.7) were studied at low-temperature. Surprisingly, no adduct formation took place in case of quinoline, isoquinoline, and 2,2'–bipyridine as shown by the Raman

spectra, which contained only signals attributed to the reactants at –80°C. Apparently, the donor strength for quinoline and isoquinoline are not sufficiently large for adduct formation with the weak Lewis acid SF_4. A reason for the failure to produce an adduct with 2,2'–bipyridine could be given with the steric effect, not allowing the bidentate 2,2'–bipyridine ligand to coordinate to sulfur in SF_4.

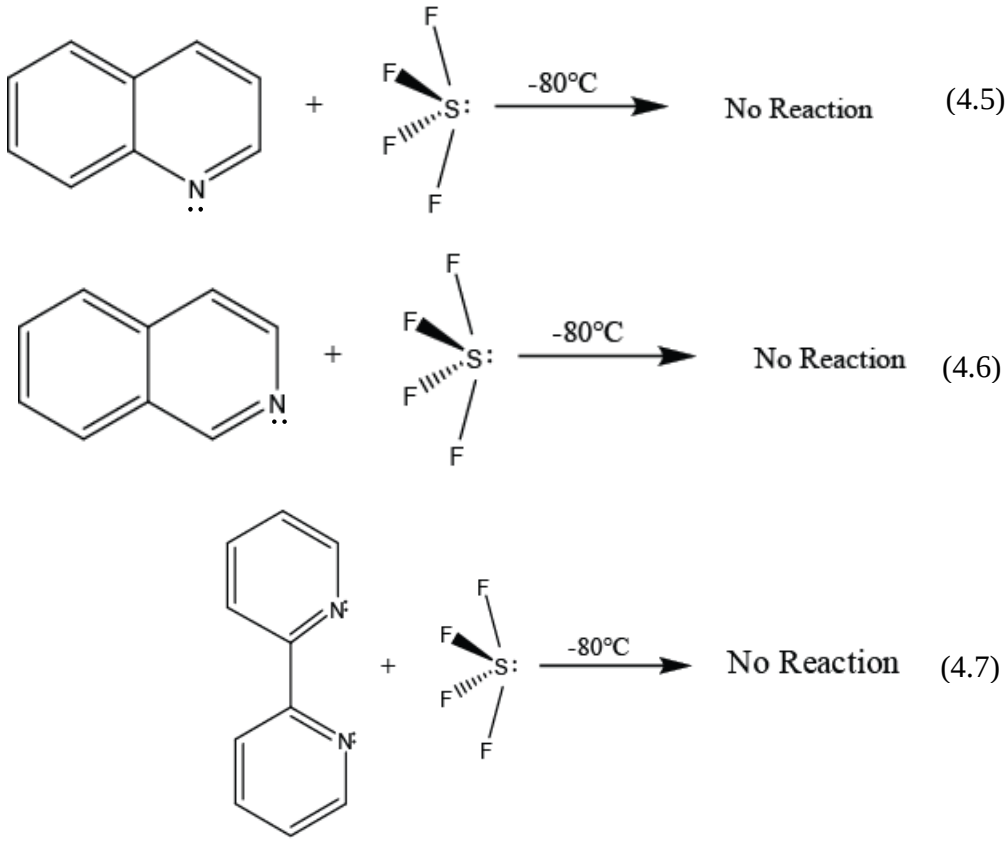

4.2.2 Raman Spectroscopy of SF_4 adducts

SF_4·Pyridine Adduct

The Raman spectra of SF_4, pyridine, and SF_4·pyridine were recorded at –110° C. The Raman spectra are depicted in Fig. 4.2.1 and the vibrational frequencies are listed in

Table 4.1. In the Raman spectrum of liquid SF_4 at –110°C, two broad intense bands were observed at 896 cm^{-1} and 536 cm^{-1} which can be assigned to the symmetric equatorial and axial SF_2 stretching, respectively.[8] The weaker band at 857 cm^{-1} can be attributed to the asymmetric stretch of the equatorial SF_2 group. The broad band at 536 cm^{-1} overlaps with the symmetric combination of the equatorial and axial SF_2 scissoring vibrations. In general the observed Raman spectrum is in excellent agreement with that observed in the literature.[9] The Raman spectrum of the SF_4·pyridine adduct contains bands that can be attributed to the pyridine moiety in the adduct and also sharp bands that are assigned to vibrations of the SF_4 group. Several Raman signals associated with the pyridine part of the adduct are significantly shifted compared to those of neat pyridine. The stretching frequencies of the C–H vibrations of pyridine upon complex formation are shifted, e.g., the signal at 3055 cm^{-1} in free pyridine is shifted to 3068 cm^{-1}. A similar shift of this CH strechting frequency has been observed for 1:1 adduct of pyridine with trifluoroacetic anhydride.[10] Upon complexation of pyridine with trifluoroacetic anhydride, a shift of the C–C stretching mode at 1580 to 1630 cm^{-1} has been observed.[10] A similar shift from 1581 to 1622 cm^{-1} was observed in the current study for the SF_4·pyridine adduct. The most intense band in the Raman spectrum of neat pyridine is at 990 cm^{-1}, which corresponds to the symmetric C_5N ring stretch. This band is shifted to 1003 cm^{-1} in the SF_4·pyridine adduct, compared to 1024 cm^{-1} for the pyridine-trifluoroacetic anhydride adduct.[10] These shifts provide clear evidence for the complexation of pyridine. Since the frequency shifts are smaller than for other adducts, a weaker Lewis acid/base interaction is found in the SF_4·pyridine adduct, reflecting the weak Lewis acidity of SF_4.

In contrast to the Raman spectrum of neat SF_4, relatively sharp signals are observed in the S–F stretching region. The symmetric and asymmetric stretching S–F frequencies for equatorial position are shifted from 896 and 857 cm^{-1} in neat SF_4 to 852 and 776 cm^{-1} in the adduct, respectively. The stretching for axial S–F has been shifted from 536 cm^{-1} to 513 cm^{-1}. These observations also support the formation of a complex between SF_4 and pyridine. The shift of the S–F stretching bands to lower frequencies reflects the weaker S–F bonds in the adduct compared to free SF_4.

The mass balance for the reaction of SF_4 with pyridine suggests the formation of a 1:1 adduct. When the mixture was allowed to warm up to –38°C under dynamic vacuum, the adduct dissociates and pyridine was recovered giving the same bands in the Raman spectrum as were present in the original spectrum of pyridine.

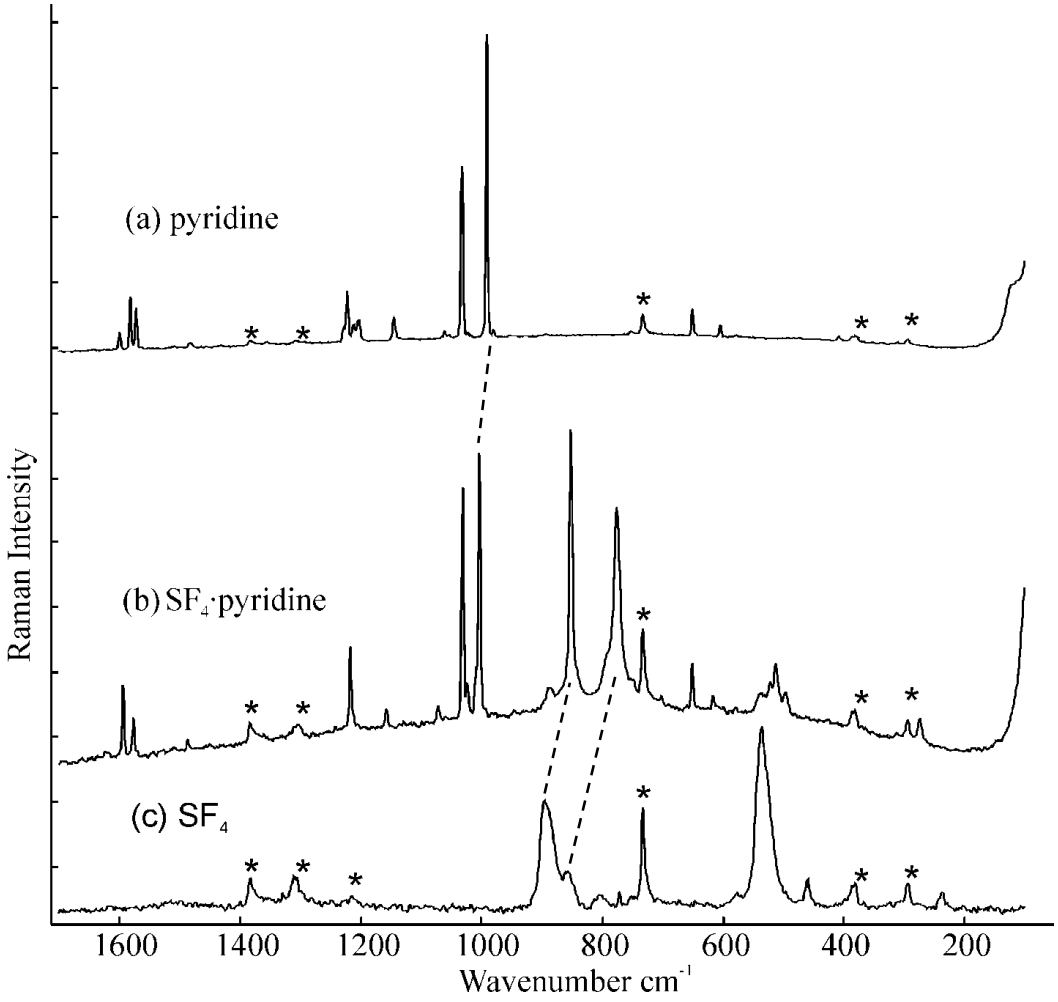

Figure 4.2.1 Raman spectra of (a) pyridine, (b) the SF_4·pyridine adduct, and (c) SF_4 at –110°C. Asterisks (*) denote bands arising from the FEP sample tube.

Table 4.1 Raman frequencies (relative intensities), cm^{-1} of SF_4, pyridine and SF_4·pyridine at –110°C together with their tentative assignments.

vibrational frequencies			assignments		
pyridine[a]	SF_4[b]	SF_4·pyridine[c]	pyridine[d]	SF_4[e]	SF_4·pyridine
3173(1)		3180(1)			
3156(1)		3153(3)			
3143(3)		3143(1)			
3088(5)		3092(8)			
3070(2)		3077(21)			
3060(sh)		3068(48)	ν(C-H)		ν(C-H)
3055(39)		3058(sh)			
3033(5)		3044(7)			
3020(5)		3030(6)			
		3001(2)			
2987(2)		2987(1)	overtones		overtones and
2954(2)		2962(5)	and		combination bands
2917(1)		2926(2)	combination		
			bands		
		1622(2)			
1599(5)		1593(29)	ν(C-C)		ν(C-C)
1581(9)		1581(7)			
1571(7)		1576(15)	.		
		1514(2)			
1481(3)		1486(5)	ν(C-N)		ν(C-N)
		1448(2)			
1383(1)		1383(11)			
		1242(2)			
1228(3)		1230(1)			
1222(18)		1222(sh)			
		1217(33)[f]			
1211(2)		1212(sh)			
1203(5)		1203(5)	δ(C-H)		δ(C-H)
		1157(7)			
1145(2)		1145(3)			
		1072(5)			
1060(2)		1068(4)			
		1031(100)	in-plane		in-plane ring-def
1031(75)		1023(22)	ring-def		
		1009(16)			
990(100)		1003(96)	$\nu_s(C_5N$ ring)		$\nu_s(C_5N$ ring)
980(1)		991(37)			
	896(65)	852(95)		$\nu_s(SF_{2,eq})$	ν(S-F)
	857(32)	776(76)		$\nu_{as}(SF_{2,eq})$	ν(S-F)
		749(10)			
		702(3)			out-of-plane C-H def.
650(5)		651(17)			
		617(6)	in-plane		in-plane ring-def
			ring-def		
604(3)		605(3)			
578(1)		578(3)			

	536(100)	522(6) 513(18)	}	$\nu_s(SF_{2,\,ax})$ $\delta_{sciss}(SF_{2,ax})+$ $\delta_{sciss}(SF_{2,eq})$	$\nu_s(SF_{2,ax})$ $\delta_{sciss}(SF_{2,ax})+$ $\delta_{sciss}(SF_{2,eq})$
	461(10)	497(9)		$SF_{2,eq}$ wagging	$SF_{2,eq}$ wagging
408(1) 381(2) 313(1) 294(1)		426(2) 412(2) 382(8)[f] 311(2)	} out-of-plane ring def		out-of-plane ring def
	237(8)	274(11)		$\delta_{sciss}(SF_{2,ax})-$ $\delta_{sciss}(SF_{2,eq})$	$\delta_{sciss}(SF_{2,ax})-$ $\delta_{sciss}(SF_{2,eq})$

[a] The Raman spectrum was recorded in a ¼–in FEP tube at –110°C. Signals from the FEP sample tube were observed at 294(2), 385(3), 733(11), 1306(1), 1382(2) cm^{-1}. [b] The Raman spectrum was recorded in a ¼–in FEP tube at -110°C. Signals from the FEP sample tube were observed at 294(8), 385(12), 733(53), 1216(5), 1306(16), 1382(19) cm^{-1}. Bands at 1382(19), 804(9), 772(11) cm^{-1} were observed for ν(S–O) SOF_2, ν(S–F) SOF_2 and ν(S–F) SF_6 respectively. [c] The Raman spectrum was recorded in a ¼–in FEP tube at –110°C. Signals from the FEP sample tube were observed at 294(6), 385(8), 733(35), 1216(2), 1306(5), 1382(9) cm^{-1}. [d] Pyridine bands have been assigned based on references 11-15. [e] Sulfur tetrafluoride bands have been assigned based on references 8,9. [f] Overlap with FEP band.

Two isomers are possible for the SF_4·pyridine adduct (Figure 4.2); one isomer with a nearly square planar SF_4 geometry and one with retention of the SF_4 seesaw geometry. Based on the Raman spectroscopic data, isomer (a) with the approximate SF_4 seesaw geometry is expected to be the prepared adduct. The SF_4 Raman frequencies are shifted, but the relative intensities are generally maintained. A square planar SF_4 moiety would give rise to completely different relative intensities of the SF_4 stretching bands in the Raman spectrum due to a complete change of local symmetry. Computational work done by Hélène P. A. Mercier at McMaster University[16] found that the two isomers (a) and (b) are minima on the potential energy surface. The DFT calculation based on B3LYP/cc-pVTZ basis set showed that the isomer (a) is more stable than isomer (b) by 61.4 $kJmol^{-1}$ supporting our assignment. Interestingly, the calculated distance between sulfur and nitrogen is 2.573 Å in the more stable isomer (a) as compared to 1.971 Å in

isomer (b). The S–N bond length in the more stable isomer is still significantly shorter than the sum of the van der Waal's radii of sulfur and nitrogen atom (3.35Å).[17]

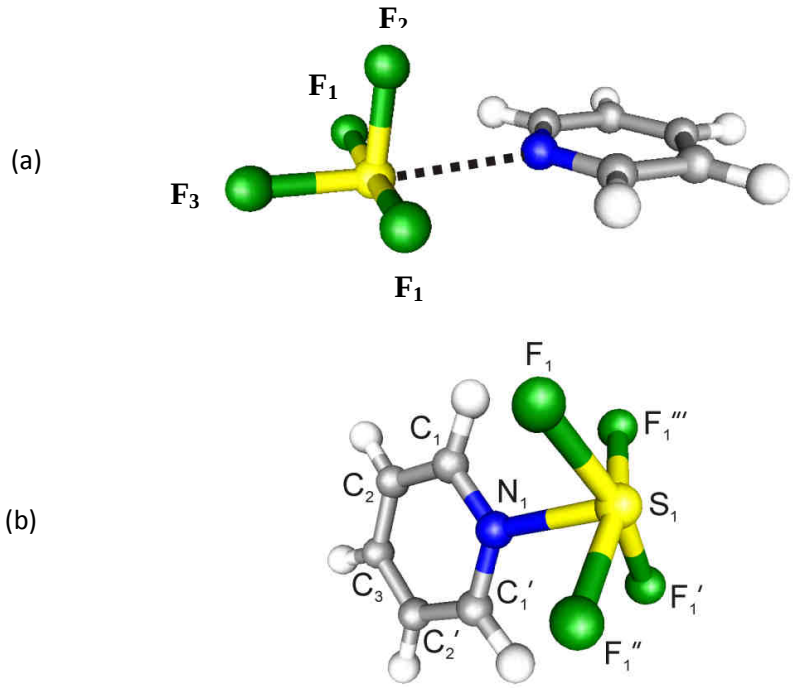

Figure 4.2 Structures of two possible isomers isomer(a) and isomer(b) used for DFT calculation of SF_4 with pyridine adduct.[9]

SF_4·Lutidine Adduct

Raman spectra of SF_4, lutidine, and SF_4·lutidine at –110°C were recorded and are depicted in Fig. 4.2.2. The vibrational frequencies and tentative assignments are listed in Table 4.2. In the Raman spectrum of the SF_4·lutidine adduct three bands in the equatorial SF_2 stretching region were observed at 810, 820, and 861 cm^{-1}. Only two S–F bands are expected in this region, however, vibrational coupling of molecules in a unit cell may explain the appearance of the two bands at 810 and 820 cm^{-1}. The symmetric stretching

for the axial SF_2 moiety is shifted from 536 cm^{-1} in free SF_4 to 522 cm^{-1} in the adduct. These frequencies are in general agreement with those found for the pyridine adduct. The Raman spectra of the lutidine adduct shows vibrational bands attributed to the lutidine group. In comparison with the Raman spectrum of free lutidine, many vibrational bands are shifted and the number of observed bands is increased. The latter is a result of the lowering in symmetry upon adduct formation. Shifts are observed for the C–H stretching frequencies with the signal at 3050 being shifted to 3081 cm^{-1} upon adduct formation. In the literature, a C–C stretching band in the infrared spectrum of a lutidine adduct with the Lewis acidic surface of $AlF_{2.6}(OH)_{0.4}$ at 1610 cm^{-1} was found to be characteristic for a Lewis acid/base adduct.[15] The observation of a Raman band at 1602 cm^{-1} for the SF_4 adduct suggests a weaker Lewis acid-base interaction. Similar to the pyridine adduct, the symmetric C_5N ring stretch has been shifted from 997 for free lutidine to 1009 cm^{-1} for the adduct. These facts indicate the formation of an adduct between SF_4 and lutidine. Also the mass balance of this reaction indicates a 1:1 stoichiometry between SF_4 and lutidine. When the mixture was warmed up to –38°C under dynamic vacuum to remove SF_4, the adduct dissociates and lutidine was recovered with HF_2^- as an impurity (560 cm^{-1} and 1022 cm^{-1}). The impurity peaks are in agreement with the literature data for HF_2^-.[18]

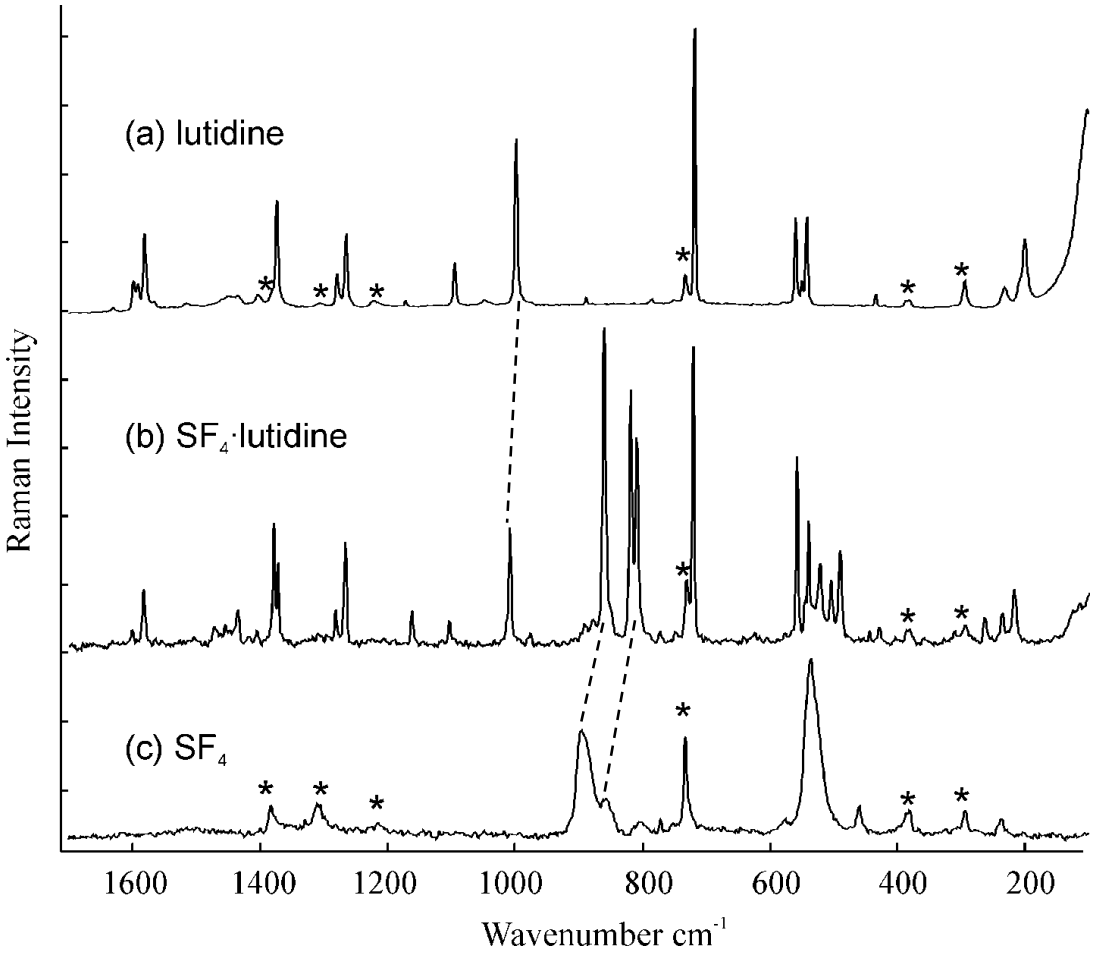

Figure 4.2.2 Raman Spectrum of (a) lutidine, (b) SF_4·lutidine adduct, and (c) SF_4 at –110°C. Asterisks (*) denote bands arising from the FEP sample tube.

Table 4.2 Raman frequencies (relative intensities), cm^{-1} of SF_4, lutidine, and SF_4·lutidine adduct at –110°C

lutidine[a]	SF_4[b]	lutidine·SF_4[c]	assignments		
			lutidine[d]	SF_4[e]	lutidine·SF_4
3160(1)		3159(2)			
		3081(29)			
3075(20)		3073(sh)			
		3061(4)	ν(C-H)		ν(C-H)
3050(11)		3054(4)	(aromatic ring)		(aromatic ring)
		3046(4)			
3027(19)		3028(6)			
2999(17)		2991(24)			
		2982(5)	ν(C-H)		ν(C-H)
2956(17)		2961(4)	(CH_3)		(CH_3)
		2938(50)			
2918(52)		2926(16)			
2854(6)		2861(2)	overtones and		overtones and
2726(8)		2733(2)	combination bands		combination bands
1597(11)		1602(4)			
1590(9)					
1580(28)		1583(26)	ν(C-C) + δ(C-H)		ν(C-C) + δ(C-H)
1565(1)		1565(1)			
		1472(8)			
		1461(4)	ν(C-N)		ν(C-N)
		1455(8)			
1449(2)		1448(5)			
1435(1)		1436(14)			
		1419(1)			
1402(4)		1406(4)	δ(CH_3)		δ(CH_3)
		1379(41)[f]			
1373(40)		1372(31)			
		1310(1)			
1278(13)		1282(24)	in-plane		in-plane
1264(28)		1267(33)	δ(C-H)		δ(C-H)
1221(2)					
1172(2)		1162(21)	in-plane		
1094(17)		1104(6)	ring-deform.		
1047(2)					
997(62)		1009(43)	$\nu_s(C_5N$ ring)		$\nu_s(C_5N$ ring)
		976(3)			
888(2)					
	896(65)	861(100)		$\nu_s(SF_{2,eq})$	ν(S-F)
	857(32)	820(66)		$\nu_{as}(SF_{2,eq})$	ν(S-F)
		810(70)			
786(2)					
			out-of plane		out-of-plane
718(100)		721(95)	C-H deform.		C-H deform.
559(36)		559(68)	in-plane ring		in-plane ring
550(28)		541(56)	deform.		deform.

542(36)					
	536(100)	522(43) 505(35)	}	$\nu_s(SF_2)_{ax}$ $\delta_{sciss}(SF_{2,ax})$+ $\delta_{sciss}(SF_{2,eq})$	$\nu_s(SF_2)_{ax}$ $\delta_{sciss}(SF_{2,ax})$ + $\delta_{sciss}(SF_{2,eq})$
	461(10)	491(48)		$SF_{2,eq}$ wagging	$SF_{2,eq}$ wagging
434(6)		445(2) 430(2) 312(1)			
294(12)[f]		295(10)[f]	in-plane ring deform.		in-plane ring deform.
	237(6)	266(3)		$\delta_{sciss}(SF_{2,ax})$ $-\delta_{sciss}(SF_{2,eq})$	$\delta_{sciss}(SF_{2,ax})$ – $\delta_{sciss}(SF_{2,eq})$
232(6)					
200(27)		218(19)	out-of-plane ring deform.		out-of-plane ring deform.

[a] The Raman spectrum was recorded in a ¼–in FEP tube at –110°C. Signals from the FEP sample tube were observed at 294(10), 385(6), 733(24), 1306(1), 1382(2) cm^{-1}. [b] The Raman spectrum was recorded in a ¼–in FEP tube at -110°C. Signals from the FEP sample tube were observed at 294(8), 385(12), 733(53), 1216(2), 1306(1), 1382(2) cm^{-1}. Bands at 1382(19), 804(9), 772(11) cm^{-1} were observed for ν(S–O) SOF_2, ν(S–F) SOF_2 and ν(S–F) SF_6 respectively. [c] The Raman spectrum was recorded in a ¼–in FEP tube at –110°C. Signals from the FEP sample tube were observed at 294(6), 385(5), 733(24), 1216(1), 1306(1), 1379(41) cm^{-1}. [d] The bands for lutidine have been assigned based on references 19. [e] Sulfur tetrafluoride bands have been assigned based on references 8,9. [f] Overlap with FEP band.

SF_4·4-Picoline Adduct

The Raman spectra of SF_4, 4-picoline and SF_4·4-picoline were recorded at –110°C (Fig 4.2.3). The vibrational frequencies and their tentative assignments are listed in Table 4.3. In the Raman of SF_4·4-picoline adduct S-F stretching bands were observed at 841 and 821 cm^{-1}.[1] The symmetric stretching band for axial SF_2 unit is shifted from 536 cm^{-1} to 530 cm^{-1}. Several peaks from neat 4-picoline have also been shifted upon formation of the SF_4·4-picoline adduct. The aromatic C–H stretching frequencies for 4-picoline appear above 3000 cm^{-1} as expected, while the aliphatic C–H stretching frequencies for CH_3 group appear in the region from 2908 to 2992 cm^{-1}. The stretching

frequencies of the C–H vibrations of 4-picoline are shifted upon complex formation, e.g., the signal at 3049 cm^{-1} has been shifted to 3065 cm^{-1}. The C–C stretch at 1608 has been shifted to 1612 cm^{-1}. The symmetric stretch in the 4-picoline for the C_5N ring has been shifted from 998 to 1008 cm^{-1}. These observations support the formation of an adduct between SF_4 and 4-picoline. The mass balance of the reaction indicates a 1:1 stoichiometry between SF_4 and 4-picoline. When the adduct was warmed up to -35°C under dynamic vacuum to remove SF_4, the adduct dissociated and 4-picoline was recovered with HF_2^- as an impurity (560 and 1022 cm^{-1}).

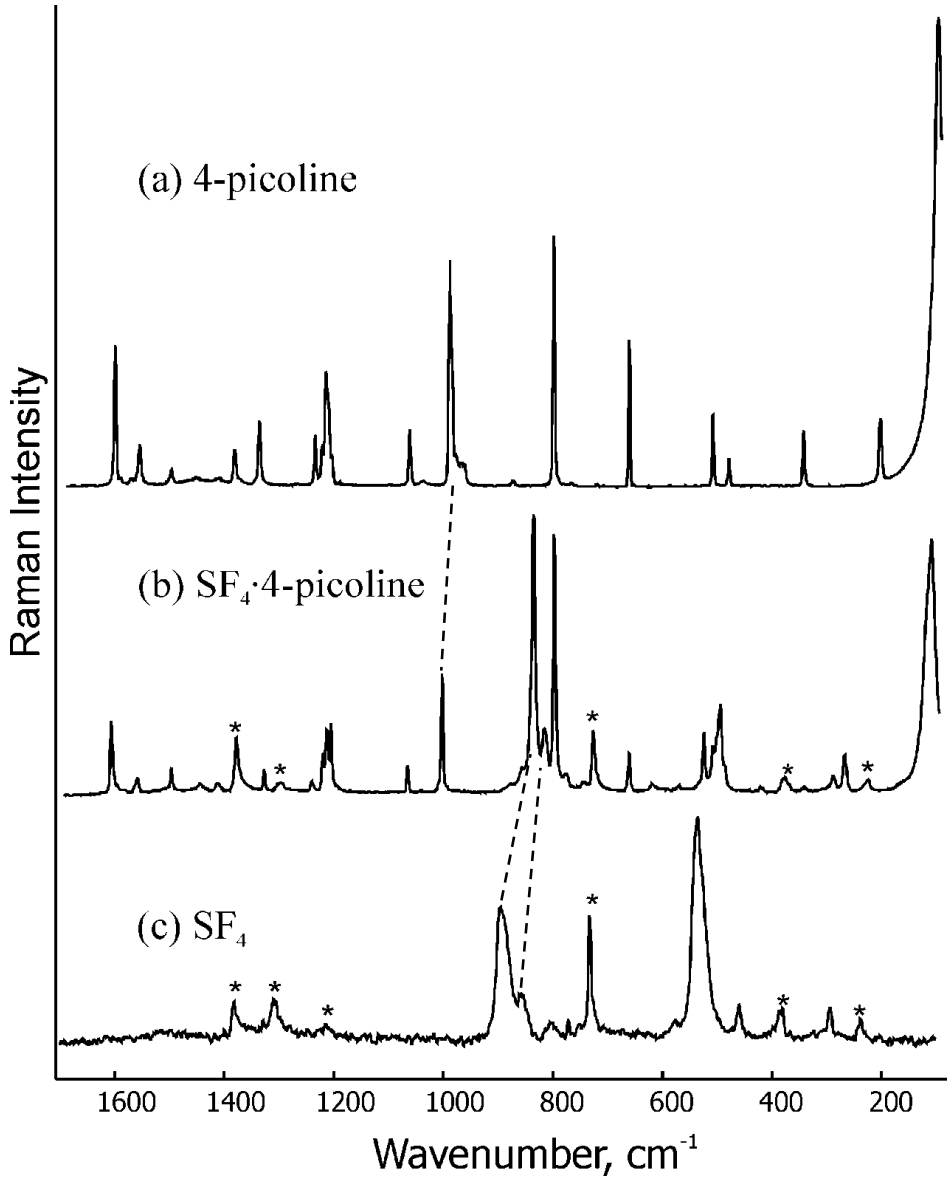

Figure 4.2.3 Raman spectrum of SF_4, 4-picoline, and SF_4·4-picoline adduct at –110°C. Asterisks (*) denote bands arising from the FEP sample tube.

Table 4.3 Raman frequencies (relative intensities), cm^{-1} of SF_4, 4-picoline and SF_4·4-picoline adduct at –110°C

4–picoline[a]	SF_4[b]	4–picoline·SF_4[c]	assignments		
			4-picoline[d]	SF_4[e]	4-picoline·SF_4
		3065(44)			
3049(93)		3045(14)	ν(C-H)		ν(C-H)
3033(38)		3034(7)	(aromatics)		(aromatics)
		3003(3)			
2992(17)		2993(19)	ν(C-H)		ν(C-H)
2965(12)		2964(7)	(CH_3)		(CH_3)
2922(49)		2929(28)			
2908(sh)		2905(2)			
2861(12)		2893(2)			
2819(5)		2874(2)	overtones and		overtones and
2739(10)		2737(9)	combination		combination bands
2462(12)		2493(2)	bands		
1608(53)		1612(27)			
1599(2)		1602(3)			
1579(2)			ν(C-C)		ν(C-C)
1563(15)		1566(5)			
1505(5)		1503(18)			
1460(3)		1451(5)	ν(C-N)		ν(C-N)
1419(3)		1419(5)			
1390(15)					
1382(sh)		1384(20)[f]			
1345(24)		1333(18)			
		1306(5)			
1243(22)		1275(11)			
			in-plane		in-plane
		1246(6)	δ(C-H)		δ(C-H)
1231(16)		1227(16)			
1224(49)		1220(28)			
1213(15)		1211(29)			
1071(24)		1072(12)	in-plane		in-plane
1046(3)			ring def		ring def
998(91)		1008(44)	$\nu_s(C_5N$ ring)		$\nu_s(C_5N$ ring)
987(15)					
977(10)					
971(9)					
883(3)					
	896(65)	841(100)		$\nu_s(SF_{2eq})$	ν(S-F)
	857(32)	821(29)		$\nu_{as}(SF_{2eq})$	ν(S-F)
808(100)		804(93)	ν(C-Me)		ν(C-Me)
774(2)		783(12)			
731(1)		726(sh)[f]			
671(56)		667(16)	out-of-plane		out-of-plane
		625(4)	C-H deform.		C-H deform.
		578(3)			

	536(100)	530(22) 514(18)	}	$\nu_s(SF_2)_{ax}$ $\delta_{sciss}(SF_{2,ax})$ + $\delta_{sciss}(SF_{2,eq})$	$\nu_s(SF_2)_{ax}$ $\delta_{sciss}(SF_{2,ax})$ + $\delta_{sciss}(SF_{2,eq})$
518(28)		507(sh)			
489(10)		501(31)			
	461(10)	428(5)		$SF_{2(eq)}$ wagging	$SF_{2(eq)}$ wagging
352(24)		348(3)	out-of-plane ring-deform.		out-of-plane ring-deform.
	237(6)	274(16)		$\delta_{sciss}(SF_{2,ax})$– $\delta_{sciss}(SF_{2,eq})$	$\delta_{sciss}(SF_{2,ax})$– $\delta_{sciss}(SF_{2,eq})$
212(26)		233(5)			

[a] The Raman spectrum was recorded in glass NMR tube at –110°C. [b] The Raman spectrum was recorded in a ¼-in FEP tube at –110°C. Signals from the FEP sample tube were observed at 294(8), 385(12), 733(53), 1216(2), 1306(1), 1382(2) cm^{-1}. Bands at 1382(19), 804(9), 772(11) cm^{-1} were observed for ν(S-O) SOF_2, ν(S-F) SOF_2 and ν(S-F) SF_6 respectively. [c] The Raman spectrum was recorded in a ¼-in FEP tube at -110°C. Signals from the FEP sample tube were observed at 294(6), 386(6), 733(20), 1306(1), 1382(3) cm^{-1}. [d] 4–picoline bands have been assigned based on references 20-21. [e] Sulfur tetrafluoride bands have been assigned based on references 8,9. [f] Overlap with FEP band.

SF_4·Triethylamine Adduct

The Raman spectra of SF_4, triethylamine and SF_4·triethylamine were recorded (Fig 4.2.4). The vibrational frequencies and their tentative assignments are listed in Table 4.4. In the Raman spectrum of SF_4·triethylamine adduct SF stretching bands were observed at 816 and 826 cm^{-1}, which are shifted from 896 and 857 cm^{-1} in neat SF_4. The symmetric axial SF_2 stretching mode is shifted from 536 for SF_4 to 498 cm^{-1} for the adduct. Changes in the Raman bands were observed for triethylamine upon formation of the SF_4·triethylamine adduct. The number of bands increased significantly, reflecting the lower symmetry of the triethylamine in the adduct. The aliphatic C–H stretching frequencies for triethylamine appear below 3000 cm^{-1} as expected for the alkyl group, while more splitting were observed for SF_4·triethylamine adduct. The C–N stretch at 1455 is split into three bands at 1483, 1461, and 1445 cm^{-1}. These facts clearly support

the formation of an adduct between SF_4 and triethylamine. The mass balance of the reaction indicates a 1:1 stereochemistry between SF_4 and triethylamine. When the adduct was warmed up to –35°C and SF_4 was removed under dynamic vacuum, the adduct dissociates and triethylamine was recovered with HF_2^- as an impurity (560 $cm^{-1}$and 1022 cm^{-1}), giving the same peaks in the Raman spectrum as were present in the original triethylamine.

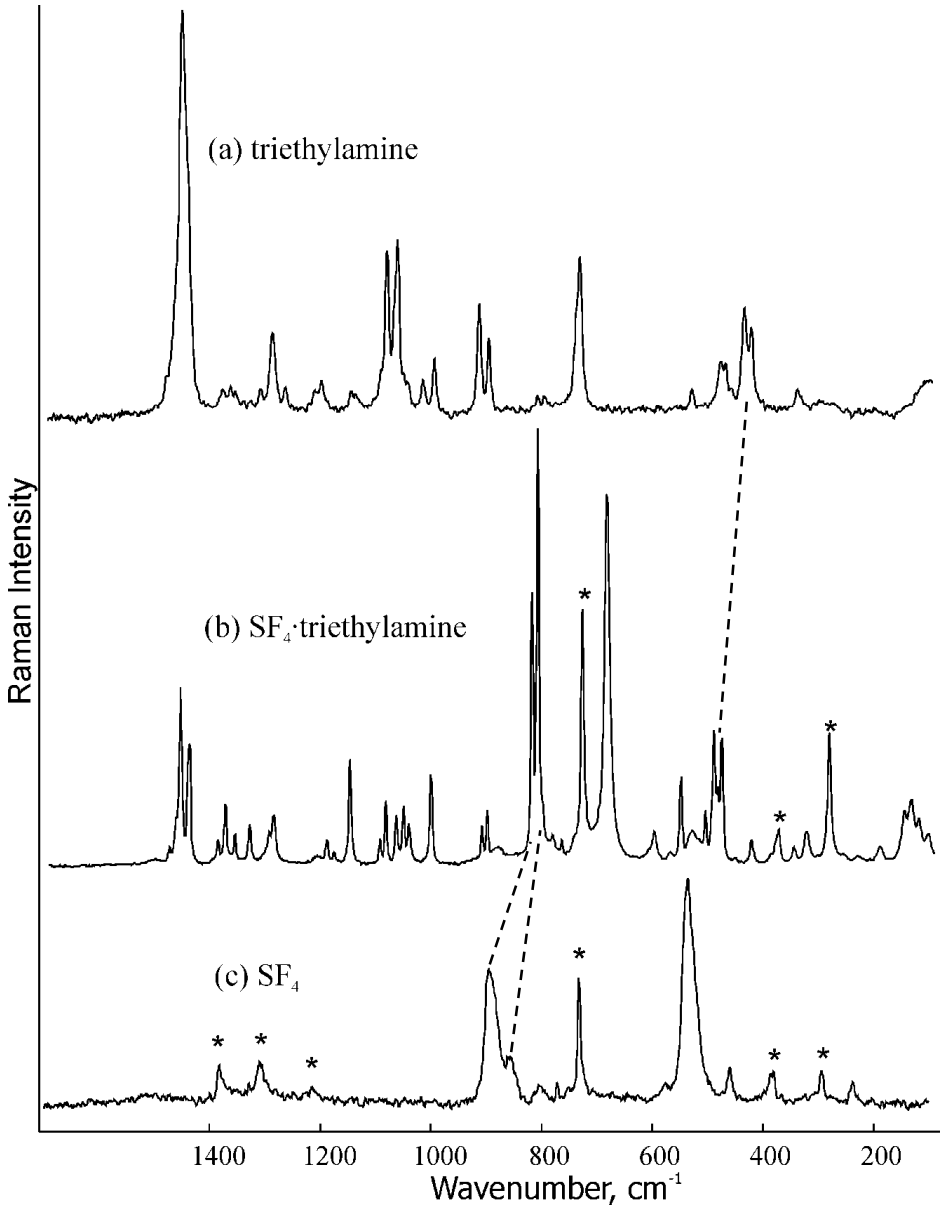

Figure 4.2.4 Raman Spectrum of SF_4, triethylamine, and SF_4·triethylamine adduct at –110°C. Asterisks (*) denote bands arising from the FEP sample tube.

Table 4.4 Raman frequencies (relative intensities), cm^{-1} of SF_4, triethylamine and SF_4·triethylamine adduct at –110°C.

triethyl amine[a]	SF_4[b]	triethyl amine·SF_4[c]	Assignments		
			triethyl amine[d]	SF_4[e]	triethylamine·SF_4
		2994 (22)			
		2980 (40)			
2967(75)		2970 (34)			
		2948(24)			
2934(100)		2933(12)	ν(C-H)		ν(C-H)
		2914(12)			
2923(sh)		2898(12)			
2899(49)					
2871(60)		2881(24)			
2795(39)		2854(14)			
2776(19)		2749(2)			
2750(18)		2726(2)	overtones		overtones
2734(14)		2720(2)			
2709(19)					
		1483(2)			
1455(58)		1461(40)	ν(C-N)		ν(C-N)
		1445(26)			
		1393(6)			
1383(2)		1380(14)[f]			
1369(2)		1363(6)			
1359(2)		1336(10)			
1316(2)		1301(6)[f]			
1292(15)		1293(10)			
1268(2)			δ(C-H)		δ(C-H)
1205(3)		1197(6)			
		1185(1)			
1150(1)		1156(24)			
1121(5)		1104(3)			
1085(20)		1091(14)			
1066(20)		1072(10)			
		1058(10)			
		1048(8)			
1000(13)		1009(22)	CH_3-rock.		CH_3-rock.
919(18)					
901(15)		918(6)			
		907(12)			
	896(65)	826(60)		$\nu_s(SF_{2eq})$	ν(S-F)
	857(32)	816(100)		$\nu_{as}(SF_{2eq})$	ν(S-F)
		790(1)			
		774(1)			
721(19)		736(42)[f]			
		691(80)			
		608(3)			
535(2)		558(22)	C_3N deform.		C_3N deform.

	536(100)	513(12) 498(28)	$\nu_s(SF_2)$ax $\delta_{sciss}(SF_{2,ax})$ + $\delta_{sciss}(SF_{2,eq})$	$\nu_s(SF_2)$ax $\delta_{sciss}(SF_{2,ax})$ + $\delta_{sciss}(SF_{2,eq})$
		491(18)		
483(10)		484(24)		
474(10)				
	461(10)		SF_2(eq) wagging	
440(16)		431(5)		
427(15)		381(8)[f]		
345(3)		354(1)		
		330(8)		
	237(6)	291(28)[f]	$\delta_{sciss}(SF_{2,ax})$– $\delta_{sciss}(SF_{2,eq})$	$\delta_{sciss}(SF_{2,ax})$– $\delta_{sciss}(SF_{2,eq})$

[a] The Raman spectrum was recorded in glass NMR tube at –110°C. [b] The Raman spectrum was recorded in a ¼–in FEP tube at –110°C. Signals from the FEP sample tube were observed at 294(8), 385(12), 733(53), 1216(2), 1306(1), 1382(2) cm^{-1}. Bands at 1382(19), 804(9), 772(11) cm^{-1} were observed for ν(S–O) SOF_2, ν(S–F) SOF_2 and ν(S–F) SF_6 respectively. [c] The Raman spectrum was recorded in a ¼-in FEP tube at –110°C. Signals from the FEP sample tube were observed at 295(sh), 385(6), 1216, 1306(sh) cm^{-1}. [d] Triethyl amine bands have been assigned based on references 22–23. [e] Sulfur tetrafluoride bands have been assigned based on references 8,9. [f] Overlap with FEP band.

A comparison of the S–F stretching bands in the four adducts relative to SF_4 are summarized in Table 4.5. For all four adducts similar shifts in the S–F stretching frequencies to lower frequencies have been observed compared to free SF_4. This reflects the weaker SF bonding in the adduct compared to free SF_4. Donor numbers are available for pyridine (33.1) and triethylamine (61), indicating the larger Lewis basicity of triethylamine.[24] In fact, the S–F stretching mode at 826 cm^{-1} for triethylamine is significantly lower than 852 cm^{-1} for pyridine. The observation is paralleled by the lower frequency for the symmetric axial SF_2 mode in triethylamine. The opposite trend for the SF stretching bands at 776 and 816 cm^{-1} seems counterintuitive and needs to be investigated by computational means. Although lutidine is expected to be a stronger base than pyridine, the SF stretching frequencies of its adduct appear at higher temperature.

This observation may be a consequence of the steric bulk from the ortho methyl groups of lutidine.

Table 4.5 Comparison of S–F stretching and $\delta_{sciss}(SF_{2,ax})+ \delta_{sciss}(SF_{2,eq})$ frequencies (cm^{-1}) in free SF_4 and in different adducts determined by Raman spectroscopy at –110°C.

SF_4	pyridine·SF_4	lutidine·SF_4	4–picoline·SF_4	triethylamine·SF_4	assignments
896(65) 857(32)	852(95) 776(76)	861(100) 820(66) 810(70)	841(100) 821(22)	826(60) 816(100)	$\nu(SF_{2,eq})$
536(100)	522(6) 513(18)	526(39) 505(35)	530(22) 514(18)	513(12) 498(28)	$\nu_s(SF_{2,ax})$ $\delta_{sciss}(SF_{2,ax})+ \delta_{sciss}(SF_{2,eq})$

4.2.3 NMR Spectroscopy of the Pyridine·SF_4 Adduct

The adduct formation between SF_4 and pyridine was also studied by solution-state ^1H, ^{19}F and ^{13}C NMR spectroscopy at low temperature in excess SF_4 as the solvent.

The sulfur tetrafluoride and the SF_4·pyridine adducts were characterized by low-temperature solution-state ^{19}F NMR spectroscopy. The NMR spectra are depicted in Fig. 4.2.5. The ^{19}F NMR spectrum of neat SF_4 at –60°C shows a very broad signal at 59.2 ppm which shows the fast exchange between the axial and equatorial fluorine environments in SF_4 at –60°C, likely as a consequence of an HF impurity.[25] Two sharp signals at 57.4 ppm and 72.0 ppm are observed due to the impurities of SF_6 and SOF_2 present in commercial samples of SF_4. Upon formation of the SF_4·pyridine adduct at –60°C, the SF_4 signal becomes narrower and shifts to 54.2 ppm due to the shielding by the electrons present on nitrogen of pyridine.

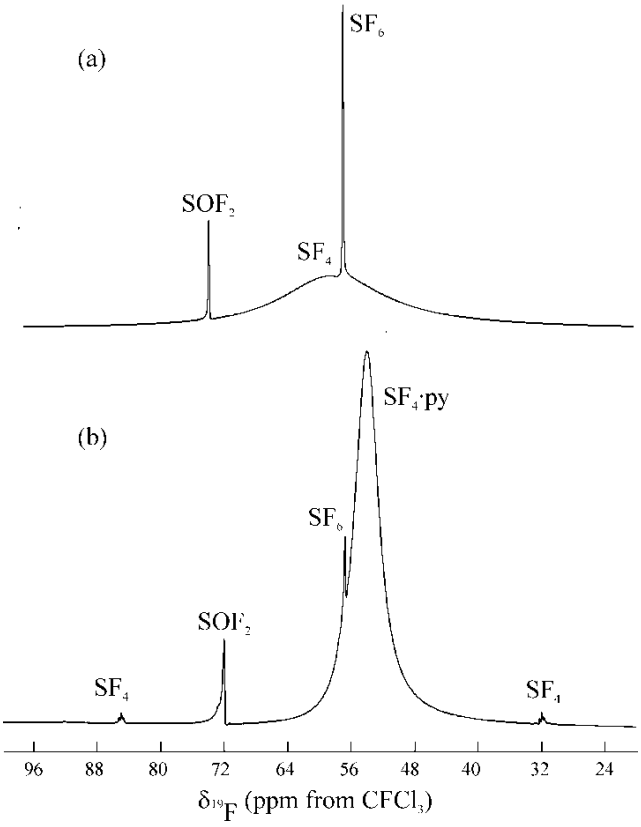

Figure 4.2.5 Solution-state ^{19}F NMR spectra of (a) neat SF_4 and (b) SF_4·pyridine in liquid SF_4 at –60°C

The ^1H NMR spectra of Pyridine and the SF_4·pyridine adduct were characterized by low- temperature solution-state ^1H NMR spectroscopy. The ^1H NMR spectra are depicted in Fig. 4.2.6. The ^1H NMR spectroscopy of pyridine at –56°C shows three broad peaks. The peak at 8.6 ppm can be assigned to the protons ortho to the nitrogen. The protons, in the meta position to the nitrogen, appears at 7.1 ppm and the signal for the proton para to the nitrogen appears at 7.5 ppm in pure pyridine. Upon the adduct formation of SF_4 with pyridine at –60°C, the signal for the protons having ortho, meta and para position to the nitrogen in pyridine have been shifted to 8.4, 7.2 and 7.6 ppm respectively, which is consistent with the formation of a N-S bond. This is consistent with

the literature published for the adduct between pyridine and trifluoroacetic anhydride at -78°C, where the peaks for ortho, meta and para protons were shifted from 8.03, 6.89, and 6.52 ppm in pyridine to 8.0 ppm, 7.2(br) ppm and 7.2(br) ppm in the adduct, respectively.[10]

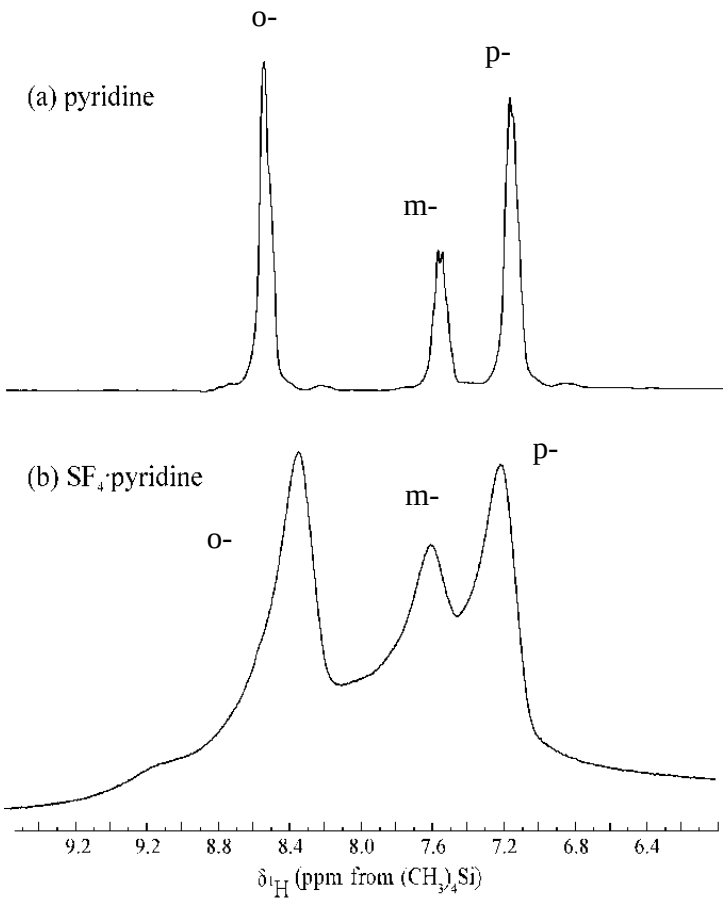

Figure 4.2.6 Solution-state ^{1}H NMR spectra of (a) neat pyridine at –56°C and (b) the SF_4·pyridine adduct in excess liquid SF_4 at –60°C.

Pyridine and the SF_4·pyridine adducts were characterized by low-temperature solution-state ^{13}C NMR spectroscopy. The NMR spectra are depicted in Fig. 4.2.7. Carbon-13 NMR spectroscopy of pyridine, at –56°C, shows three broad peaks. The peak at 158.1 ppm, 145.4 ppm and 132.0 ppm can be assigned to the carbons, ortho to the

nitrogen, para to the nitrogen, and meta to the nitrogen, in pyridine. In the SF_4·pyridine adduct, the signal at 158.1 ppm is shifted to 154.6 ppm, the signal at 145.4 ppm is shifted to 146.8 ppm and the signal at 132.0 ppm is shifted to 133.0 ppm at –60°C, indicating the formation of N–S bond. In the the adduct formation between pyridine and trifluoroacetic anhydride at -78°C, the peaks for ortho, meta and para carbons were shifted from 150.0, 135.8, and 123.8 ppm in pyridine to 143 ppm, 143(br) ppm and 125(br) ppm in the adduct, respectively.[10]

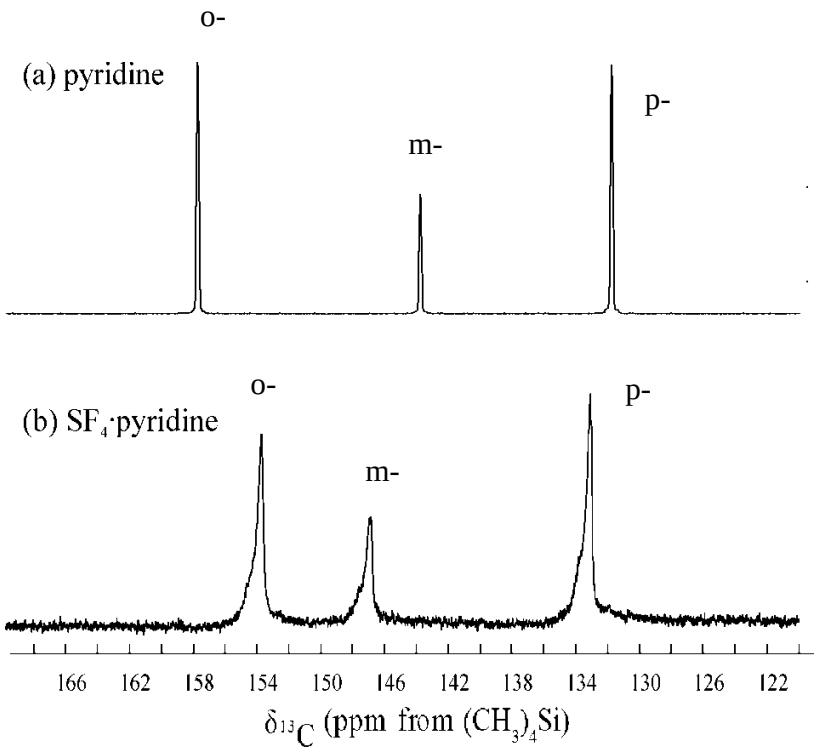

Figure 4.2.7 Solution-state ^{13}C NMR spectra of (a) neat pyridine at –56°C and (b) the SF_4·pyridine adduct in excess liquid SF_4 at –60°C.

4.3 Conclusion:

Adducts of SF_4 with four nitrogen bases were prepared and characterized by Raman spectroscopy and by NMR spectroscopy in the case of the pyridine·SF_4 complex. This study presents the first unambiguous spectroscopic evidence for adducts of SF_4 with nitrogen bases. It has been found that these weak adducts formation process is reversible in nature. No adduct formation of SF_4 with quinoline, isoquinoline and 2,2'-bipyridine was observed at –80°C, as shown by Raman spectroscopy.

References:

1. Miller, T. M.; Viggiano, A. A.; Dolbier, W. R.; Sergeeva, T. A.; Friedman, J. F. *J. Phys. Chem. A.* **2007,** *111*, 1024.
2. Cohen, B.; Hoover, T. R.; Pered, R. D. *Inorg. Nucl. Chem.* **1966**, *28*, 919.
3. Cohen, B.; MacDiarmind, A. G. *Angew. Chem., Int. Ed.* **1963**, *75*, 207.
4. Muetterties, E. L. *J. Am. Chem. Soc.* **1960**, *82*, 1082.
5. Padma, D. K. *J. Fluorine Chem.* **1974**, *4*, 441.
6. Sass, C. S.; Ault, B. S. *J. Phys. Chem.* **1985**, *89*, 1002.
7. Holleman, A. F.; Wiberg, N. *Inorganic Chemistry*, Academic Press, San Diego, California, 2001, p. 526.
8. Christe, K. O.; Willner, H; Sawodny, W. *Spectrochim. Acta* **1979**, *35A*, 1347.
9. Dodd, R. E.; Woodward, L. A. ; Roberts H. L. *Trans. Faraday Soc.* **1956**, *52*, 1052.
10. Anthoni, U.; Christensen, D.; Christophersen, C.; Nielsen, P. H. *Acta Chem. Scand.* **1995**, *49*, 203.

11. Urena, P. F.; Gomez, F. M.; Gonzalez, J. J. L.; Torres, M. E. *Spectrochim. Acta A* **2003**, *59*, 2815.

12. Szafran, M.; Koput, J. *J. Mol. Struc.* **2001**, *565*, 439.

13. Destexhe, A.; Smets, J.; Adamowicz, L.; Maes, G. *J. Phys. Chem.* **1994**, *98*, 1506.

14. Clark, R. J. H.; Williams, C. S. *Inorg. Chem.* **1965**, *4*, 350.

15. Tressaud, A. Functionalized Inorganic Fluorides, WILEY-VCH Verlag GmbH & Co. KGaA: Weinheim, 2010, 131.

16. Chaudhary, P.; Gerken, M; Goettel, J.; Hazendonk, P.; Mercier, H. P. A. *CSC Conference*, Toronto **2010**, INP 116.

17. Bondi, A. *J. Phys. Chem.*, **1964**, *68*, 441.

18. Harmon, M. K.; Lovelace, R. R. *J. Phys. Chem.* **1982**, *86*, 900.

19. Arenas, J. F.; Otero, J. C.; Centeno, S. P.; Tocon, I. P.; Soto, J. *Surface Sci.* **2002**, *511*, 163.

20. Cardini, G., Muniz-Miranda, M.; Schettino, V. *J. Phys. Chem. B.* **2004**, *108*, 17007.

21. Tocon, I. L.; Woolley, M. S.; Otero, J. C.; Marcos, J. I. *J. Mol. Struc.* **1998**, *470*, 241.

22. Lien, C. F.; Lin Y. F.; Lin, Y. S.; Chen, M. T.; Lin, J. L. *J. Phys. Chem. B* **2004**, *108*, 18261.

23. Hata, T. *Bull. Chem. Research Inst. of Non-Aqueous Solutions* **1972**, 106.

24. Gutmann, V.; Resch, G. *Lecture notes on Solution Chemistry*, World Scientific Publishing Co., Singapore, 1995, 134.

25. Janzen, A. F. *Coord. Chem. Rev.*, **1994**, *130*, 355.

Chapter-5

Phase-Behavior of $[SF_3][MF_6]$, M = As, Sb

5.1 Introduction

Sulfur tetrafluoride is very well known for its fluoride-ion-donor properties towards strong Lewis acids such as BF_3, AsF_5, SbF_5 to form salts of the type $[SF_3][BF_4]$, $[SF_3][AsF_6]$ and $[SF_3][SbF_6]$.[1] Muetterties and coworkers suggested the validity of an ionic formulation of $[SF_3][SbF_6]$ based on solution-state ^{19}F NMR study of $[SF_3][AsF_4]$, because the ^{19}F NMR spectrum of the $[SF_3][AsF_4]$ system at temperatures as low as –60°C showed only one type of fluorine environment as a consequence of rapid exchange of fluorine atoms between the cations and anions.[2] Association and dissociation of a simple acid-base adduct would not provide a mechanism for exchange of fluorine atoms bonded to arsenic with those bonded to sulfur. It was also predicted that the $[SF_3][SbF_6]$ salt exhibits fluorine bridging in between SF_3^+ and SbF_6^- so that $[SF_3^+]$ would attain a pseudo octahedral symmetry.[2] On the basis of vibrational spectroscopy, Gillespie and coworkers found that the SF_4 adducts with BF_3, AsF_5, and SbF_5 were essentially SF_3^+ salts; however, they interpreted deviations of the observed spectra from the idealized ionic formulation in terms of fluorine bridging between anions and cations.[3]

Neil Bartlett and coworkers presented X-ray crystallographic data on $[SF_3][BF_4]$ showing SF_3^+ cations with short contacts of 2.624(2) Å (2×) and 2.593(3) Å with fluorine atoms of the three closest BF_4^- groups, increasing the coordination number of sulfur to six.[4] On the other hand, the X-ray structure of $[SF_3][SbF_6]$ has not been determined due to

the powder nature of the salt, and the quality of the X-ray crystallographic data on $[SF_3][AsF_6]$ was poor.[4] As a consequence no structural information could be obtained.

Several thermally unstable salts of SF_3^+ with GeF_6^{2-}, GeF_5^-, SO_3F^- and $CF_3SO_3^-$ have also been prepared. All the salts were characterized by Raman spectroscopy.[5] In addition, a crystal structure of $[SF_3^+]_2[GeF_6^{2-}]$ was reported, also showing short anion-cation contacts.[5]

The stability order of known SF_3^+ salts may be given as: $[SF_3][SbF_6]$ (m.p. 253°C) > $[SF_3][AsF_6]$ > $[SF_3][IrF_6]$ > $[SF_3][BF_4]$ > $[SF_3][PF_6]$ > $[(SF_3)_2][GeF_6]$ > $[SF_3][AsF_4]$ (m.p. –20°C).[6]

5.2 Results and Discussion

5.2.1 Raman Spectroscopy

5.2.1.1 Raman spectroscopy of $[SF_3^+][SbF_6^-]$

Variable-temperature Raman spectra of $[SF_3][SbF_6]$ were recorded at temperatures between ambient temperature and –125°C (Figure 5.1). The observed Raman spectrum of $[SF_3^+][SbF_6^-]$ at ambient temperature agrees well with the spectrum reported by Azeem *et al.*[1] Vibrational frequencies of $[SF_3][SbF_6]$ at –25°C, –65°C and –125°C are listed in Table 5.1 together with their assignments. The free SF_3^+ cation and SbF_6^- anion are expected to adopt C_{3v} and O_h point symmetries, respectively, on the basis of the VSEPR model. Hence, the symmetry labels of the C_{3v} and O_h point groups are used in the discussion of the Raman spectra.

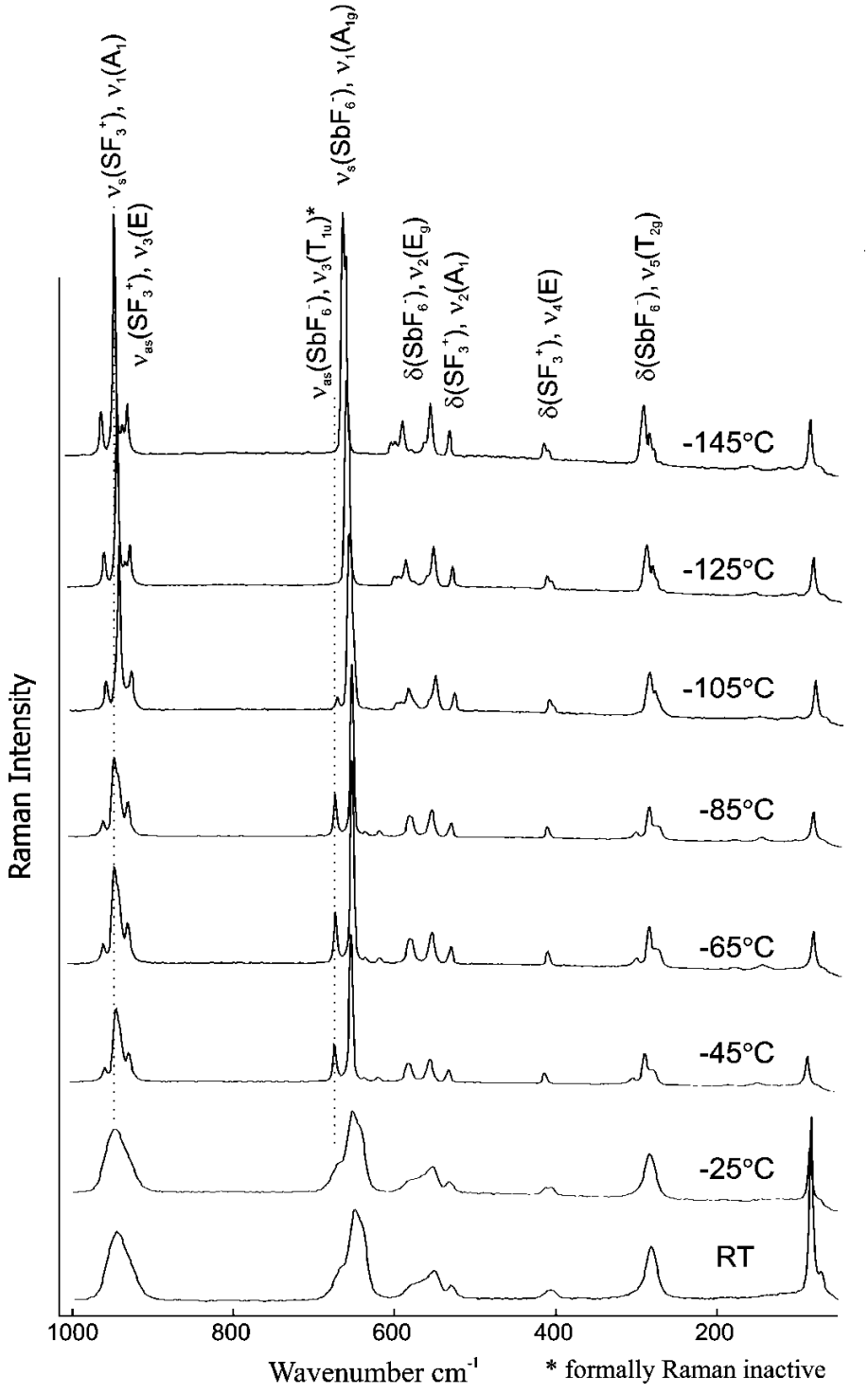

Figure 5.1 Variable-temperature Raman spectra of SF_3SbF_6. 'RT' denotes room-temperature.

Table 5.1 Raman frequencies (relative intensities) and their assignments for $[SF_3][SbF_6]$

Frequency (cm^{-1})			Assignments	
–25°C	–65°C	–125°C	SF_3^+ (C_{3v})	SbF_6^- (O_h)
	956(14)	955(20)		
946(79)	943(50)	939(95)	$\nu_1(A_1)$, $\nu_s(SF_3)$	
928(sh)	938(sh)	929(15)	$\nu_3(E)$, $\nu_{as}(SF_3)$	
	926(24)	923(23)		
669(sh)	671(29)			$\nu_3(T_{1u})$, $\nu_{as}(SbF_6)$
652(100)	650(100)	658(100)		$\nu_1(A_{1g})$, $\nu_s(SbF_6)$
643(sh)	634(8)			
	617(8)			
		598(6)		
		593(6)		
581(sh)	580(17)	585(15)		$\nu_2(E_g)$, $\nu_{as}(SbF_6)$
		575(3)		
		557(8)		
552(46)	552(20)	550(23)		
	533(sh)			
532(21)	529(13)	527(14)	$\nu_2(A_1)$, $\delta(SF_3)$	
411(12)	410(11)	410(9)	$\nu_4(E)$, $\delta(SF_3)$	
406(12)		406(6)		
	301(8)	288(25)		
283(57)	286(22)	281(15)		$\nu_5(T_{2g})$, $\delta(SbF_6)$
	274(12)	276(sh)		

At –25°C, a Raman band for SF_3^+ at 946 cm^{-1} is observed and can be assigned to the symmetric cation stretching mode. The shoulder at 928 cm^{-1} can be assigned to the asymmetric stretching mode for SF_3^+ based on the assignment made by Azeem *et al.*[1] The broad Raman bands at 532 and 411 cm^{-1} can be attributed to the A_1 and E bending modes of SF_3^+, respectively. Another broad band is observed at 652 cm^{-1} having a little shoulder at 669 cm^{-1}. The band at 652 cm^{-1} has been assigned to A_{1g} stretching mode of the SbF_6^- anion, and the shoulder at 669 cm^{-1} can be assigned to T_{1u} mode for SbF_6^- anion, which is formally Raman forbidden.

The observation of a formally Raman forbidden mode in the Raman spectrum of solid $[SF_3][SbF_6]$ indicates severe distortion of the anion from octahedral symmetry. The broad signals at 552 and 283 cm^{-1} can also be attributed to SbF_6^- anion modes. The overall broadness of bands in the Raman spectrum at –25°C can be attributed to some motion at the Raman time scale. This modification of $[SF_3^+][SbF_6^-]$ has been denoted as the α-phase of $[SF_3^+][SbF_6^-]$.

As the temperature is lowered to –45°C, the signals become significantly narrower allowing to resolve the formally Raman inactive T_{1u} mode for SbF_6^-anion at 671 cm^{-1}, which results from significant distortion of the octahedral SbF_6^- anion in the solid state. The deviation of the anion symmetry from octahedral is corroborated by the observation of splitting for the $v_2(E_g)$ (552 cm^{-1}) and $v_5(T_{2g})$ (286 cm^{-1}) modes into two and three signals, respectively. The v_3(E) asymmetric stretching mode of SF_3^+ seems to split into two peaks likely because of lowering of cation symmetry (926 and 938(sh) cm^{-1}). These changes could arise because of continuous sharpening of the Raman bands

upon decreasing the temperature or the existence of a distinctly different modification. The latter explanation is supported by solid-state NMR spectroscopy (vide infra). The modification that is stable between –45 and –85°C is assigned to the β-phase of $[SF_3^+][SbF_6^-]$.

As the temperature is further lowered below –85°C, further changes are observed. For example, a different triplet splitting pattern for the $v_5(T_{2g})$ mode of SbF_6^- is observed compared to the pattern observed at –65°C. Also, additional splitting of the $v_2(E_g)$ mode for SbF_6^- around 575 and 585 cm^{-1} is observed. The complex splitting pattern of the $v_2(E_g)$ mode could be a consequence of vibrational coupling of the anions within a unit cell. The signal at 671cm^{-1} that was attributed to the Raman forbidden T_{1u} mode of octahedral SbF_6^- is not observed in Raman spectrum at –125°C anymore. These changes suggest a third distinctly different modification for $[SF_3^+][SbF_6^-]$ at this temperature and in the present work it has been assigned to the γ-$[SF_3^+][SbF_6^-]$ phase. Hence, on the basis of variable-temperature Raman spectroscopy transition temperatures between the three phases for $[SF_3^+][SbF_6^-]$ have been determined as given in Eq. 5.1.

$$\alpha\text{-}[SF_3^+][SbF_6^-] \underset{}{\overset{-25 \text{ to } -45℃}{\rightleftharpoons}} \beta\text{-}[SF_3^+][SbF_6^-] \underset{}{\overset{-85 \text{ to } -105℃}{\rightleftharpoons}} \gamma\text{-}[SF_3^+][SbF_6^-] \qquad (5.1)$$

5.2.1.2 Raman Spectroscopy of $[SF_3^+][AsF_6^-]$

In order to investigate the phase behavior of $[SF_3][AsF_6]$, variable-temperature Raman spectra were recorded. No significant changes were observed in the Raman spectra of $[SF_3^+][AsF_6^-]$ between room-temperature and –145ºC. The observed spectrum of

$[SF_3^+][AsF_6^-]$ at ambient temperature (Fig 5.2) agrees well with the spectrum recorded by Azeem *et al*. available in literature.[1] The frequencies at 926 and 945 cm^{-1} can be assigned to SF_3^+ stretching bands while at 686, 563 and 587 cm^{-1} can be assigned to AsF_6^- stretching frequencies.

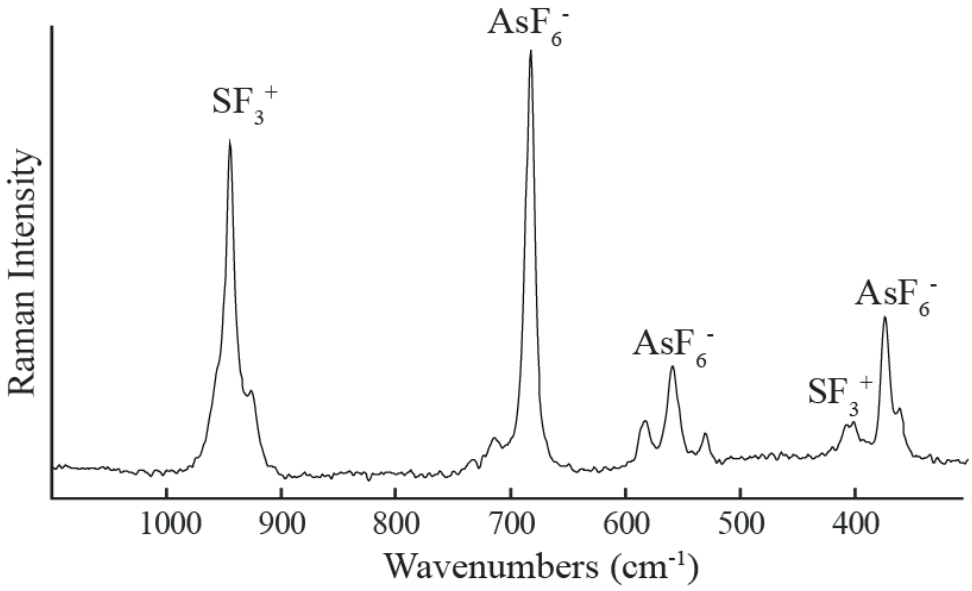

Figure 5.2 Raman spectrum of $[SF_3][AsF_6]$ at ambient temperature

Table 5.2 Assignment of Raman frequencies of SF_3AsF_6

Frequency (cm^{-1})	Assignment	
	SF_3^+ (C_{3v})	AsF_6^- (O_h)
960 (sh)		
945(81)	$\nu_1(A_1)$, $\nu_s(SF_3)$	
926(29)	$\nu_3(E)$, $\nu_{as}(SF_3)$	
686(100)		$\nu_1(A_{1g})$, $\nu_{as}(AsF_6)$
587(23)		$\nu_2(E_g)$, $\nu_{as}(AsF_6)$
563(32)		
530(20)	$\nu_2(A_1)$, $\delta(SF_3)$	
411(22)	$\nu_4(E)$, $\delta(SF_3)$	
379(44)		$\nu_5(T_{2g})$, $\delta(AsF_6)$

5.2.2 Solid-State ^{19}F MAS NMR Spectroscopy

5.2.2.1 Solid-State ^{19}F MAS NMR Spectroscopy of $[SF_3][SbF_6]$

Variable-temperature solid-state ^{19}F MAS NMR spectra of $[SF_3][SbF_6]$ inside a FEP insert were recorded between –25°C to –125°C (Fig 5.3). The ^{19}F NMR spectrum at –25°C shows resonances attributed to the SF_3^+ cation at +37.5 ppm and SbF_6^- anion at –115.6 ppm, besides an isotropic peak at –119.8 ppm and its spinning side bands manifold due to the FEP insert. In the solution-state ^{19}F NMR spectra, resonances were found at –27.1 ppm and +124.3 ppm for the SF_3^+ cation and SbF_6^- anion in anhydrous HF solvent, respectively.[1] The observation of one cation and one anion resonance in the solid state indicates the fast exchange of fluorine environments in the cation and in the anion on the

NMR time scale. The singlet of SbF_6^- anion can be attributed to the fast exchange of different fluorine atoms around antimony and fast relaxing quadrupolar ^{121}Sb and ^{123}Sb nuclides due to the presence of a significant electric field gradient.

Lowering the temperature below –25°C results in changes in the SbF_6^- anion signal, as well as in the SF_3^+ cation signal. The new resonances can be attributed to the β-phase of $[SF_3^+][SbF_6^-]$. At –45°C, a multiplet for the SbF_6^- anion appears, and for the SF_3^+ cation an additional broad singlet resonance emerges at 33.6 ppm besides the singlet at 37.5 ppm (Fig 5.3). At –65°C, the singlet at 37.5 ppm essentially disappears. The line-width of the singlet at 33.6 ppm is significantly larger than that at 37.5 ppm. In addition, the observation of spinning side bands for the new singlet at 33.6 ppm can be explained by a significant inequivalence of the shielding tensors of the fluorine environments in the SF_3^+ cation of β-$[SF_3^+][SbF_6^-]$ compared to that of the α-modification. The narrow ^{19}F resonance for α-$[SF_3^+][SbF_6^-]$ that shows no significant spinning sidebands reveals the similarity of the fluorine shielding tensors in the SF_3^+ cation. At –65°C, the multiplet in the SbF_6^- region is best resolved (Fig 5.5). The multiplet in Figure 5.4 and 5.5 arises from coupling between ^{19}F and Sb. Antimony has two quadrupolar nuclides, i.e., ^{121}Sb (natural abundance: 57.21%, spin: I = 5/2) and ^{123}Sb (natural abundance: 42.79%, spin: I = 7/2). As a result of coupling to ^{121}Sb and ^{123}Sb the superposition (equal interaction) of sextet and octet subspectra are observed. Because of the fast quadrupolar relaxation, ^1J–coupling between ^{19}F and ^{121}Sb as well as ^{123}Sb is frequently not observed in ^{19}F NMR spectra. Scalar–coupling to the quadrupolar nuclei is only observed for very symmetric (e.g. octahedral) environments about Sb, where the effective electric field gradient about the quadrupolar nucleus is zero. This has been observed in the HF solution of $NaSbF_6$

where the values for $^{1}J(^{121}Sb–^{19}F)$ and $^{1}J(^{123}Sb–^{19}F)$ were found to be 1945 ± 5 Hz and 1055±5 Hz, respectively.[7] Due to the coupling between a quadrupolar nucleus and a spin-1/2 nucleus, residual dipolar coupling effects are observed in the *J*-couplings between antimony and fluorine nucleus as has been explained in the section 1.5.1.9. Rather than observing a constant spacing between lines, a uniform increase in spacing is observed going from low to high frequency in the multiplet (Fig 5.4).

Upon lowering the temperature to –105°C, the multiplet pattern for the SbF_6^- anion disappears and a new singlet for SbF_6^- appears at –115.5 ppm. This observation is paralleled by the appearance of a sharp singlet for the SF_3^+ cation at +38.1 ppm with no significant spinning sidebands, indicating again the fast exchange of the fluorine atoms on NMR time scale. (Fig. 5.4). The broad singlet for the SbF_6^- anion is an indication of the reintroduction of the electric field gradient that results in fast quadrupolar relaxation of the ^{121}Sb and ^{123}Sb nuclides and the restriction on fluxionality on fluorines due to low-temperature.

Thus, three modifications are observed between –25°C and –145°C by solid-state ^{19}F NMR spectroscopy (Eq. 5.1), paralleling the Raman spectroscopic observations. The ^{19}F chemical shift of SF_3^+ and the ^{19}F signal of SbF_6^- are different for these modifications.

In summary, the fluorine environments in all three phases are in the fast exchange regime. In the α-phase (above –45°C) the single peaks for SF_3^+ and SbF_6^- are the result of fast exchange of fluorine environment on both SF_3^+ cation and SbF_6^- anion along with fast relaxing quadrupolar ^{121}Sb and ^{123}Sb nuclides in case of SbF_6^- anion. In the β-phase (between – 45°C to –85°C), because the rapid exchange of the fluorine environments in

the anion emulates perfect octahedral anion symmetry, the electric field gradient is average to essentially zero. Hence, the splitting pattern due to the coupling between the quadrupolar antimony nuclides with the ^{19}F nucleus is seen. At the same time the fluorine environment around sulfur is becoming inequivalent resulting in an additional broad peak. In the γ-phase (below –85°C) the new singlets for SF_3^+ and SbF_6^- are the result of again fast exchange of fluorine environment on both SF_3^+ cation and SbF_6^- anion alongwith the fast relaxing quadrupolar ^{121}Sb and ^{123}Sb nuclides in case of SbF_6^- anion. However, the broadness in the SbF_6^- anion peak is a result of the slow-down in motion at this temperature.

The difference between Raman and NMR spectroscopy with respect to β-$[SF_3^+][SbF_6^-]$ is a consequence of their different time-scales. In Raman spectroscopy the lifetime of excited states is much shorter than in NMR spectroscopy, where relaxation processes take place in seconds.

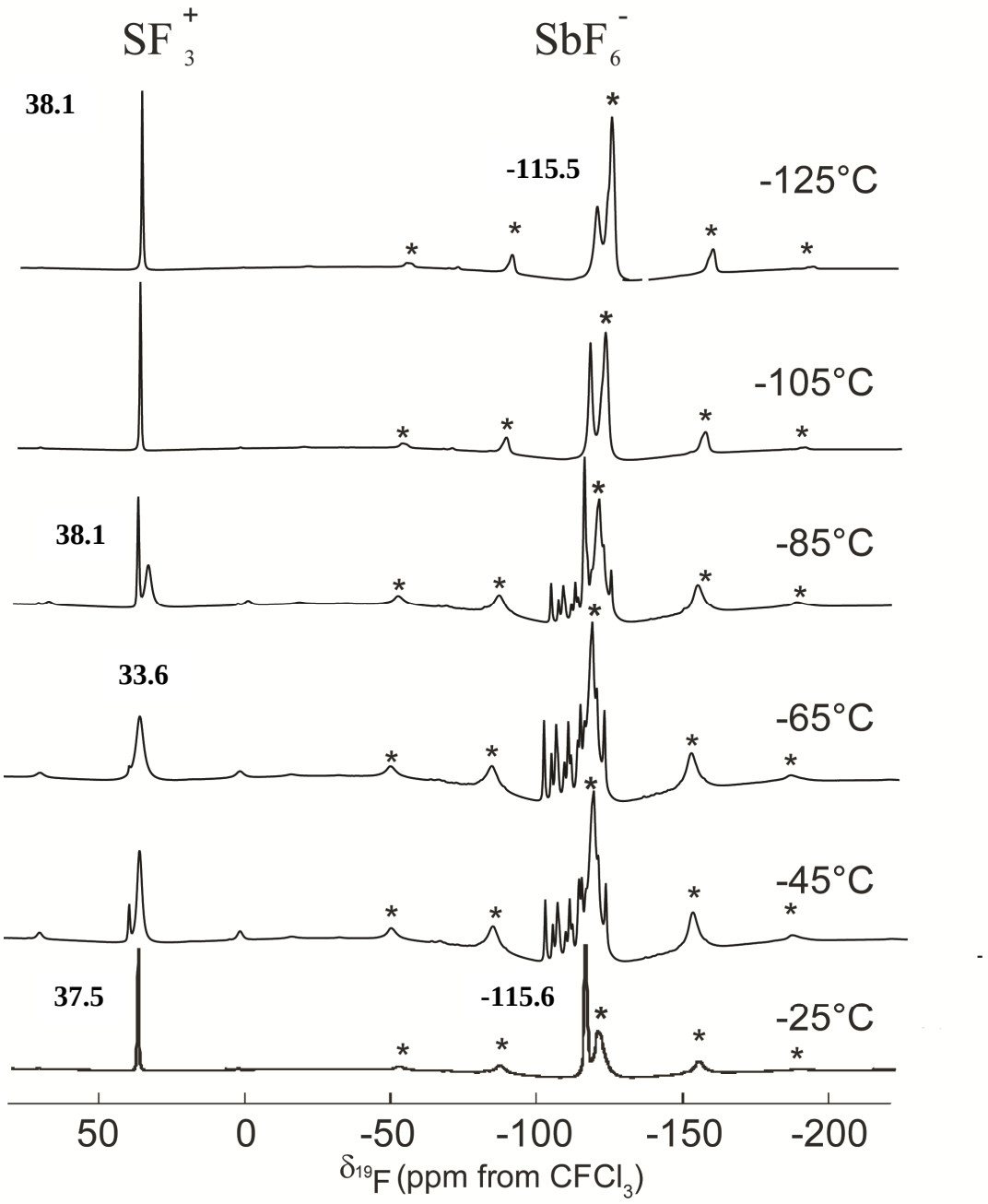

Figure 5.3 Variable low temperature ^{19}F solid state MAS 16 kHz NMR spectra of $[SF_3][SbF_6]$ where asterisks (*) denote the spinning sideband manifold arising from FEP sample tube (δ_{iso} = –123.6 ppm).

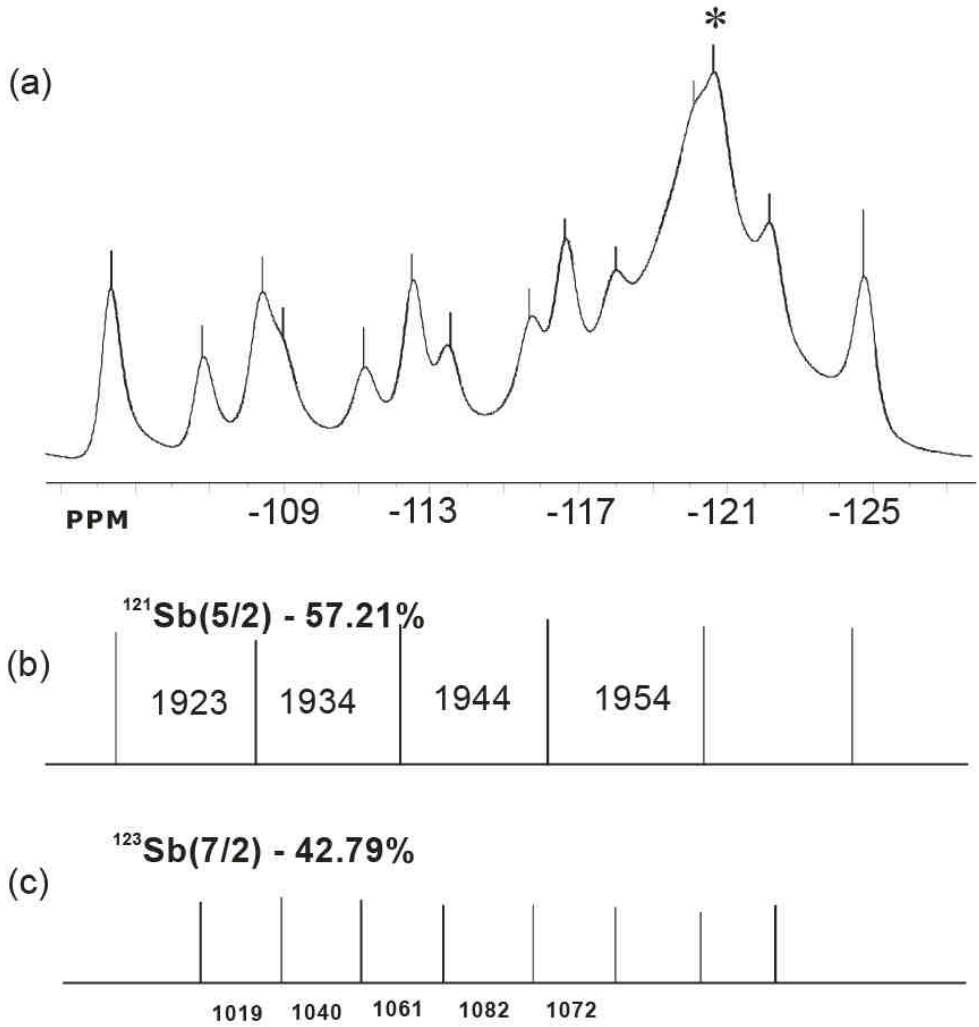

Figure 5.4 (a) Antimony nuclei (spin- 5/2 &7/2) to fluorine (spin-1/2) coupling pattern shown by solid–state ^{19}F NMR spectrum of $[SF_3][SbF_6]$ at -65°C (b) coupling pattern of ^{121}Sb (spin–5/2) with ^{19}F nucleus (c) coupling pattern of ^{123}Sb (spin-7/2) with ^{19}F nucleus. Asterisk (*) denotes the overlap of the multiplet with the FEP signal. The low-frequency spacings could not be determined accurately because of overlap with the FEP signal.

5.2.2.2 Solid-State ^{19}F MAS NMR Spectroscopy of $[SF_3][AsF_6]$

In the solid-state ^{19}F MAS NMR spectrum of $[SF_3][AsF_6]$, a singlet with the spinning sidebands is observed at 32.3 ppm for SF_3^+ while for AsF_6^- a broad peak is observed at –61.9 ppm (Figure 5.5), which is in good agreement with literature where ^{19}F

NMR spectrum was recorded in liquid SO_2 for $C_{60}(AsF_6)_x$ (–64.5 ppm).[8] The single broad AsF_6^- anion peak is due to the fast relaxing arsenic quadrupolar nucleus. The fast relaxing arsenic nucleus provides no $^1J(^{75}As\text{-}^{19}F)$ scalar coupling. However, $^1J(^{75}As\text{-}^{19}F)$ has been observed by solution-state ^{19}F NMR spectroscopy with a $^1J(^{75}As\text{-}^{19}F)$ coupling constant of 930 Hz.[9] The spinning sideband pattern of SF_3^+ cation indicates the significant inequivalence of the shielding tensors of the three cation fluorines, as observed for the β-modification of $[SF_3][SbF_6]$. The FEP isotropic peak shows up at –123.6 ppm with spinning sideband manifold. The variable low-temperature solid-state ^{19}F NMR spectroscopy of $[SF_3][AsF_6]$ shows no significant changes from –25°C to –125°C (Figure 5.6), and this result is consistent with variable low-temperature Raman spectroscopy.

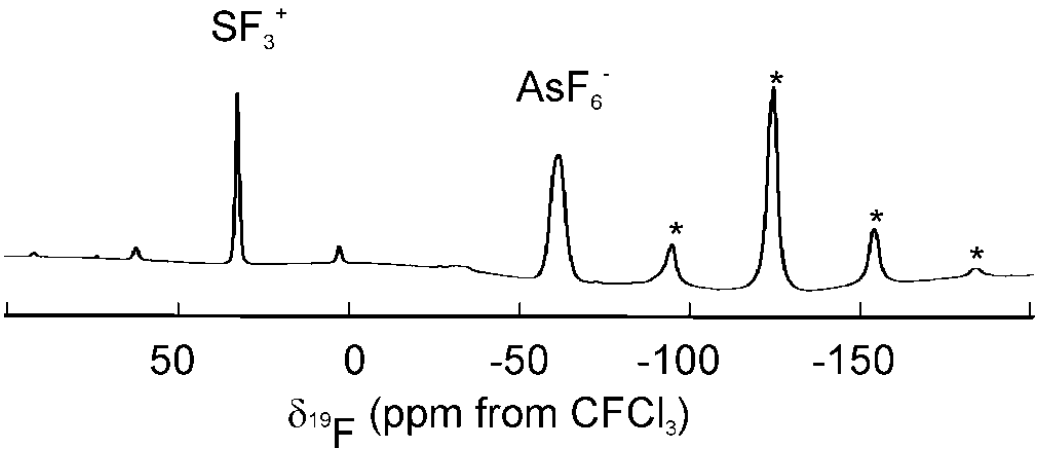

Figure 5.5 Solid-state MAS 14 kHz ^{19}F NMR spectra of $[SF_3][AsF_6]$. Asterisks(*) denote the spinning sideband manifold arising from the FEP sample tube (isotropic peak at –123.6 ppm).

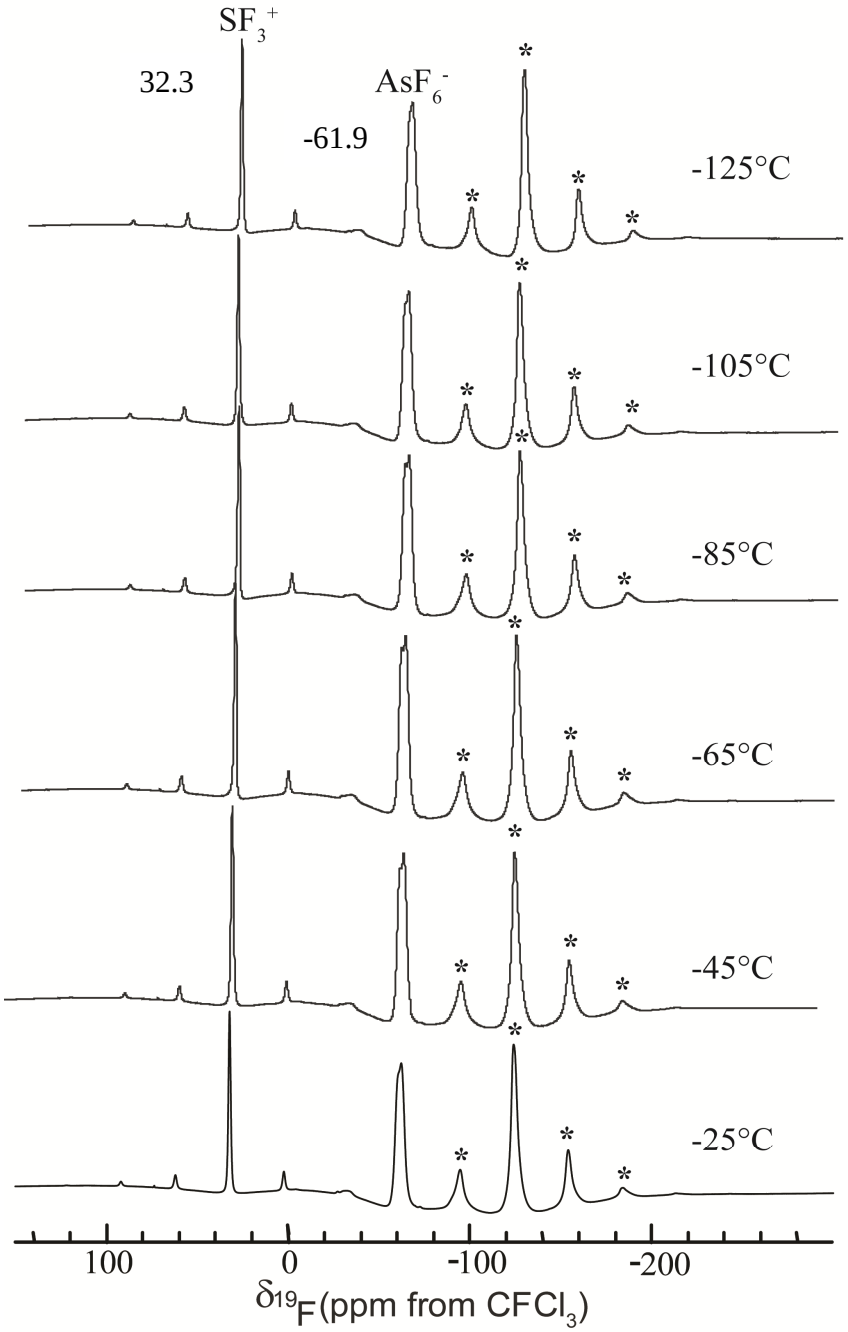

Figure 5.6 Variable-temperature solid-state ^{19}F NMR spectra of $[SF_3][AsF_6]$ at MAS 14 kHz. Asterisks (*) denote the spinning sideband manifold arising from the FEP sample tube (isotropic peak at –123.6 ppm). The AsF_6^- resonance shows overlap with one of the sideband from FEP.

5.2.3 X-ray Crystallography of $SF_3^+(HF)SbF_6^-$

In order to structurally characterize the three phases of $[SF_3^+][SbF_6^-]$, crystal growth was attempted from anhydrous HF, because anhydrous HF is a good solvent for SF_3^+ salts and is inert. Crystallization from anhydrous HF at low-temperature furnished colorless crystals of $[SF_3^+](HF)[SbF_6^-]$ instead. The crystals were grown and manipulated at low temperature, i.e., below –70 °C. The $[SF_3^+](HF)[SbF_6^-]$ crystallizes in the monoclinic space group $P2_1/c$ with four formula units $[SF_3^+](HF)[SbF_6^-]$ in the unit cell. A comparison for the known $[SF_3^+]$ structures, i.e, $[SF_3^+](HF)[SbF_6^-]$, $[SF_3^+][BF_4^-]$[4] and $[(SF_3)_2^+][GeF_6^{2-}]$,[5] is summarized in the Table 5.3.

The crystal structure contains SF_3^+ cation, SbF_6^- anion, as well as a HF solvent molecule that is bridging a SF_3^+ cation and a SbF_6^- anion. In the crystal structure of $[SF_3^+](HF)[SbF_6^-]$, the SbF_6^- has a distorted octahedral structure. The SF_3^+ cation adopts a trigonal pyramidal geometry with approximate C_{3v} symmetry and S–F bond lengths ranging from 1.506(9) to 1.510(9) Å. The coordination sphere about S is expanded by contacts to two fluorine atoms of two SbF_6^- anions (2.567(1) and 2.533(1) Å) and to the fluorine of one HF molecule (2.528(1) Å), increasing the total coordination number of sulfur to six (Fig. 5.7(c) and Fig. 5.9). The S···Fcontacts seem to avoid the lone pair on the SF_3^+ cation. All of these secondary contacts are shorter than the sum of van der Waal's radii (2.65 Å).[10] The fluorine contacts between SF_3^+ and SbF_6^- in this structure (Fig 5.7) are similar to those found in $[SF_3^+][BF_4^-]$ (2.593(3) and 2.624(2)Å),[4] but significantly longer than those in $[SF_3^+]_2[GeF_6^{2-}]$ (2.367(2) and 2.420(1)Å)[5]. The F(10)–

S–F(1) angle is essentially linear (179.05(5)°). But the F(2)–S–F(8B) and F(3)–S–F(4A) angles are 174.84(5)° and 174.55(5)°, respectively, which deviate from linearity.

This crystal structure is one of the few known structures of an HF solvate. Other crystal structures available for HF solvate system are $[OsO_3F][HF][SbF_6]$, $[OsO_3F][HF]_2[AsF_6]$[11], $La(HF)_2(AsF_6)_3$[12], and $[(\eta^5\text{-}C_5Me_5)NbF_4(HF)AsF_3]_2$.[13] The distance between the hydrogen-bonded fluorines F(10) and F(6) is 2.6294(17) Å, which is smaller than the sum of the van der Waal radii (2.94 Å)[10] and is close to the F···F distance found in $[(\eta^5\text{-}C_5Me_5)NbF_4(HF)AsF_3]_2$ (2.686Å).[13] Compared to the osmium compounds $[OsO_3F][HF][SbF_6]$ (2.38(2) Å) and $[OsO_3F][HF]_2[AsF_6]$[11] (2.429(8)Å and 2.512(8)Å), the F···F distances are longer in $[SF_3^+](HF)[SbF_6^-]$ (Figure 5.8).

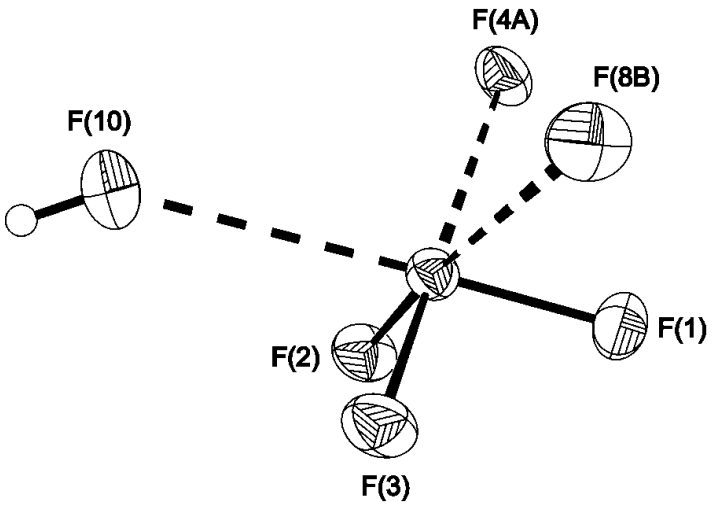

Figure: 5.7 Structure of SF_3^+ cation in the crystal of $[SF_3^+](HF)[SbF_6^-]$ from X-ray crystallography. Thermal ellipsoids are drawn at the 50% probability level.

Table 5.3 Bond lengths and contacts and bond angles for $[SF_3^+]$ in three different compounds

	S–F bond length (Å)	S···F contacts (Å)	F–S–F bond Angle (°)	Reference
$[SF_3^+]$ $[BF_4^-]$	1.499(2) 1.495(2)	2.593(3) 2.624(2)	97.62(7) 97.39(12)	4
$[SF_3^+]_2$ $[GeF_6^{2-}]$	1.515(2) 1.519(1)	2.420(1) 2.367(2)	96.23(10) 96.12(8)	5
$[SF_3^+]$ (HF)$[SbF_6^-]$	1.508(10) 1.506(9) 1.510(9)	2.533(1) 2.567(1) 2.528(1)	97.69(7) 97.89(6) 97.45(6)	Present work

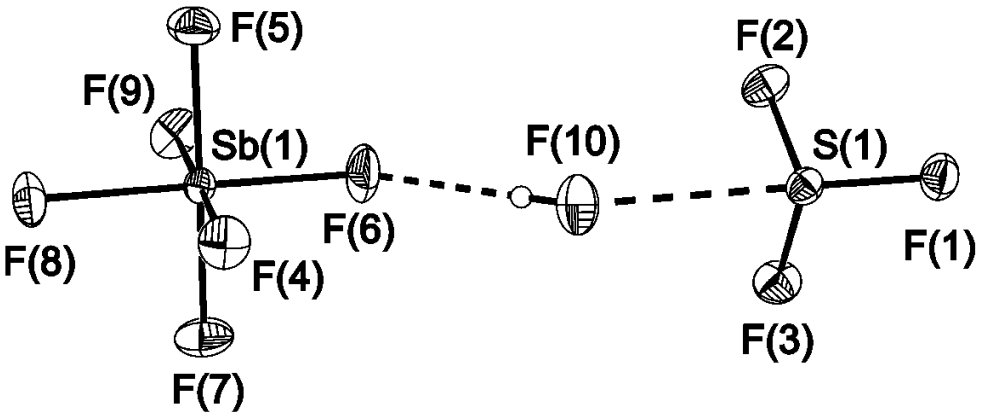

Figure: 5.8 Structure of $[SF_3^+](HF)[SbF_6^-]$ in the crystal of $[SF_3^+](HF)[SbF_6^-]$ from X-ray crystallography. Thermal ellipsoids are drawn at the 50% probability level.

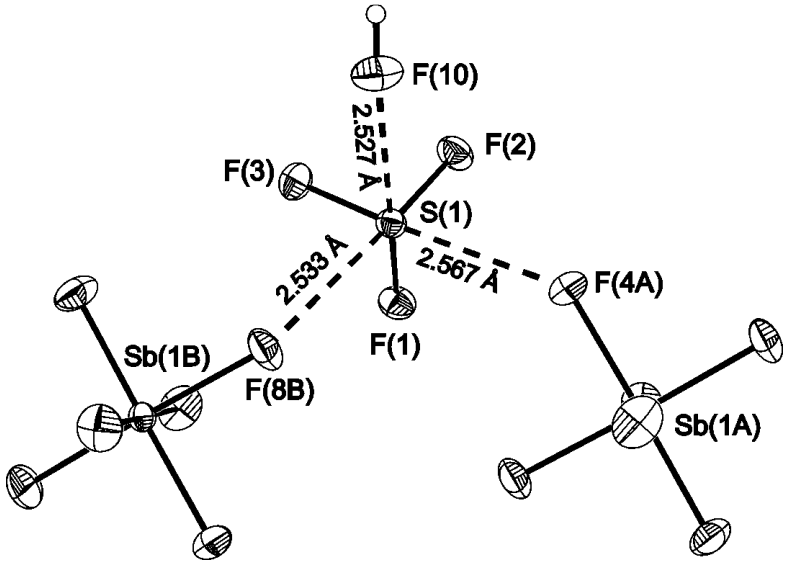

Figure: 5.9 Structure of $[SF_3^+](HF)[SbF_6^-]$ showing contacts in the crystal of $[SF_3^+](HF)[SbF_6^-]$ from X-ray crystallography. Thermal ellipsoids are drawn at the 50% probability level.

Table 5.4: Bond lengths and bond angles in the X-ray structure of $[SF_3^+](HF)[SbF_6^-]$

Bond Lengths and Contacts, Å		Bond angle,°	
S1—F2	1.5066(1)	F2—S1—F1	97.69(7)
S1—F1	1.5082(1)	F2—S1—F3	97.45(6)
S1—F3	1.5099(1)	F1—S1—F3	97.89(6)
S1···F(8B)	2.5330(1)	F7—Sb1—F9	90.69(5)
S1···F(4A)	2.5670(1)	F7—Sb1—F5	179.16(5)
S1···F(10)	2.5280(1)	F9—Sb1—F5	89.83(5)
Sb1—F7	1.8574(1)	F7—Sb1—F6	90.26(5)
Sb1—F9	1.8630(1)	F9—Sb1—F6	91.32(5)
Sb1—F5	1.8631(1)	F5—Sb1—F6	90.38(5)
Sb1—F6	1.8748(1)	F7—Sb1—F4	90.60(5)
Sb1—F4	1.8883(1)	F9—Sb1—F4	178.11(4)
Sb1—F8	1.8905(1)	F5—Sb1—F4	88.86(5)
		F6—Sb1—F4	90.05(5)
		F7—Sb1—F8	89.90(5)
		F9—Sb1—F8	90.50(5)
		F5—Sb1—F8	89.44(5)
		F6—Sb1—F8	178.18(5)
		F4—Sb1—F8	88.13(5)

Table 5.5 Crystal Data and structure Refinement for $[SF_3](HF)[SbF_6]$

Empirical formula	$HF_{10}SSb$
Formula weight, g mol^{-1}	344.82
Temperature, K	153
Wavelength, pm	71.073
Crystal System	Monoclinic
Space group	$P2_1/c$
Unit cell dimensions,	a = 5.60 (1) Å
	b = 10.27(1) Å
	c = 12.80(1) Å
	β = 100.30(10) º
Volume, 10^2 $Å^3$	7.36(1)
Z	4
Density(calculated), mg mm^{-3}	3.158
Absorption coefficient, mm^{-1}	4.23
F(000)	632
Crystal size, mm^3	0.43 × 0.28 × 0.19
Theta range for data collection	2.56° - 27.55°
Index ranges	$-7 \leq h \leq 7$,
	$-13 \leq k \leq 13$,
	$-16 \leq l \leq 16$
Reflections collected	8134
Independent reflections	1664 [R_{int} = 0.017]
Completeness to theta[27.55°]	99.2%
Refinement method	Full matrix Least-squares on F^2
Data/restraints/parameters	1664/1/114
Goodness-of-fit on F^2	1.092
Refine diff density_max	0.515
Refine diff density_ min	–0.400

5.3 Conclusion

With the help of variable-temperature solid-state ^{19}F MAS NMR spectra of $[SF_3][SbF_6]$, it was shown that three different phases of SF_3SbF_6 exist between –25 and –145°C. These phases were further confirmed with variable-temperature Raman spectroscopy. On the other hand, $[SF_3][AsF_6]$ showed no phase change in the same temperature range. The interpretation of the phases of $[SF_3][SbF_6]$ is tentative. Unambiguous correlation of the Raman and NMR spectra with structural features of the three modifications awaits crystallographic characterization. Crystal growth of $[SF_3][SbF_6]$ was attempted at –70°C using anhydrous HF as solvent. The SbF_6^- anion acts as a weakly coordinating anion leaving the SF_3^+ highly electrophilic, so that an HF molecule is entrapped in the coordination sphere of the SF_3^+ cation. The crystal structure of $[SF_3^+](HF)[SbF_6^-]$ represents one of the few HF solvate structures.

References

1. Azeem, M.; Brownstein, M.; Gillespie, R. J. *Can. J. Chem.* **1969**, *47*, 4159.
2. Oppegard, A. L.; Smith, W. C.; Muetterties, E. L.; Engelhardt, V. A. *J. Am. Chem. Soc.* **1960,** *82*, 3835.
3. Gillespie, R. J.; Moss, K. C. *J. Chem. Soc.* **1966**, 1170.
4. Gibler, D. D.; Adams, C. J.; Fischer, M.; Zalkin, A.; Bartlett, N. *Inorg. Chem.* **1972**, *11*, 2325.
5. (i) Mallouk, T. E.; Rosenthal, G. L.; Müller, G.; Brusasco, R.; Bartlett, N. *Inorg. .Chem.* **1984**, *23*, 3167 (ii) O'Brien, B. A.; DesMarteau, D. D. *Inorg. Chem.* **1984**, *23*, 644.

6. Smith, W. C. *Angew. Chem., Int. Ed.* **1962**, *1*, 467.

7. Kidd, R. G; Matthews, R. W. *Inorg. Chem*. **1972**, *11*, 1156.

8. Datars, W. R.; Ummat, P. K. *Solid State Commun.* **1995**, *94*, 649.

9. Muetterties, E. L.; Phillips, W. D. *J. Am. Chem. Soc.* **1959**, *81*, 1084.

10. Bondi, A. *J. Phys. Chem.*, **1964**, *68*, 441.

11. Gerken, M.; Dixon, D. A.; Schrobilgen, G. J. *Inorg. Chem.* **2002**, *41*, 259.

12. Mazej, Z.; Borrmann, H.; Lutar, K.; Zemva, B. *Inorg. Chem.* **1998**, *37*, 5912.

13. Roesky, H. W.; Sotoodeh, M.; Xu, Y. M.; Schrumpf, F.; Noltemeyer, M. Z., *Z. Anorg. Allg. Chem.* **1990**, *580*, 131.

14. Bacon, J.; Dean, P. A. W.; Gillespie, R. J. *Can. J. Chem.* **1969**, *47*, 1655.

15. Bartlett, N.; Robinson, P. L. *Chem. Ind. (London)* **1956**, 1351.

16. Bartlett, N.; Robinson, P. L. *J. Chem. Soc.* **1961**, 3417.

Chapter-6

Future Work

No two-dimensional NMR spectroscopic studies have been reported for trimethyltin fluoride. Several 2D NMR experiments will be very helpful in completing its unambiguous NMR characterization. Two-dimensional heteronuclear spin-echo double-resonance (SEDOR) experiments should be carried out in order to obtain exact relative tensor orientations for the two fluorine environments about tin. In addition, a series of variable slow-spinning $^{119}Sn\{^{1}H\}$ NMR spectra is necessary to determine more precisely the *J*–anisotropies of the coupling between ^{119}Sn and its adjacent two fluorine environments. A series of $^{117}Sn\{^{1}H,^{19}F\}$ NMR spectra should be recorded allowing to verify the $^{2}J(^{119}Sn\text{-}^{117}Sn)$ coupling constant observed in the present study.

The present Raman spectroscopic characterization of the reaction between SF_4 and nitrogen bases provided the first spectroscopic proof for adduction formation. A complete computational study of all prepared adducts will aid the complete assignment of the Raman spectra. Crystal growth of SF_4 adducts has to be attempted from excess SF_4 or solvents such as $CFCl_3$. A crystal structure of these Lewis acid base adducts would provide unambiguous proof of the predicted structures.

In the present work, three modifications were identified for $[SF_3][SbF_6]$. Conclusive interpretation of the spectroscopic results awaits X-ray crystallographic characterization of these phases. In the future, crystal growth of $[SF_3][SbF_6]$ can be attempted by crystallization from (a) molten $[SF_3][SbF_6]$, (b) anhydrous HF with large excess SbF_5 at low temperature, (c) SbF_5 solvent, and (d) by a solvothermal process of $[SF_3][SbF_6]$ with small amounts of anhydrous HF at elevated temperatures.

Appendix-1

SIMPSON simulation input file for solid-state ^{19}F MAS NMR spectrum at MAS 24 kHz

```
spinsys {
channels 19F 119Sn
nuclei 19F 19F 119Sn
shift 1 -134 -26000 0.6 0 0 0
shift 2 -134 -26000 0.6 0 141 0
shift 3 -1604 0 0 0 0 0
jcoupling 1 2 0 0 0 0 0 0
jcoupling 1 3 1320 -800 0 0 0 0
jcoupling 2 3 1320 3200 0 0 0 0
dipole 1 2 -1152 0 0 0
dipole 1 3 4266 0 0 0
dipole 2 3 3150 0 0 0}
par {
    start_operator          I1z
    detect_operator         I1p
    sw                      500000
    spin_rate               24000
    gamma_angles            20
    variable dwell          1e6/sw
    crystal_file            rep30
    np                      4096
    verbose                 1101
    variable rf1            138888.8
    variable t90            0.25e6/rf1
    proton_frequency        500.13e6}
proc pulseq {} {
  global par
  maxdt 1.0
  reset
  pulse $par(t90) $par(rf1) x 0 0
  acq
  for {set i 1} {$i < $par(np)} {incr i} {
  delay $par(dwell)
  acq}   }
proc main {} {
global par
set f [fsimpson]
fzerofill $f  65536
faddlb $f 250 0.5
fft $f
fphase $f -rp -13 -lp -130 -scale 200.06
fsave $f $par(name).spe}
```

Appendix-2

SIMPSON simulation input file for solid-state ^{19}F MAS NMR spectrum NMR spectrum at MAS 24 kHz

```
spinsys {
channels 19F 119Sn
nuclei 19F 19F 119Sn
shift 1 -134 -26000 0.6 0 0 0
shift 2 -134 -26000 0.6 0 141 0
shift 3 -1604 0 0 0 0 0
jcoupling 1 2 0 0 0 0 0 0
jcoupling 1 3 0 0 0 0 0 0
jcoupling 2 3 0 0 0 0 0 0
dipole 1 2 0 0 0 0
dipole 1 3 0 0 0 0
dipole 2 3 0 0 0 0 }
par {
   start_operator          I1z
   detect_operator         I1p
   sw                      500000
   spin_rate               24000
   gamma_angles            20
   variable dwell          1e6/sw
   crystal_file            rep30
   np                      4096
   verbose                 1101
   variable rf1            138888.8
   variable t90            0.25e6/rf1
   proton_frequency        500.13e6}
proc pulseq {} {
  global par
  maxdt 1.0
  reset
  pulse $par(t90) $par(rf1) x 0 0
  acq
  for {set i 1} {$i < $par(np)} {incr i} {
  delay $par(dwell)
  acq} }
proc main {} {
global par
set f [fsimpson]
fzerofill $f 65536
faddlb $f 250 0.5
fft $f
fphase $f -rp -13 -lp -130 -scale 200.06
fsave $f $par(name).spe}
```

Appendix-3

SIMPSON simulation input file for solid-state ^{119}Sn{^{1}H,^{19}F}MAS NMR spectrum at MAS 18 kHz

```
spinsys {
channels 119Sn 117Sn
nuclei 119Sn  117Sn 117Sn
shift 1 109 -39500 0.6 0 0 0
shift 2 -1604 4260 0 0 0 0
shift 3 -1604 4260 0 0 141 0
jcoupling 1 2 3539 0 0 0 0 0
jcoupling 1 3 3539 0 0 0 0 0
jcoupling 2 3 0 0 0 0 0 0
dipole 1 2 -166 0 0 0
dipole 1 2 -166 0 0 0
dipole 2 3 0 0 0 0}
par {
   start_operator          I1z
   detect_operator         I1m
   sw                      500000
   spin_rate               18000
   gamma_angles            20
   variable dwell          1e6/sw
   crystal_file            rep30
   np                      1024
   verbose                 1101
   variable rf1            138888.8
   variable t90            0.25e6/rf1
   proton_frequency        500.13e6}
proc pulseq {} {
  global par
  maxdt 1.0
  reset
  pulse $par(t90) $par(rf1) x 0 0
  acq
  for {set i 1} {$i < $par(np)} {incr i} {
  delay $par(dwell)
  acq}   }
proc main {} {
global par
set f [fsimpson]
fzerofill $f 32768
faddlb $f 300 0.5
fft $f
fphase $f -rp -13 -lp -130 -scale 200.06
fsave $f $par(name).spe}
```

Appendix-4

SIMPSON simulation input file for solid-state ^{119}Sn{^{1}H,^{19}F}MAS NMR spectrum at MAS 24 kHz

```
spinsys {
channels 119Sn 19F
nuclei 119Sn 19F  19F
shift 1 424 -39500 0.60 0 165 0
shift 2 -293 -26000 0 0 0 0
shift 3 -293 -26000 0 0 15 0
jcoupling 1 2 1320 -800 0 0 0 0
jcoupling 1 3 1320 3200 0 0 0 0
jcoupling 2 3 0 0 0 0 0 0
dipole 1 2 4266 0 0 0
dipole 1 3 3200 0 0 0
dipole 2 3 -1152 0 0 0 }
par {
   start_operator          I1z
   detect_operator         I1m
   sw                      500000
   spin_rate               24000
   gamma_angles            20
   variable dwell          1e6/sw
   crystal_file            rep30
   np                      1024
   verbose                 1101
   variable rf1            138888.8
   variable t90            0.25e6/rf1
   proton_frequency        500.13e6}
proc pulseq {} {
  global par
  maxdt 1.0
  reset
  pulse $par(t90) $par(rf1) x 0 0
  acq
  for {set i 1} {$i < $par(np)} {incr i} {
  delay $par(dwell)
  acq }  }
proc main {} {
global par
set f [fsimpson]
fzerofill $f 32768
faddlb $f 300 0.5
fft $f
fphase $f -rp -13 -lp -130 -scale 200.06
fsave $f $par(name).spe}
```

Appendix-5

Atomic coordinates and isotropic or equivalent isotropic displacement parameters ($Å^2$) for $[SF_3](HF)[SbF_6]$

	x	y	z	U_{iso}*/U_{eq}
Sb1	0.378435 (17)	0.253048 (8)	0.034554 (8)	0.01483 (6)
S1	0.95062 (7)	0.46906 (3)	0.79248 (3)	0.01747 (9)
F1	0.61421 (18)	0.15188 (10)	−0.01446 (9)	0.0338 (2)
F2	0.60122 (18)	0.38723 (9)	0.06788 (9)	0.0326 (2)
F3	0.46551 (17)	0.18477 (10)	0.17072 (7)	0.0300 (2)
F4	0.15166 (17)	0.12028 (9)	0.00043 (8)	0.0285 (2)
F5	0.13740 (16)	0.35693 (9)	0.07955 (8)	0.0278 (2)
F6	0.27931 (17)	0.32162 (9)	−0.10315 (7)	0.0268 (2)
F7	0.97720 (17)	0.36485 (9)	0.71268 (7)	0.0254 (2)
F8	0.79335 (17)	0.39374 (9)	0.85518 (8)	0.0249 (2)
F9	0.75191 (17)	0.54580 (9)	0.72409 (7)	0.0270 (2)
F10	0.7921 (2)	0.09734 (11)	0.81412 (9)	0.0344 (3)
H1	0.762 (5)	0.108 (3)	0.869 (2)	0.080 (10)*

Appendix-6

Anisotropic displacement parameters for $[SF_3](HF)[SbF_6]$. The anisotropic displacement factor exponent takes the form: $-2\pi^2[h^2a^{*2}U^{11}+\ldots\ldots+ 2\ h\ k\ a^*\ b^*\ U^{12}]$

	U^{11}	U^{22}	U^{33}	U^{12}	U^{13}	U^{23}
Sb1	0.01288 (8)	0.01607 (8)	0.01552 (8)	0.00179 (3)	0.00249 (5)	0.00031 (3)
S1	0.01682(17)	0.01953 (18)	0.01600 (18)	0.00094 (13)	0.00280 (12)	−0.00084 (13)
F1	0.0288 (5)	0.0374 (6)	0.0388 (6)	0.0142 (4)	0.0160 (5)	0.0006 (5)
F2	0.0270 (5)	0.0301 (5)	0.0377 (6)	−0.0112 (4)	−0.0025 (4)	0.0020 (4)
F3	0.0272 (5)	0.0399 (6)	0.0215 (5)	0.0028 (4)	0.0005 (4)	0.0112 (4)
F4	0.0273 (5)	0.0240 (5)	0.0335 (6)	−0.0083 (4)	0.0031 (4)	−0.0039 (4)
F5	0.0225 (5)	0.0312 (5)	0.0304 (5)	0.0081 (4)	0.0064 (4)	−0.0086 (4)
F6	0.0297 (5)	0.0305 (5)	0.0190 (5)	0.0037 (4)	0.0012 (4)	0.0057 (4)
F7	0.0260 (5)	0.0288 (5)	0.0215 (5)	0.0024 (4)	0.0042 (4)	−0.0078 (4)
F8	0.0244 (5)	0.0267 (5)	0.0257 (5)	−0.0034 (4)	0.0098 (4)	0.0001 (4)
F9	0.0237 (5)	0.0312 (5)	0.0241 (5)	0.0069 (4)	−0.0009 (4)	0.0037 (4)
F10	0.0384 (6)	0.0423 (6)	0.0239 (6)	0.0045 (5)	0.0096 (5)	−0.0054 (5)

Appendix-7

Bond Lengths (Å) and Angles (°) for $[SF_3](HF)[SbF_6]$

Sb1—F1	1.8743(9)
Sb1—F2	1.8566(9)
Sb1—F3	1.8617(9)
Sb1—F4	1.8613(9)
Sb1—F5	1.8895(9)
Sb1—F6	1.8878(9)
S1—F7	1.5055(9)
S1—F8	1.5072(10)
S1—F9	1.5091(9)
F2—Sb1—F4	179.18(4)
F2—Sb1—F3	90.68(5)
F4—Sb1—F3	89.84(4)
F2—Sb1—F1	90.24(5)
F4—Sb1—F1	90.39(5)
F3—Sb1—F1	91.30(5)
F2—Sb1—F6	90.62(4)
F4—Sb1—F6	88.85(4)
F3—Sb1—F6	178.12(4)
F1—Sb1—F6	90.06(4)
F2—Sb1—F5	89.87(4)
F4—Sb1—F5	89.48(4)
F3—Sb1—F5	90.50(4)
F1—Sb1—F5	178.19(4)
F6—Sb1—F5	88.13(4)
F7—S1—F8	97.74(6)
F7—S1—F9	97.45(6)
F8—S1—F9	97.87(6)